THE UNIVERSITY *of* EDINBURGH

THE UNIVERSITY *of* EDINBURGH

Curvature Statistics of Turbulence

by

Yasmin Hengster

Doctor of Philosophy
University of Edinburgh
October 2025

Declaration

I declare that this thesis was composed by myself, that the work contained therein is my own, except where explicitly stated otherwise in the text, and that it has not been submitted, in whole or in part, for any other degree or professional qualification.

Parts of this work have been published in Hengster et al. (2024).

Yasmin Hengster, October 2024

Abstract

Turbulence is present in many different flow types across natural phenomena and industrial applications but still raises open questions due to its complexity and multi-scale nature which defers most direct analytical approaches. However, a statistical approach has proven itself as a powerful tool to help with the understanding and modelling of turbulence, overcoming some limitations of analytical approaches.

Within this thesis, I analyse datasets of four different flow types, three of experimental nature and one of numerical nature to study the statistics of geometric quantities such as curvature and torsion, in particular concerning the effect of anisotropy. For the experimental datasets, the focus is on Lagrangian trajectories and for the numerical datasets on stream lines and, in case of a conducting fluid, magnetic field lines. These curves can be described as three-dimensional space curves and therefore curvature and torsion can give a full description of these. Curvature and torsion are particularly interesting measures of turbulence as a salient feature of turbulence is the presence of different spatial and temporal scales, which is captured by the different derivatives involved. The curvature vector is introduced as a new measure of the effect of anisotropies, originating from different mechanisms like a temperature gradient, mean flow or magnetic background field, on the geometry of Lagrangian trajectories and either stream lines or, in case of a conducting fluid, magnetic field lines.

The first study includes Lagrangian experimental datasets of a turbulent von Kármán flow, Rayleigh-Bénard convection at two different Rayleigh numbers and the logarithmic layer of a turbulent zero-pressure-gradient boundary layer over a flat plate. The curvature and torsion statistics of von Kármán flow and Rayleigh-Bénard convection agree well with previously reported experimental and numerical results for the curvature and with numerical simulations of homogeneous and isotropic turbulence for the torsion. For the logarithmic region of the boundary layer, the form of the torsion probability density function (PDF) also agrees with

these results. The curvature PDF retains the same heavy tail as curvature PDFs measured for the aforementioned flow types for small curvature events, however, high curvature events are suppressed by the mean flow. Studying the curvature vector and connecting it with velocity fluctuations shows the effect of anisotropy and allows a geometric interpretation of large-scale motion in terms of the structure of trajectories.

In the second study, another type of anisotropy is introduced by a magnetic background field for a flow with electrically conducting fluid in magnetohydrodynamic turbulence. Utilising high resolution data obtained by direct numerical simulation of magnetohydrodynamic turbulence across a range of Reynolds numbers, the curvature PDFs of stream lines and magnetic field lines compare well with the PDFs derived based on Gaussian statistics for the Lagrangian trajectories. For the PDFs of the curvature vector components, the magnetic field lines tend to be less curved in the direction of the magnetic background field, which can be connected to the suppression of magnetic field fluctuations parallel to the magnetic background field and the partial two-dimensionalisation of the flow. The curvature vector PDFs of stream lines show that the effect of a magnetic background field on the geometry of stream lines is less profound compared to the effect on the magnetic field lines.

The models mentioned above are based on Gaussian statistics. However, turbulence is more complex and intermittency plays a crucial role. As an improvement of these models, a model for the curvature PDF for von Kármán flow and Rayleigh-Bénard convection is derived, which takes spatio-temporal intermittency into account. Using a decomposition into Gaussian sub-ensembles, where within each the curvature PDF is known exactly, an exact model expression and a closed-form approximation for the curvature PDF can be derived. These PDFs agree qualitatively and quantitatively with the measured curvature PDFs of turbulent von Kármán flow and Rayleigh-Bénard convection.

Lay Summary

Turbulent flows occur throughout nature and industry, from the flow around an air plane to the convection in the sun. However, a complete understanding of turbulence remains one of the major challenges in modern physics. This is due to its complexity, as turbulence acts across multiple spatial and temporal scales, and depending on the flow type, may be highly

sensitive to both initial conditions and boundary conditions.

The focus of this thesis is on the effect of anisotropy on the geometry of particle trajectories, magnetic field lines and flow stream lines. For this, statistics of the curvature and torsion are calculated which are particularly useful as these mix information of different scales. To further quantify the effect of anisotropy the curvature vector is introduced, which allows us to connect large-scale motion with the geometric structure of the trajectories, magnetic field lines and stream lines.

We consider four types of turbulent flow, experimental studies of a von Kármán flow, Rayleigh-Bénard convection, and a turbulent zero-pressure-gradient boundary layer, as well as direct numerical simulations of flows of electrically conducting fluid. For von Kármán flow, Rayleigh-Bénard convection and the magnetohydrodynamic flow, the curvature and torsion statistics do not reveal any effects of anisotropy, while for the boundary layer the curvature tends to be smaller and particle trajectories are more stretched. Using the curvature vector, the effects of anisotropy become more apparent in all flow types, helping with the understanding on how temperature gradients, mean flows, or magnetic fields influence the geometry of particle trajectories, stream lines and magnetic field lines. Additionally, a model for the curvature PDF in von Kármán flow and Rayleigh-Bénard convection using Gaussian statistics is derived and compared to data.

Acknowledgments

I thank my supervisor Dr. Moritz Linkmann for his scientific guidance, support and endless patience. I am especially grateful for his mentorship and the way he shared his knowledge, helping shape this work in ways that would not have been possible without him.

I would also like to thank Prof. Michael Wilczek for his scientific guidance during my research visit and beyond. I also thank the group in Bayreuth for making me feel welcome during my time in Bayreuth. Many thanks also to various collaborators for providing data and fruitful discussions.

I would like to thank my family for their constant support throughout my PhD journey. Their encouragement to pursue opportunities abroad, their understanding of my absences, and their endless support have made this work possible.

I am grateful to my friends who made these years of research an enjoyable experience.

I am thankful for the funding that I received from Priority Programme SPP 1881 "Turbulent Superstructures" of the Deutsche Forschungsgemeinschaft (DFG, grant number LI3694/1).

Contents

List of Figures

List of Tables

Chapter 1

Introduction

Flows occur in many natural phenomena and industrial applications and are described by the equations of fluid dynamics. Flows can be separated into two main categories, firstly, in laminar flows where movements are smooth and regular and it is possible to describe the flow analytically and secondly, in turbulent flows where the motions are more chaotic and irregular. It is hard to almost impossible to describe turbulence analytically, such that turbulence still raises a lot of open questions. However, turbulence is omnipresent, thus there is a need to understand it. Examples of the occurrence of turbulence are a flow over an air plane wings, where drag caused by turbulence reduces the efficiency of air planes, in the atmosphere, where turbulences influences the weather through convection, or magnetic convection in the sun.To help with the understanding of the different occurrences of turbulence in more detail, different simplified experimental and numerical setups can be investigated. Within this thesis, the focus shall be on the geometric description of turbulence. This can be done through either particles in the flow that represent the overall movement of the flow or through lines frozen into the flow, representing the direction of the velocity field. Mathematically, these lines can be interpreted as space curves and as such can be fully described by its *curvature* and *torsion* (Bär, 2010), making these two properties useful observables to describe the geometric features of turbulence. For most cases, initial conditions cannot be prescribed with sufficient precision, thus a statistical description of turbulence can be useful. Multiple studies have discussed curvature and torsion statistics of turbulent flows. While most works focus on curvature statistics (Schekochihin et al., 2001, 2002, 2004; Braun et al., 2006; Xu et al., 2007; Alards et al., 2017; Yang et al., 2019; Yuen and Lazarian, 2020; Ji et al., 2022; Bandy-

opadhyay et al., 2020; Lemoine, 2023; Scagliarini, 2011; Bentkamp et al., 2022; Hengster et al., 2024), some also investigate torsion statistics (Alards et al., 2017; Scagliarini, 2011). It appears that the probability density functions (PDFs) exhibit a universal power law for most flow types. Closed-form models have been derived for these PDF (Schekochihin et al., 2001; Xu et al., 2007; Bentkamp et al., 2022), based on Gaussian statistics for the velocity and acceleration. These assumptions are generally not true, specifically for the acceleration (Mordant, Crawford and Bodenschatz, 2004; Bentkamp et al., 2019; Biferale, Boffetta, Celani, Devenish, Lanotte and Toschi, 2004; Lawson et al., 2018). By taking deviations from Gaussian statistics into account, we derived an improved model for the curvature PDF. Additionally, the different flow types mentioned above are all of different nature and have different boundary conditions, resulting in anisotropies in the flow. To capture these, a new measure, the *curvature vector*, will be introduced, highlighting differences for different flow types.

This chapter will give an overview about important physical and mathematical concepts in the field of fluid dynamics, and more specifically turbulence. After introducing the governing equations, I will explain commonly used concepts in fluid dynamics and outline the specifics of the different flow types considered within this thesis. Some of the material presented in the following sections is based on the books of Pope (2000), Frisch (1995) and Batchelor (1953).

1.1 Navier-Stokes Equations

The motion of fluids is governed by the Navier-Stokes equations, which can be derived from the conservation of mass and the conservation of momentum. A common assumption in the field of fluid dynamics, also used in this work, is that the flow is incompressible and the density is constant in space and time. The conservation of mass for an incompressible flow leads to:

$$\nabla \cdot \boldsymbol{u} = 0\,, \tag{1.1}$$

where $\boldsymbol{u}$ is the velocity. From the conversation of momentum and the conversation of mass, the Navier-Stokes equations for incompressible flows can be derived:

$$\partial_t \boldsymbol{u} + \boldsymbol{u} \cdot \nabla \boldsymbol{u} = -\nabla p + \nu \Delta \boldsymbol{u} + \boldsymbol{f} \tag{1.2}$$

where p is the pressure divided by density ρ, also called kinematic pressure, and $-\nabla p$ the pressure gradient, describing changes of pressure in the fluid, ν is the kinematic viscosity and $\boldsymbol{f}$ is an optional external force, examples include gravity or an external pressure gradient. The non-linear term $\boldsymbol{u} \cdot \nabla \boldsymbol{u}$ is the advection or inertial term, causing energy transfer across scales, and $\nu \Delta \boldsymbol{u}$ is the viscous term, responsible for momentum diffusion and energy dissipation. Using a characteristic velocity U_0 and length scale L determined by the flow type, a characteristic time L/U_0 and pressure ρU_0^2 can be defined and equation (1.2) can be non-dimensionalised:

$$\partial_{t^*} \boldsymbol{u}^* + \boldsymbol{u}^* \cdot \nabla^* \boldsymbol{u}^* = -\nabla^* p^* + \frac{1}{Re} \Delta^* \boldsymbol{u}^* + \boldsymbol{f}^* \tag{1.3}$$

where ()* indicate non-dimensionalised variables and

$$Re = \frac{U_0 L}{\nu} \tag{1.4}$$

is the Reynolds number. The Reynolds number describes the ratio of inertial to viscous forces, allowing an alternative derivation of the Reynolds number. In the Navier-Stokes equations, the inertial forces are $\partial_t \boldsymbol{u} + \boldsymbol{u} \cdot \nabla \boldsymbol{u} \sim \frac{U_0^2}{L}$ and the viscous forces are $\nu \Delta \boldsymbol{u} \sim \frac{\nu U_0}{L^2}$, and therefore $Re = \frac{U_0^2}{L} / \frac{\nu U_0}{L^2} = \frac{U_0 L}{\nu}$. Examples for U_0 can be the free stream velocity in a boundary layer or the free-fall velocity in convection and for L pipe diameter or the box height for convection are commonly used variables. A higher Reynolds number often indicates a more turbulent flow. It allows us to compare similar flow conditions even if the physical scales (velocity and length scale) differ. Flows can be categorised into two main states where laminar flows are smooth and regular flows while turbulent flows are more chaotic and feature motion at different scales. The Reynolds number can be used as an indicator to determine which state a flow falls into. In the following, the ()* is dropped for convenience and discussed variables are non-dimensional unless states otherwise.

In turbulent flows, the kinetic energy is distributed across a wide range of spatial scales, this is described by the energy spectrum $E(k)$, where k is the wavenumber. The energy spectrum is the Fourier transform of the velocity autocorrelation function which will be defined in a later section. The total kinetic energy is given by the energy across all scales (Batchelor, 1953):

$$E_u = \frac{1}{2}\langle u_i u_i \rangle = \int_0^\infty E(k)dk \tag{1.5}$$

where the sum over repeated indices is implied. Energy dissipates into heat at the smallest scales with the energy dissipation rate ε. To describe how the energy gets transferred to the scales of dissipation, the energy flux can be calculated. The scale filtered energy flux Π^ℓ, where ℓ is the filter scale, quantifies the amount of energy that gets transferred from scales larger than ℓ to scales smaller than ℓ (positive flux), or from scales smaller than ℓ to scales larger than ℓ (negative flux), and can be defined as (Buzzicotti et al., 2018):

$$\Pi^\ell = -\frac{\partial \bar{u}_i^\ell}{\partial x_j}\tau^\ell(u_i, u_j) \tag{1.6}$$

where $\bar{u}_i^\ell = \int d^3r G^\ell(\boldsymbol{r}) u_i(\boldsymbol{x}+\boldsymbol{r})$ represents the filtered velocity field using a low pass filter $G^\ell(\boldsymbol{r})$, and

$$\tau^\ell(u_i, u_j) = \overline{u_i u_j}^\ell - \overline{u_i}^\ell \overline{u_j}^\ell \tag{1.7}$$

is the sub-grid scale stress tensor and $\overline{u_i u_j}^\ell = \int d^3r G^\ell(\boldsymbol{r}) u_i(\boldsymbol{x}+\boldsymbol{r}) u_j(\boldsymbol{x}+\boldsymbol{r})$. If a Galerkin projector with cutoff wavenumber $k = \pi/\ell$ is used, the flux can also be calculated in Fourier space.

Solving the Navier-Stokes equations requires a set of initial and boundary conditions. The experimental datasets provided are using Dirichlet boundary conditions and for the numerical datasets periodic boundary conditions are used. For some simple cases of laminar flows, it is possible to solve the Navier-Stokes equations analytically. Generally, solving the Navier-Stokes equations is seen to be one of the biggest challenges in modern physics as they may be extremely sensitive to initial and boundary conditions for some flow types and parameter regimes. For more complex systems like temperature-driven convection or magnetohydrodynamic turbulence, the Navier-Stokes equations are coupled with additional equations dependent on these processes. While these equations are deterministic, it can be

indefinitely difficult to solve the Navier-Stokes equations and it is helpful to look at turbulence from a statistical point of view. For this, data needs to recorded which can be done in either the Lagrangian frame of reference or the Eulerian frame of reference.

1.1.1 Eulerian and Lagrangian Frame of Reference

Fluid dynamics can be studied in two different frames of reference: the Eulerian frame of reference and the Lagrangian frame of reference.

The Eulerian frame of reference describes the flow in the laboratory frame at a set of fixed points. It is commonly used for numerical simulations. A field, for example the velocity field $\boldsymbol{u}(\boldsymbol{x}, t)$ is described as a function of the position $\boldsymbol{x}$ and time t. In numerical simulations these points would be fixed grid points, in experiments fixed measure points can be used to describe a flow in the Eulerian frame of reference.

In the Lagrangian frame of reference trajectories of fluid parcels in the flow are followed, where the position $\boldsymbol{X}(\boldsymbol{X_0}, t)$ is recorded as a function of time t and the initial position $\boldsymbol{X_0}$ at an initial time t_0. In numerical simulations, initial conditions can be set by the user by seeding particles across the measurement volume at a selected time t_0. In experiments, the initial condition of a particle is determined by the time and position at which a particle enters the measurement volume and is captured by the tracking system. Generally, initial time and position vary for all trajectories. The velocity of a fluid parcel is given by:

$$\partial_t \boldsymbol{X}(\boldsymbol{X_0}, t) = \boldsymbol{u}(\boldsymbol{X}(\boldsymbol{X_0}, t), t) \ . \tag{1.8}$$

As a result we get the time series of the velocity along the trajectory of a fluid parcel. In a numerical setting, a flow map is used to generate Lagrangian trajectories through interpolation. A flow map can, for example, be provided through an analytic function or numerical simulations of Eulerian nature. Generating the trajectories from a given velocity field ensures that the particles do not impact the flow but requires an additional step which can be expensive.

In experiments, passive tracer particles are used as fluid parcels to visualise the movement of the flow. These tracer particles are small particles with properties that are similar to the fluid, allowing them to closely follow the flow. Their diameter should smaller than the

smallest length to ensure that the smallest flow structures are captured. Passive tracer particles should also have no or small inertia to avoid impacting and changing the flow. This effect is measured by the Stokes number St:

$$St = \frac{\tau_p}{\tau_\eta} \tag{1.9}$$

where τ_p is the particles response time and τ_η is the Kolmogorov time scale, which is the smallest time scale of the flow and will be further described in section 1.4. The particle response time is the time it takes for a particle to adjust its velocity to changes in the surrounding fluid flow due to drag forces. If the Stokes number is smaller than one, the particles have a negligible effect on the flow and can be treated as passive tracer particles, otherwise effects of the particles on the flow need to be taken into account which are described by the Maxey-Riley equation (Maxey and Riley, 1983). Tracking tracer particles in experiments brings its own challenges which will be discussed in section 2.1.

1.2 Statistical Approach to Turbulence

While the Navier-Stokes equations are deterministic equations, they are extremely sensitive to any perturbations in the initial conditions. A small perturbation in the initial conditions can result in a completely different flow evolution. This becomes more apparent with increasing Reynolds number in the turbulence regime when the system is chaotic. As it is almost impossible to avoid uncertainty in the initial conditions, it is helpful to look at turbulence from a statistical point of view.

The velocity field can be treated as a random process in space and time where the next time step cannot be predicted. That allows to calculate statistical properties like probability density functions, joint PDFs, statistical moments or correlation functions. The first four

standardised moments are the mean μ, variance σ^2, skewness S and kurtosis or flatness K:

$$\mu = \langle X \rangle = \int dX P(X) X \tag{1.10}$$

$$\sigma^2 = \langle (X-\mu)^2 \rangle = \int dX P(X)(X-\mu)^2 \tag{1.11}$$

$$S = \langle (X-\mu)^3 \rangle / \sigma^3 = \frac{1}{\sigma^3} \int dX P(X)(X-\mu)^3 \tag{1.12}$$

$$K = \langle (X-\mu)^4 \rangle / \sigma^4 = \frac{1}{\sigma^4} \int dX P(X)(X-\mu)^4 \tag{1.13}$$

where $P(X)$ is the PDF of the random variable X and σ is the standard deviation. The mean represents the average value of the data, variance measures how much the data deviates from the mean, skewness quantifies the asymmetry of a distribution, and the kurtosis or flatness describes the heaviness of the tails of a distribution.

Since Gaussian distributions are widely used in statistics, statistical moments of a random variable are often compared to those of a standardised Gaussian distribution. The PDF of a Gaussian distribution is

$$P(X) = \frac{1}{\sqrt{2\pi\sigma^2}} e^{-\frac{(X-\mu)^2}{2\sigma^2}} . \tag{1.14}$$

which can be used to calculate the first four statistical moments of a standardised Gaussian distribution:

$$\mu = 0$$

$$\sigma = 1$$

$$S = 0$$

$$K = 3 .$$

Another commonly measure is the excess kurtosis, defined as $K-3$, as this directly measures deviations from the Gaussian value of 3. More generally, statistical moments of a standard Gaussian process are given by:

$$\langle X^p \rangle = \begin{cases} 0 & \text{if } p \text{ odd} \\ \frac{(2n)!}{n!2^n} & \text{if } p \text{ even} \end{cases}$$

for any positive integer $p > 0$.

For discrete data, the integrals in equations (1.10) - (1.13) are replaced by summations:

$$\langle X \rangle = \frac{1}{N} \sum_{i=1}^{N} X_i \tag{1.15}$$

for the mean where N is the number of data points and X_i the value of a data point i. For the other moments, the equations are analogous. To ensure statistical convergence, a combination of an ensemble (space) average and time average is used. For Lagrangian trajectories, that is:

$$\langle X \rangle = \frac{1}{Q} \sum_{i=1}^{M} \sum_{j=1}^{N_i} X^{(i)}(t_j) \tag{1.16}$$

where M is the number of trajectories, N_i the number of time steps of the i-th trajectory, t_j the j-th time step of the i-th trajectory, Q the total number of data points considered and $X^{(i)}(t_j)$ the value of the random variable at time t_j of the i-th trajectory. For an Eulerian field, the total average is:

$$\langle X \rangle = \frac{1}{T \cdot N} \sum_{i=1}^{T} \sum_{j=1}^{N} X^{(i)}(x_j) \tag{1.17}$$

where T is the number of time steps (fields) considered with a grid containing a total of N points distributed at fixed locations within the measurement volume. The value of the random variable at time step i at grid point x_j is $X^{(i)}(x_j)$. The equations for moments of order two and above are analogous.

An additional set of important statistical measures are correlation tensors. We can define correlation functions either in the Eulerian frame of reference:

$$C_{ij}^{E}(\boldsymbol{x_1}, \boldsymbol{x_2}) = \langle u_i(\boldsymbol{x_1}, t) u_j(\boldsymbol{x_2}, t) \rangle \tag{1.18}$$

at a fixed t and the average indicates the average over different realisations. For statistical convergence, a time average may also be included. In the Lagrangian frame of reference, the correlation function is defined as:

$$C_{ij}^{L}(t_1, t_2) = \langle u_i(\boldsymbol{x}(t_1), t_1) u_j(\boldsymbol{x}(t_2), t_2) \rangle \tag{1.19}$$

of a specific trajectory $x(t)$. The average here would ideally indicate an average of different

realisations of the same particle. However, due to the nature of Lagrangian trajectories, this is not possible and the average is taken over different trajectories to achieve statistical convergence.

The time t_2 can also be written as $t_2 = t_1 + \tau$ where τ is a time lag, analogously $\boldsymbol{x_2} = \boldsymbol{x_1} + \boldsymbol{r}$ where $\boldsymbol{r}$ is a displacement vector. Therefore, the correlation functions become:

$$C_{ij}^{E}(\boldsymbol{x_1}, \boldsymbol{r}) = \langle u_i(\boldsymbol{x_1}, t) u_j(\boldsymbol{x_1} + \boldsymbol{r}, t) \rangle \,. \tag{1.20}$$

$$C_{ij}^{L}(t_1, \tau) = \langle u_i(\boldsymbol{x}(t_1), t_1) u_j(\boldsymbol{x}(t_1 + \tau), t_1 + \tau) \rangle \,. \tag{1.21}$$

For $i = j$ this is also known as the autocorrelation function of the velocity component u_i. The acceleration autocorrelation function can be defined in an analogous manner.

In the next section, the concept of statistically stationary homogeneous and isotropic turbulence is introduced. For these cases, the statistics do not depend on the t_1 or the location $\boldsymbol{x_1}$ and the correlation functions become independent of these:

$$C_{ij}^{E}(\boldsymbol{r}) = \langle u_i(\boldsymbol{x}, t) u_j(\boldsymbol{x} + \boldsymbol{r}, t) \rangle \tag{1.22}$$

$$C_{ij}^{L}(\tau) = \langle u_i(\boldsymbol{x}(t), t) u_j(\boldsymbol{x}(t + \tau), t + \tau) \rangle \tag{1.23}$$

and the averages become spatial, time and ensemble averages ensuring statistical convergence. Based on that, we can define velocity structure functions in the Eulerian ($G_p(r)$) and Lagrangian ($S_p(\tau)$) frame of reference which are the p-th moment of the velocity increments $\delta_r u_i$ and $\delta_\tau u_i$:

$$G_p(r) = \langle (u_i(\boldsymbol{x} + \boldsymbol{r}) - u_i(\boldsymbol{x}))^p \rangle =: \langle (\delta_r u_i)^p \rangle \tag{1.24}$$

where $r = |\boldsymbol{r}|$. The Lagrangian structure functions can be defined as:

$$S_p(\tau) = \langle (u_i(t + \tau) - u_i(t)^p \rangle = \langle (\delta_\tau u_i)^p \rangle \,. \tag{1.25}$$

From Kolmogorov's theory, scaling laws for the structure functions can be derived which will be explained in the section 1.4.

1.3 Homogeneous and Isotropic Turbulence

A specific type of turbulence, introduced for theoretical simplicity, is homogeneous and isotropic turbulence (Taylor, 1935). This concept is about statistical symmetries, where isotropy means that PDFs are invariant under all $SO(3)$ rotations, a specific case of $O(3)$, that does not include reflections:

$$P\left(\boldsymbol{u}(\boldsymbol{x})\right) = P\left(\boldsymbol{u}(R\boldsymbol{x})\right) . \tag{1.26}$$

where R is a rotation matrix which could, for example, be a rotation by angle θ around the z-axis:

$$R(\theta) = \begin{pmatrix} \cos\theta & -\sin\theta & 0 \\ \sin\theta & \cos\theta & 0 \\ 0 & 0 & 1 \end{pmatrix} . \tag{1.27}$$

Homogeneity refers to space translations, meaning that the PDF is invariant when shifted by $\Delta\boldsymbol{x}$ in space:

$$P(\boldsymbol{u}(\boldsymbol{x})) = P(\boldsymbol{u}(\boldsymbol{x} + \boldsymbol{\Delta x})) . \tag{1.28}$$

Additionally the concept of statistically stationary turbulence can be introduced, referring to the PDF being invariant under time translation Δt:

$$P(\boldsymbol{u}(\boldsymbol{x}(t)) = P(\boldsymbol{u}(\boldsymbol{x}(t + \Delta t))) . \tag{1.29}$$

While these concepts are useful for theoretical calculations and models, finding flow conditions that fully satisfy them in reality is generally challenging. This can occur, for example, due to the presence of boundaries, where boundary conditions influence the flow behaviour near the edges, which can differ from the flow dynamics within the domain. Another example is the presence of a mean velocity in one direction, which breaks isotropy or energy dissipation compromising statistical stationarity. However, if the Reynolds number is sufficiently high and we observe flows far away from boundaries for relatively short amount of times, we can speak of local isotropy and local homogeneity where the flow scales are much smaller than the scales of the system. As turbulence is dissipative, a statistically stationary state can only be achieved in presence of a kinetic energy supply.

Even with these limitations, the concept of stationary homogeneous and isotropic turbulence is a useful concept and due to the complexity of turbulence a good starting point for theoretical models.

1.3.1 Taylor Microscale

The concept of homogeneous isotropic turbulence does not allow us to define a flow typical length scale, for example the height of a box, and therefore defining the Reynolds number like in equation 1.4 is not possible. A commonly used length scale instead is the Taylor microscale λ, introduced by Taylor (1935):

$$\lambda = \sqrt{\frac{15\nu}{\varepsilon}} U_{rms} \tag{1.30}$$

where $U_{rms} = \sqrt{1/3\ (\langle u_x^2 \rangle + \langle u_y^2 \rangle + \langle u_z^2 \rangle)}$ is the averaged root-mean-square of the velocity components and ε the mean dissipation rate. The dissipation rate ε quantifies the rate at which turbulence kinetic energy is converted into thermal energy due to viscosity and given by:

$$\varepsilon = 2\nu \langle S_{ij} S_{ij} \rangle \tag{1.31}$$

where $S_{ij} = \frac{1}{2}\left(\frac{\partial u_i}{\partial x_j} + \frac{\partial u_j}{\partial x_i}\right)$ is the strain rate tensor. The factor 15 in the Taylor microscale can be derived from the energy dissipation in homogeneous and isotropic turbulence, a detailed derivation can be found in Taylor (1935).

This length scale is the largest scale from where energy starts to dissipate. Having a length scale, independent of the system size, leads to a definition of the Taylor-scale Reynolds number based on the Taylor microscale:

$$Re_\lambda = \frac{U_{rms}\lambda}{\nu} = \sqrt{\frac{15}{\varepsilon\nu}} U_{rms}^2 \,. \tag{1.32}$$

1.4 Kolmogorov Scales

Turbulence is a multi scale-phenomenon where energy gets transferred across scales. Richardson (2007) introduced in 1922 the concept of turbulence where the largest eddies, which are of size ℓ_0 and comparable to the characteristic scale of the flow, are unstable and break up

into smaller eddies where energy gets transferred from the larger scale to the smaller scale. This process repeats itself until the energy dissipates due to viscosity at small scales. The energy transfer across scales can be described by the energy cascade. Kolmogorov developed a theory to describe the energy cascade in a mathematical way.

1.4.1 Kolmogorov 1941 Theory

Kolmogorov's theory from 1941 (K41) describes the process of energy being transferred and results in the famous 5/3-law for the energy spectrum (Kolmogorov, 1941). His theory is based on 3 hypotheses, paraphrased from Pope (2000). The first two of such are:

- **Kolmogorov's hypothesis of local isotropy.** At sufficient high Reynolds number, the small-scale turbulent motions ($\ell \ll \ell_0$) are statistically isotropic.
- **Kolmogorov's first similarity hypothesis.** In every turbulent flow at sufficiently high Reynolds number, the statistics of small-scale motions ($\ell < \ell_0$) have a universal form that is uniquely determined by the viscosity ν and dissipation rate ε.

where ℓ_0 is a length scale that divides eddies into anisotropic large eddies and isotropic small eddies. The length scale of the smallest eddies before dissipating is the Kolmogorov length scale η, and as consequence of the hypotheses if the length scale decreases, time and velocity scale have to decrease as well. Therefore a Kolmogorov time scale and velocity scale can be defined as:

$$\eta = (\nu^3/\varepsilon)^{1/4} \tag{1.33}$$

$$u_\eta = (\varepsilon\nu)^{1/4} \tag{1.34}$$

$$\tau_\eta = (\nu/\varepsilon)^{1/2} \tag{1.35}$$

where ε is the mean energy dissipation rate. The Reynolds number of these scales is $\frac{\eta u_\eta}{\nu} = 1$. The third hypothesis is:

- **Kolmogorov's second similarity hypothesis.** In every turbulent flow at sufficiently high Reynolds number, the statistics of the motions of scale ℓ in the range $\ell_0 \gg \ell \gg \eta$ have a universal form that is uniquely determined by ε, independent of ν.

From the second similarity hypothesis, it can be derived that the energy spectrum in the inertial range ($\ell_0 > \ell > \eta$) should only depend on the length scale $\ell = 1/k$ and the energy dissipation rate ε and should be independent of ν. Therefore the energy spectrum should have the form:

$$E(k) = C\varepsilon^x k^y \tag{1.36}$$

where C is a constant that can be estimated using experimental data and it was found that $C = 1.5$ (Pope, 2000). x and y are exponents that need to be estimated which can be done by dimensional analysis, resulting in $x = 2/3$ and $y = -5/3$ and therefore the energy spectrum is:

$$E(k) \propto \varepsilon^{2/3} k^{-5/3}\,. \tag{1.37}$$

To derive scaling exponents for the structure functions (eqs. (1.24)-(1.25)), the similarity hypothesis and dimensionality analysis can be used, resulting in:

$$G_p(r) \propto (\varepsilon r)^{p/3} \tag{1.38}$$

$$S_p(\tau) \propto (\varepsilon \tau)^{p/2}\,. \tag{1.39}$$

Based on these results, Heisenberg (1948) and Yaglom (1949) derived a scaling for the variance of the acceleration components:

$$\langle a_i a_j \rangle = a_0 \varepsilon^{3/2} \nu^{-1/2} \delta_{ij} \tag{1.40}$$

where δ_{ij} is the Kronecker delta where $\delta_{ij} = 1$ if $i = j$ and 0 otherwise. a_0 is assumed to be a universal constant measured from data.

1.5 Intermittency

One assumption made in the K41 theory is that the velocity field fluctuations are self-similar at inertial-range scales. That is, the statistics of velocity fluctuations across different scales are independent of the time (Lagrange) or length (Euler) scale. If the statistics are scale-depend, the velocity fluctuations are intermittent. It is commonly know that turbulence does have intermittent features. These can be measured by structure functions which can

be defined in the Eulerian (eq. (1.24)) and Lagrangian (eq. (1.25)) setting. The predicted scaling laws by the Kolmogorov theory assume self-similarity and therefore do not include intermittency. Intermittency therefore can be seen by deviations of the predicted scaling for the structure functions (Toschi and Bodenschatz, 2009). Additionally, if turbulence would be self-similar, the flatness of acceleration PDFs would be independent of the Reynolds number, which is not the case as shown for example in Voth et al. (2002). More detail on intermittecy can be found in the book by Frisch (1995).

While the Heisenberg-Yaglom scaling assumes that a_0 is a universal constant, it has been shown that a_0 depends on the Reynolds number (Voth et al., 2002) as a result of intermittency.

Another way to highlight intermittency is shown in Mordant et al. (2002) and Bentkamp et al. (2019) where the authors have shown that the PDFs of the velocity increments change with the time lag τ. If τ is small, the PDF is closely related to the PDF of the acceleration, while if τ is large, the PDF is close to the velocity PDF.

1.6 Different Flow Types

After having discussed the fundamental concepts of fluid dynamics and turbulence, I will now discuss the underlying physics of the flow types that will be analysed in this thesis. These flow types are determined by the flow setup and the driving mechanism of a flow.

1.6.1 Von Kármán Flow

The von Kármán flow is an experimental setup that is used to approximate the theoretical concept of homogeneous isotropic turbulence. It consists of a water tank with two counter-rotating propellers installed in vertical direction. The measurements are taken in a small sub-volume in the centre of the vessel, more details on the setup can be found in section 2.1.2. As the propellers are installed along a single direction, an anisotropic large-scale motion is introduced. Ouellette et al. (2006) reported velocity statistics and show that large-scale anisotropies affect small-scale turbulence. A potential explanation for the anisotropy is presented in Voth et al. (2002). The fluid motion introduced by the propellers is a superposition of shearing and pumping modes. The shearing mode is caused by the counter-rotating

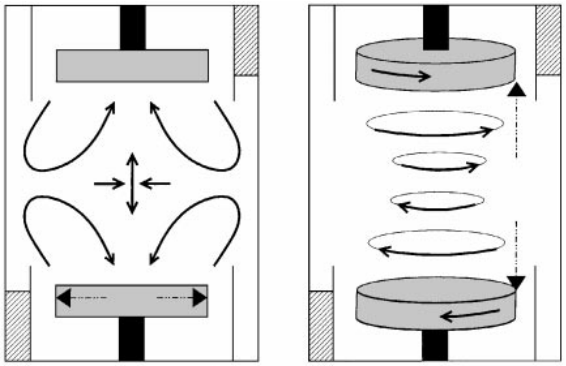

Figure 1.1: Pumping (right) and shearing (left) modes in a flow between two counter-rotating discs. Figure from Voth et al. (2002).

propellers where the fluid rotates in direction of the propeller, creating a shear layer in the middle of the flow chamber. Through the propeller motion, centrifugal pumping is introduced such that the fluid first flows inwards and subsequently upwards towards the propellers. A visualisation of these two modes can be found in figure 1.1.

1.6.2 Rayleigh-Bénard Convection

Rayleigh-Bénard convection (RBC) is a type of convection that occurs in a container when a fluid is heated from below and cooled from the top, a sketch of this setup is presented in figure 1.2. If the temperature difference is large enough, convection rolls develop due to the density differences at the top and bottom plates.

For this section, variables are dimensional and a non-dimensionalisation for this system is provided. This system can be described by the Boussinesq approximation (Oberbeck, 1879) where the density ρ is assumed to be a linear function of the temperature T of the fluid and is approximated by:

$$\rho(T) = \rho_{ref}\left(1 - \alpha(T - T_{ref})\right) \tag{1.41}$$

where ρ_{ref} is the density at the mean temperature T_{ref}, and α is the thermal expansion coefficient. In the Boussinesq approximation, it is assumed that density variations are only

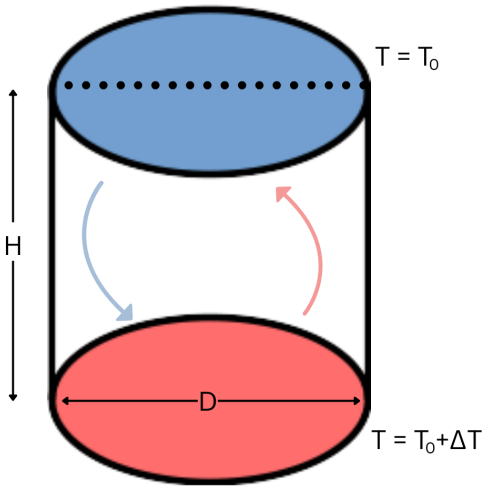

Figure 1.2: Sketch of a Rayleigh-Bénard convection. The top plate has a lower temperature than the bottom plate. Due to density differences, cold fluid falls while hot fluid rises, resulting in convection rolls.

significant in the buoyancy term, leading to the governing equations as follows:

$$\nabla \cdot \boldsymbol{u} = 0 \tag{1.42}$$

$$\partial_t \boldsymbol{u} + \boldsymbol{u} \cdot \nabla \boldsymbol{u} = -\nabla p + \nu \Delta \boldsymbol{u} + \alpha g (T - T_{ref}) \boldsymbol{e}_z \tag{1.43}$$

$$\partial_t T + \boldsymbol{u} \cdot \nabla T = \kappa \nabla^2 T \tag{1.44}$$

where g is the gravitational acceleration, $\boldsymbol{e_z}$ the unit vector in z-direction and κ the thermal diffusivity. This set of equations are the dimensional Navier-Stokes equations with the forcing term $\alpha g(T - T_{ref})\boldsymbol{e}_z$ which are coupled with the governing equation for the temperature field. To non-dimensionalise these equations, the container height H is used as a length scale, for the temperature the temperature difference between the top and bottom plate ΔT is used and the free fall velocity $U_f = (g\alpha \Delta T H)^{1/2}$ for the velocity:

$$\nabla^* \cdot \boldsymbol{u}^* = 0 \tag{1.45}$$

$$\partial_{t^*} \boldsymbol{u}^* + \boldsymbol{u}^* \cdot \nabla^* \boldsymbol{u}^* = -\nabla^* p^* + \frac{\sqrt{Pr}}{\sqrt{Ra}} \nabla^{*^2} \boldsymbol{u}^* + T^* - \boldsymbol{e}_z \tag{1.46}$$

$$\partial_{t^*} T^* + \boldsymbol{u}^* \cdot \nabla^* T^* = \frac{1}{\sqrt{RaPr}} \nabla^{*^2} T^* \tag{1.47}$$

where $()^*$ are non-dimensionless variables and the Prandtl number Pr and the Rayleigh

number Ra are defined as:

$$Pr = \nu/\kappa \tag{1.48}$$

$$Ra = \alpha g H^3 \Delta T/(\nu\kappa) \tag{1.49}$$

and can be used to define a free fall Reynolds number Re_f:

$$Re_f = \frac{U_f H}{\nu} = \sqrt{\frac{Ra}{Pr}}\,. \tag{1.50}$$

The Prandtl number indicates whether momentum diffusivity ($Pr > 1$) or thermal diffusivity ($Pr < 1$) is more dominant in the flow and is a descriptor the fluid. For $Pr > 1$ the velocity boundary layer is thicker compared to the thermal boundary layer, for $Pr < 1$ the thermal boundary layer is thicker compared to the velocity boundary layer (Grossmann and Lohse, 2000). The thermal boundary layer thickness λ_b is:

$$\lambda_b = H/(2Nu) \tag{1.51}$$

with Nu the Nusselt number which describes the ratio of the total heat transfer through convection and conduction to the heat transfer through conduction and is defined as:

$$Nu = \frac{\langle u_z T\rangle_A - \kappa\partial_z\langle T\rangle_A}{\kappa\Delta T/H} \tag{1.52}$$

where $\langle\cdot\rangle_A$ the horizontal average at a fixed height z. The Rayleigh number Ra is a measure of the thermal driving. If the Rayleigh number is below a critical value Ra_{crit}, no convection cell will form and the heat will be transferred through conduction. Ra_{crit} depends on the boundary conditions and the aspect ratio Γ of the cell . The aspect ratio is defined as:

$$\Gamma = D/H \tag{1.53}$$

where D is the diameter of the container.

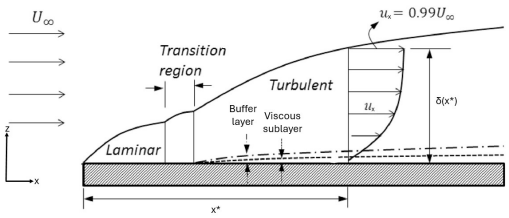

Figure 1.3: Sketch of the formation of a boundary layer. The fluid approached the surface with a free-stream velocity U_∞. The flow near the surface is slowed down due to viscous forces, resulting in a laminar boundary layer. Depending on flow conditions, this laminar boundary layer can transition to a turbulent boundary layer, which is the focus within this work. Figure modified from Shahmohamadi and Rashidi (2017)

1.6.3 Turbulent Boundary Layer

Turbulent boundary layers form when fluid flows over a surface and are present in many natural and industrial phenomena, like in a river bed or over an air plane wing. Initially, when a fluid approaches the surface with a free-stream velocity $\boldsymbol{U}_\infty$, usually in x-direction and defined as $\boldsymbol{U}_\infty = (U_\infty, 0, 0)$, the flow is slowed down by viscous forces near the boundary. The volume in which the flow is slower compared to the free stream velocity is called boundary layer (fig.1.3).

In the theoretical description of the boundary layer, it is assumed that the statistics are independent of the spanwise direction y. In literature, the spanwise direction would usually be in z-direction and the wall-normal direction would be in y-direction. However, the convectional coordinate system of the Rayleigh-Bénard convection is used for all described flow types here. With increasing distance from the wall, corresponding to the z-direction, the impact of viscous forces decreases, and the flow aligns with the free-stream velocity. This transition can be used to define the boundary layer thickness δ, which is the distance from the wall beyond which the effects of the wall are minimal. The thickness of the boundary layer grows with distance travelled over the surface and therefore is a function of x, as it can be seen in figure 1.3. The thickness of the boundary layer $\delta(x)$ can be defined in different ways, the most common is where the spanwise averaged velocity in x-direction reaches 99% of the free stream velocity:

$$\langle u_x(x, \delta(x)) \rangle_y = 0.99 U_\infty \ . \tag{1.54}$$

While in general the boundary layer thickness is a function of x, we will focus on a fully developed boundary layer, where the changes in the boundary layer thickness can be neglected.

Boundary layers can be divided into different sub-layers for which the velocity profiles can be derived. To compare different boundary layers, wall units can be used for a non-dimensionalisation. The wall units are defined for fully developed boundary layers where the statistics only depend on the wall distance z. They are defined as:

$$z^+ = \frac{u_\tau z}{\nu} \tag{1.55}$$

$$u^+ = \frac{u_x}{u_\tau} \tag{1.56}$$

where $u_\tau = \sqrt{\frac{\tau_W}{\rho}}$ the friction velocity and τ_W is the wall shear stress. Using the velocity friction, a friction Reynolds number is defined as:

$$Re_\tau = \frac{u_\tau \delta}{\nu} \tag{1.57}$$

which is commonly used to characterise boundary layer flows. The z^+ can also be interpreted as a local Reynolds number, indicating the relative importance of viscosity and the level of turbulence and thus can be used to split the boundary layer into different sub-layers. The different sub-layers can be defined as:

- Viscous sub-layer: $z^+ < 5$ (viscous stresses are dominating)
- Buffer layer: $5 < z^+ < 30$ (region between viscous sub-layer and logarithmic layer)
- Logarithmic layer (or log-law layer): $z^+ > 30$
- Outer layer: $z^+ > 50$ (viscous effects are negligible).

For the viscous sub-layer and the logarithmic layer, the mean velocity profile can be derived. For the viscous sub-layer, the velocity profile is linear:

$$u^+ = z^+ \tag{1.58}$$

and for the logarithmic layer, the mean velocity profile follows a logarithmic law:

$$u^+ = \frac{1}{\kappa} \ln z^+ + B \tag{1.59}$$

where B and κ are constants and estimated using data. It was found that $B \approx 5$ and for the von Kármán constant $\kappa \approx 0.41$ (Schlichting and Gersten, 2017). The log-law is a universal velocity profile that holds for wall-bounded flows. Similarly to the Kolmogorov theory, where the energy spectra only depends on the dissipation rate and viscosity, the log-law only depends on the distance to the wall and the friction velocity. An example velocity profile can be found in figure 2.6 (middle) for the dataset used within this thesis.

1.6.4 Magnetohydrodynamic Turbulence

This section is based on the book by Biskamp (2003). When fluids are electrically conducting, magnetic effects need to be taken into account when describing the flow. Therefore, the incompressible Navier-Stokes equations need to be coupled with the Maxwell equations. This results in adding the Lorentz force to the governing equation of the velocity field which can be split into an additional pressure term (absorbed in p in the equation below) and magnetic tension force. For the governing equation of the magnetic field, the curl of the electric field can be simplified using that the magnetic field and velocity field are divergence free. Overall, this results in:

$$\frac{\partial \boldsymbol{u}}{\partial t} + \boldsymbol{u} \cdot \nabla \boldsymbol{u} = -\nabla p + \boldsymbol{B} \cdot \nabla \boldsymbol{B} + \nu \nabla^2 \boldsymbol{u} + \boldsymbol{F_u} \tag{1.60}$$

$$\frac{\partial \boldsymbol{B}}{\partial t} + \boldsymbol{u} \cdot \nabla \boldsymbol{B} = \boldsymbol{B} \cdot \nabla \boldsymbol{u} + \mu \nabla^2 \boldsymbol{B} + \boldsymbol{F_b} \tag{1.61}$$

$$\nabla \cdot \boldsymbol{u} = 0 \tag{1.62}$$

$$\nabla \cdot \boldsymbol{B} = 0 \tag{1.63}$$

where $\boldsymbol{B}$ is the magnetic field, μ the magnetic diffusivity and $\boldsymbol{F_u}$ and $\boldsymbol{F_b}$ mechanic and electromagnetic external forces. In this thesis, no external electromagnetic forces are used, therefore $\boldsymbol{F_b} = 0$.The magnetic field is made up of a background field $\boldsymbol{B_0}$ and magnetic field fluctuations $\boldsymbol{b}$:

$$\boldsymbol{B} = \boldsymbol{B_0} + \boldsymbol{b}\,. \tag{1.64}$$

The additional term $\boldsymbol{B} \cdot \nabla \boldsymbol{B}$ in the governing equation of the velocity field is called magnetic tension, describing the force acting on bent magnetic field lines to straighten them. The

magnetic tension has its origin in the Lorentz force:

$$\boldsymbol{j} \times \boldsymbol{B} = \boldsymbol{B} \cdot \nabla \boldsymbol{B} - \nabla B^2/2 \tag{1.65}$$

where $\boldsymbol{j} = \nabla \times \boldsymbol{B}$ the current density and the term $-\nabla B^2/2$ is the magnetic pressure, absorbed in the pressure p in equation (1.60).

The terms $\boldsymbol{u} \cdot \nabla \boldsymbol{B}$ and $\boldsymbol{B} \cdot \nabla \boldsymbol{u}$ in the governing equation for the magnetic field are responsible for the transport of the magnetic field and stretching of the field lines respectively.

Similarly to the Prandtl number in Rayleigh-Bénard convection, a magnetic Prandtl number Pm can be defined:

$$Pm = \frac{\nu}{\mu} \tag{1.66}$$

determining the relative effects of kinematic viscosity and magnetic diffusivity.

In section 1.1, the energy flux was defined to describe how energy gets transferred across different scales. For MHD turbulence this transfer is influenced not only by the velocity field but also by the magnetic field. The total energy flux Π^ℓ is the sum of the kinetic energy flux Π^u and magnetic energy flux Π^b (Aluie, 2017; Offermans et al., 2018; Capocci et al., 2024):

$$\Pi^{\ell,u} = -\frac{\partial \bar{u}_i^\ell}{\partial x_j}\tau^\ell(u_i, u_j) + \frac{\partial \bar{u}_i^\ell}{\partial x_j}\tau^\ell(b_i, b_j) \tag{1.67}$$

$$\Pi^{\ell,b} = -\frac{\partial \bar{b}_i^\ell}{\partial x_j}\tau^\ell(b_i, u_j) + \frac{\partial \bar{b}_i^\ell}{\partial x_j}\tau^\ell(u_i, b_j) \tag{1.68}$$

$$\Pi^\ell = \Pi^{\ell,u} + \Pi^{\ell,b} \tag{1.69}$$

where $\tau^\ell(f_i, g_j)$ for f_i, g_j any of the velocity of magnetic field components, is the sub-grid scale stress tensor and defined as:

$$\tau^\ell(f_i, g_j) = \overline{f_i g_j}^\ell - \overline{f}_i^\ell \overline{g}_j^\ell \,. \tag{1.70}$$

1.7 Frenet-Serret Formulae

As seen in previous sections, turbulence is a complex phenomenon that acts across multiple scales. Therefore, we examined the statistics of multi-scale observables, specifically the curvature and torsion. These quantities are particularly useful as, when Lagrangian trajectories

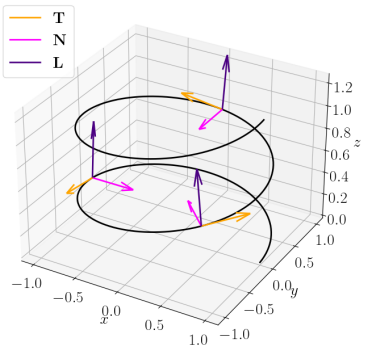

Figure 1.4: Sketch of the tangent (orange), normal (pink) and binormal (blue) vector along a spiral.

and Eulerian magnetic field lines and stream lines are treated as three-dimensional space curves, curvature and torsion provide a comprehensive description of these curves. The Frenet-Serret formulae describe these space curves as function of the arc length s with its tangent $\boldsymbol{T}$, normal vector $\boldsymbol{N}$ and binormal vector $\boldsymbol{L}$ (Bär, 2010).

$$\frac{d}{ds}\boldsymbol{T} = \kappa \boldsymbol{N} \ , \tag{1.71}$$

$$\frac{d}{ds}\boldsymbol{N} = -\kappa \boldsymbol{T} + \tau \boldsymbol{L} \ , \tag{1.72}$$

$$\frac{d}{ds}\boldsymbol{L} = -\tau \boldsymbol{N} \ , \tag{1.73}$$

where $\kappa = |d/ds\, \boldsymbol{T}|$ is the curvature and $\tau = |d/ds\, \boldsymbol{L}|$ the torsion. Since $\boldsymbol{T}$ is the tangent vector to the curve with respect to arc length, its rate of change will always be perpendicular to it, hence $\boldsymbol{N}$ is normal to $\boldsymbol{T}$, and similarly $\boldsymbol{L}$ is normal to $\boldsymbol{N}$. A sketch of these three vectors along a spiral can be found in figure 1.4. The derivative d/ds is the gradient in the direction flow, and therefore can be written as $\boldsymbol{T} \cdot \nabla$. Lagrangian trajectories are parametrised using the time t instead of the arc length, resulting in $\frac{d}{ds} = \frac{dt}{ds}\frac{d}{dt} = \frac{1}{|\boldsymbol{u}|}\frac{d}{dt}$. The curvature of a space curve is the inverse of the radius of the closest-fitting circle that approximates the curve at a point. The torsion measures how much a space curve twists.

We are interested in the effects on anisotropy of different flows on the geometry of particle trajectories, stream lines and magnetic field lines as most flows in nature or engineering applications are not statistically homogeneous and isotropic. However, curvature and torsion

are global properties where the contributions to the total curvature stemming from the rate of change of the tangent vector to the curve in each coordinate direction is retained and it can be expected that the geometry of the flow does not have an effect on the statistics (at least for small levels of anisotropy). Therefore, we introduce the curvature vector in the next section and consider the statistics of its projections onto coordinate directions defined by the flow configurations.

1.7.1 Curvature Vector

As introduced above, the curvature is defined as the magnitude of the rate of change of the tangent vector with respect to the arc length of the curve (Pressley, 2001). Inspired by the definition of the signed curvature for planar curves and since the arc length derivative of the tangent vector is always perpendicular to the tangent vector, we define the curvature vector as the derivative of the tangent with respect to the arc length $d/ds\,\boldsymbol{T}$

$$\boldsymbol{\kappa} = \frac{d}{ds}\boldsymbol{T}\,. \tag{1.74}$$

This vector is parallel to the normal vector, and perpendicular of the circle that locally approximates the space curve, indicating in which direction a trajectory, stream line or magnetic field line curves.

For Lagrangian trajectories, the tangent is the normalised velocity $\boldsymbol{T} = \frac{\boldsymbol{u}}{|\boldsymbol{u}|}$ and therefore the curvature vector is:

$$\boldsymbol{\kappa} = \frac{1}{|\boldsymbol{u}|}\frac{d}{dt}\frac{\boldsymbol{u}}{|\boldsymbol{u}|} \tag{1.75}$$

$$= \frac{\boldsymbol{u}\times\boldsymbol{a}}{|\boldsymbol{u}|^3}\,, \tag{1.76}$$

where $\boldsymbol{a}$ is the acceleration. This vector is perpendicular to the velocity $\boldsymbol{u}$ and the acceleration vector $\boldsymbol{a}$.

For the stream lines of a velocity field, the tangent is given by $\boldsymbol{T} = \frac{\boldsymbol{u}}{|\boldsymbol{u}|} = \hat{\boldsymbol{u}}$, for magnetic field lines this would be $\boldsymbol{T} = \frac{\boldsymbol{b}}{|\boldsymbol{b}|} = \hat{\boldsymbol{b}}$. The following derivation will focus on the stream lines and the derivation of magnetic field lines is analogous. By definition of the curvature vector

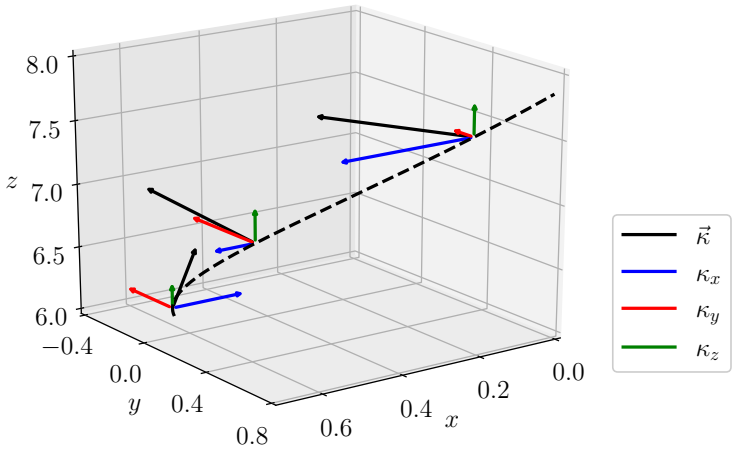

Figure 1.5: Curvature vector of a trajectory and projections onto the x-, y- and z- directions. The dashed line represents a space curve, the colours indicate the different directions, and curvature vector, as defined in equation (1.78), is shown in black.

and using that $\partial_s = \boldsymbol{T} \cdot \nabla$, the curvature vector in the Eulerian frame of reference is:

$$\boldsymbol{\kappa} = \hat{\boldsymbol{u}} \cdot \nabla \hat{\boldsymbol{u}} \,. \tag{1.77}$$

To probe the effect of large-scale coherent flow structures and more generally anisotropy on the geometry of Lagrangian particle trajectories (and stream lines and magnetic field lines), we will discuss the statistics of the projection of this vector onto the x-, y- and z-directions, respectively, visualised for an example Lagrangian trajectory in figure 1.5:

$$\begin{aligned}
\kappa_x &= \frac{1}{|\boldsymbol{u}|^3}(u_y a_z - u_z a_y) \,, \\
\kappa_y &= \frac{1}{|\boldsymbol{u}|^3}(u_z a_x - u_x a_z) \,, \\
\kappa_z &= \frac{1}{|\boldsymbol{u}|^3}(u_x a_y - u_y a_x) \,.
\end{aligned} \tag{1.78}$$

The curvature vector quantifies what physical intuition would tell us about the geometry of particle trajectories in configurations with a strong mean flow. For instance, by equation (1.78) a strong unidirectional flow should lead to smaller changes in the tangent vector to the curve in the mean flow direction and hence one may expect a higher probability of small values of the curvature in this direction compared to the other coordinate directions.

Assuming Gaussian statistics allows us to derive the power laws for the PDFs of the curvature vector components based on equation (1.78). For the right tail, the same arguments as for the full curvature, following (Xu et al., 2007), can be applied, resulting in a -2.5 power law. For the left tail, we note that each component can be defined as the signed curvature of a 2D space curve. Assuming that small curvature events are determined by small values of the normal acceleration, this leads to the curvature statistics being determined by a single acceleration component, normal to the 2D velocity, resulting in a constant PDF of the curvature vector components for small values of the curvature.

1.7.2 Curvature and Torsion in the Lagrangian Frame of Reference

Using the parametrisation of time, the curvature and torsion of a Lagrangian trajectory become:

$$\kappa = \frac{|\boldsymbol{u} \times \boldsymbol{a}|}{|\boldsymbol{u}|^3} = \frac{|\boldsymbol{a}_n|}{|\boldsymbol{u}|^2} \tag{1.79}$$

$$\tau = \frac{\boldsymbol{u} \cdot (\boldsymbol{a} \times \dot{\boldsymbol{a}})}{(\boldsymbol{u} \cdot \boldsymbol{u})^3 \kappa^2} \,, \tag{1.80}$$

where $\boldsymbol{a}_n$ is the acceleration vector normal to the velocity vector, and $\dot{\boldsymbol{a}}$ denotes the total time derivative of the acceleration. The curvature is the magnitude of the curvature vector defined in equation (1.76).

1.7.3 Curvature in the Eulerian Frame of Reference

Based on the definition of the curvature vector $\boldsymbol{\kappa}$ (eq. (1.77)), the curvature of stream lines can be defined as:

$$\kappa = |\hat{\boldsymbol{u}} \cdot \nabla \hat{\boldsymbol{u}}| \,. \tag{1.81}$$

In literature, two other analytically equivalent versions of the curvature are discussed. These are:

$$\kappa = \frac{|\boldsymbol{u} \times (\boldsymbol{u} \cdot \nabla \boldsymbol{u})|}{|\boldsymbol{u}|^3} \quad \text{and} \tag{1.82}$$

$$\kappa = |\hat{\boldsymbol{u}} \times \hat{\boldsymbol{u}} \cdot \nabla \hat{\boldsymbol{u}}| \,. \tag{1.83}$$

In the following, I will prove that these two versions are indeed equivalent to equation (1.81). First, I will show that $\hat{\boldsymbol{u}} \perp \hat{\boldsymbol{u}} \cdot \nabla \hat{\boldsymbol{u}}$ by showing that the dot product is equals zero:

$$\begin{aligned}
\hat{\boldsymbol{u}} \cdot (\hat{\boldsymbol{u}} \cdot \nabla \hat{\boldsymbol{u}}) &= \hat{u}_j \hat{u}_i \partial_i \partial \hat{u}_j && (1.84)\\
&= \frac{1}{2} \hat{u}_i \partial_i (\hat{u}_j \hat{u}_j) && (1.85)\\
&= \frac{1}{2} \hat{u}_i \partial_i 1 && (1.86)\\
&= 0 && (1.87)
\end{aligned}$$

where summation over repeated indices is implied. Using this and the definition of the cross product:

$$\begin{aligned}
\kappa &= |\hat{\boldsymbol{u}} \cdot \nabla \hat{\boldsymbol{u}}| && (1.88)\\
&= |\hat{\boldsymbol{u}}||\hat{\boldsymbol{u}} \cdot \nabla \hat{\boldsymbol{u}}| \sin \frac{\pi}{2} && (1.89)\\
&= |\hat{\boldsymbol{u}} \times (\hat{\boldsymbol{u}} \cdot \nabla \hat{\boldsymbol{u}})| \,. && (1.90)
\end{aligned}$$

As $\hat{\boldsymbol{u}} = \frac{\boldsymbol{u}}{|\boldsymbol{u}|}$, this can be rewritten as:

$$\begin{aligned}
\kappa &= \left| \frac{\boldsymbol{u}}{|\boldsymbol{u}|} \times \left(\frac{\boldsymbol{u}}{|\boldsymbol{u}|} \cdot \nabla \frac{\boldsymbol{u}}{|\boldsymbol{u}|} \right) \right| && (1.91)\\
&= \frac{\left| \boldsymbol{u} \times \left(\boldsymbol{u} \cdot \nabla \frac{\boldsymbol{u}}{|\boldsymbol{u}|} \right) \right|}{|\boldsymbol{u}|^2} && (1.92)\\
&= \frac{\left| \boldsymbol{u} \times \left(\boldsymbol{u} \cdot \frac{1}{|\boldsymbol{u}|} \nabla \boldsymbol{u} + \boldsymbol{u} \cdot (\nabla \frac{1}{|\boldsymbol{u}|}) \boldsymbol{u} \right) \right|}{|\boldsymbol{u}|^2} && (1.93)\\
&= \frac{|\boldsymbol{u} \times (\boldsymbol{u} \cdot \nabla \boldsymbol{u})|}{|\boldsymbol{u}|^3} + \frac{\left| \boldsymbol{u} \times \left(\boldsymbol{u} \cdot (\nabla \frac{1}{|\boldsymbol{u}|}) \right) \boldsymbol{u} \right|}{|\boldsymbol{u}|^2} && (1.94)\\
&= \frac{|\boldsymbol{u} \times (\boldsymbol{u} \cdot \nabla \boldsymbol{u})|}{|\boldsymbol{u}|^3} \,. && (1.95)\\
& && (1.96)
\end{aligned}$$

This proof only works for the scalar version of the curvature. However, we will see that, when numerically implementing the curvature, only equation (1.95) accurately calculates the curvature. This will be further discussed in section 3.3.2.Therefore, we analyse a different

curvature vector to equation (1.77) defined as:

$$\boldsymbol{\kappa} = \frac{\boldsymbol{u} \times (\boldsymbol{u} \cdot \nabla \boldsymbol{u})}{|\boldsymbol{u}|^3} \,. \tag{1.97}$$

This vector is parallel to the binormal vector, and therefore the interpretation of curvature vector statistics for the magnetic field lines and stream lines is different. This version of the curvature vector is normal to the plane of a local circle that approximates the curve.

1.7.4 Literature on Curvature and Torsion Statistics

Curvature and Torsion statistics have been discussed in previous works for Lagrangian trajectories and magnetic field lines.

For Lagrangian particle trajectories, curvature statistics have been calculated for numerical simulations of homogeneous and isotropic turbulence (Braun et al., 2006), for experimental data of von Kármán flow (Xu et al., 2007), experimental and numerical data of Rayleigh-Bénard convection (Alards et al., 2017) and numerical data of magnetohydrodynamic turbulence (Busse, 2009). Torsion statistics have been calculated of numerical simulations of homogeneous and isotropic turbulence (Scagliarini, 2011) and Rayleigh-Bénard convection (Alards et al., 2017). Across all datasets, the same seemingly universal form for the PDFs of curvature and torsion have been found, with low-curvature tails proportional to κ and high-curvature tails proportional to $\kappa^{-2.5}$, and low-torsion tails proportional to τ^0 and high-torsion tails proportional to τ^{-3}.

Material loops are an additional method for passive tracking of flows. As these can be described as space curves, curvature and torsion can be used to describe these fully. Bentkamp et al. (2022) calculated curvature statistics of material loops in turbulence and found that the curvature PDF is linear for small curvature values and $\propto \kappa^{-2.62}$. To predict these tails, the authors used large-deviations statistics of finite-time Lyapunov exponents of the flow and compared these results with results based on the Kraichnan model.

For the curvature of magnetic field lines, Schekochihin et al. (2001, 2002, 2004) first discussed the curvature of magnetic field lines of the turbulent small-scale kinematic dynamo. The authors derived an equation for the curvature PDF based on the Kazantsev-Kraichnan model, which will be discussed further in the next section, and compared the results with

numerical data and found that the PDF for high curvature values is $\propto \kappa^{-20.7}$. They also found that the curvature and the magnetic field strength are anti-correlated. In Schekochihin et al. (2004), it was also mentioned that care needs taken when implementing the curvature and taking the derivative of the unit vector of the magnetic field should be avoided. Later Yang et al. (2019) calculated the curvature PDFs of magnetic field lines of turbulent magnetohydrodynamic (MHD) simulations and turbulent plasma. Yang et al. (2019) found that the curvature PDF is linear for small curvature values and proportional to $\kappa^{-2.5}$ for high curvature values. An model adapted from Xu et al. (2007) for the curvature of Lagrangian trajectories to the curvature of magnetic field lines was also presented, providing an explanation for the found tails of the curvature PDF. Based on the work by Yang et al. (2019), Bandyopadhyay et al. (2020) calculated curvature PDFs of Magnetospheric Multiscale Mission (MMS) data, finding the same power laws for the curvature PDF as Yang et al. (2019). Bandyopadhyay et al. (2020) also reconfirmed the anti-correlation of curvature and magnetic field strength and additionally have shown that the normal force and curvature are strongly correlated. Huang et al. (2020) also provided measurements of the curvature statistics of MMS data, finding that the PDF is $\propto \kappa^{0.33}$ for small curvature values and $\propto \kappa^{-2.16}$ for large values of the curvature, claiming that results agree well with the power laws measured by Yang et al. (2019). Additionally Huang et al. (2020) fitted a double Pareto log-normal to the curvature PDF, resulting in a good agreement with the found power laws. An additional measurement of curvature statistics of magnetosheath data can be found in Ji et al. (2022), where for small values of curvature, the PDF is $\propto \kappa^{0.8}$ and for large curvature values, the PDF is $\propto \kappa^{-2.1}$. Ji et al. (2022) compare the high curvature PDF to the PDF of 2D MHD data in Yang et al. (2019) as magnetosheath data is strongly anisotropic. The work by Yuen and Lazarian (2020) focused on curvature statistics of compressible MHD, where it was found that the exponent of the right tail of the curvature PDF depends on the Alfvénic Mach number M_A, where the exponent varies between $\approx$ -2.5 and -0.7 for M_A between $\approx$ 0.2 and 1.5. Lemoine (2023) also calculated curvature statistics where the right tail of the curvature PDF is $\approx\propto \kappa^{-2.5}$ and connected particle transport with sharp magnetic field line bends.

1.7.5 Modelling of Curvature Probability Density Functions

In a set of different papers Schekochihin et al. (2001, 2002, 2004) derived a model for the curvature PDF of the magnetic field lines of the turbulent *kinematic* dynamo. A kinematic dynamo generates and maintains a magnetic field through moving electrically conducting fluid. Schekochihin *et al.* model the advecting velocity by a Gaussian random field that is δ-correlated in time, also known as the Kazantsev-Kraichnan model and the magnetic field as a passively advected vector field. This allows to derive a Fokker-Planck equation in the diffusion free regime for the curvature PDF. In the stationary limit they obtain:

$$P^{(\mathrm{st})}(\kappa) = \mathrm{const}\frac{1}{(1+\kappa^2)^{10/7}} \,. \tag{1.98}$$

This results in a $-20/7 = -2.86$ power law for the right tail of the PDFs representing high curvature values and constant for the left tail that describes low curvature values.

The model PDF agrees well with numerical simulations of 3D MHD turbulence for grid sizes $N = 128^3$ (Schekochihin et al., 2001, 2002) and $N = 256^3$ (Schekochihin et al., 2004) with varying large-scale Reynolds number between 1.8 and 450 and according to that varying magnetic Prandtl number between 2500 and 1. Additionally, they find that the magnetic field strength and curvature are strongly anticorrelated. Geometrically, this means that the magnetic field mainly grows along straight parts of the field lines and the magnetic field strength in the curved parts stays small.

A second model for the curvature PDF was derived for Lagrangian trajectories in homogeneous and isotropic turbulence by Xu et al. (2007), assuming velocity and acceleration components of Lagrangian tracer particles to be statistically independent Gaussian random variables. In direct analogy to the derivation by Xu et al. (2007), a model PDF for the curvature of magnetic field lines can be derived. For the PDF of the curvature of Lagrangian particles, we assume that the velocity components and acceleration components are independent random Gaussian variables. For the curvature of magnetic field lines, this assumption is that the magnetic field fluctuations and components of the magnetic tension $\boldsymbol{b}\cdot\nabla\boldsymbol{b}$ are independent random Gaussian variables. In the following derivation, I focus on the curvature of Lagrangian trajectories. The velocity components being Gaussian, results in an inverse χ^2-distribution of order three for $\frac{1}{|\boldsymbol{u}|^2}$. As a_n is the normal acceleration perpendicular to $\boldsymbol{u}$

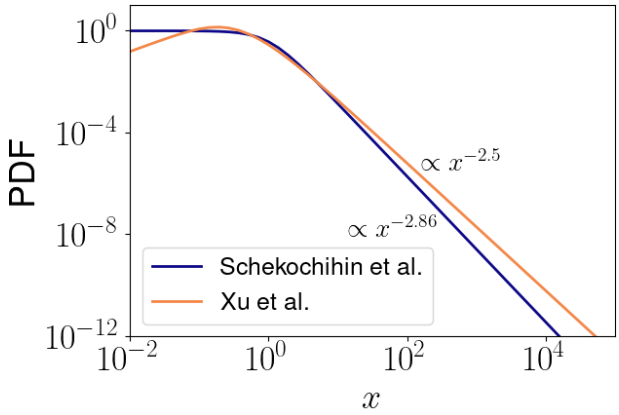

Figure 1.6: Comparison of the model PDFs for the non-dimensionalised curvature $x = \kappa \frac{\sigma_{u^2}}{\sigma_{a_n}}$ derived by Schekochihin et al. (2004) (blue) and Xu et al. (2007)(orange).

and provided we assume isotropy, a_n can be represented by two arbitrary components of the acceleration vector and therefore a_n is χ distributed of order two. As statistical independence of the different components is assumed, the PDF of the non-dimensionalised curvature $x = \kappa \frac{\sigma_{u^2}}{\sigma_{a_n}}$ can be calculated as:

$$P(x) = \frac{e^{x^{-2}/16}}{16\sqrt{2\pi}x^4}\left(\left(3+\frac{1}{2x^2}\right)K_{3/4}\left(\frac{1}{16x^2}\right) - \left(5+\frac{1}{2x^2}\right)K_{1/4}\left(\frac{1}{16x^2}\right)\right) . \quad (1.99)$$

Either taking the limits $x \to 0$ and $x \to \infty$ in the above expression or, more straightforwardly, with the same arguments as put forward by Xu et al. (2007) for the curvature of Lagrangian trajectories and Yang et al. (2019) for the curvature of magnetic field lines, one can now derive expressions for the tails of the PDFs. For the left, low-curvature tail we assume $a_n \to 0$ while $\boldsymbol{u}$ remains finite, and hence that the limiting behaviour of a_n determines the low-curvature tail of the PDF. As the components of a_n are assumed to be Gaussian distributed, this results in $p(\kappa) \propto \kappa$ for small κ. For the high-curvature tail we assume $|\boldsymbol{u}| \to 0$, while a_n remains constant. As the components of $\boldsymbol{u}$ were also assumed to be Gaussian distributed, a Taylor expansion of the resulting χ^2-distribution of order three of $|\boldsymbol{u}|^2$ results in $p(\kappa) \propto \kappa^{-2.5}$ for large values of κ.

In what follows, we highlight differences, similarities and limitations of the two models. While both models are based on Gaussian statistics, the assumptions differ slightly. The Schekochihin model assumes a velocity field that is δ-correlated in time and the magnetic

field to be passively advected, while the model following the derivation by Xu et al. (2007) assumes independent Gaussian random variables for the magnetic field and magnetic tension terms and no assumptions are being made for the flow. This results in different PDFs with different power laws for the tails. The predicted power-law tails for high curvature values with exponents -2.86 for the Schekochihin model and -2.5 for the Xu model differ measurably (fig. 1.6). For small values of the curvature the models differ significantly. As we shall see, while the Xu model aligns indeed with the both tails of curvature PDFs of magnetic field lines, the model by Schekochihin does not align with data with a predicted constant PDF for small values of the curvature. By focusing on the statistics of the curvature peaks (isolated spikes of high curvature along a loop) and connecting these with its finite-time Lyapunov exponents, Bentkamp et al. (2022) modified the model by Schekochihin using finite-time Lyapunov exponents large-deviation statistics, resulting in a linear PDF for small values of the curvature and the PDF being $\propto \kappa^{-2.57}$ for high curvature values.

The assumptions of Gaussian statistics for velocity, acceleration, magnetic field fluctuations and magnetic tension components are generally not true and will discussed in the respective results chapters.

1.8 Thesis Outline

In the next chapter, the datasets provided by collaborators will be presented (chapter 2). This includes experimental datasets of von Kármán flow, Rayleigh-Bénard convection, and a turbulent boundary layer, as well as numerical datasets of magnetohydrodynamic turbulence.

In chapter 3, the numerical methods used for the analysis in this work are outlined, along with the results of appropriate numerical tests.

Chapters 4-6 present the results of curvature statistics in different turbulent flows. Chapter 4 provides a detailed comparison of velocity, acceleration, curvature, and torsion statistics across the different experimental datasets. This includes an analysis of the effect of large-scale flow reversals on the curvature and torsion PDFs, which mostly affect small curvature and high torsion events. Additionally, I analyse the effect of anisotropy through the statistics of the curvature vector, finding that a mean flow, as observed in the boundary layer, has the biggest effect on the curvature vector statistics.

Chapter 5 focuses on statistics in magnetohydrodynamic turbulence. The curvature statistics of magnetic field lines and streamlines are presented, along with the statistics of velocity fluctuations, inertial term components, magnetic field fluctuations, and magnetic tension components. Lastly, the effect of anisotropy introduced by a strong magnetic background field is analysed. A strong magnetic background field suppresses high curvature of field lines in the direction of the background field, indicating the suppression of magnetic field fluctuations parallel to it.

As the previous two chapters will have shown that the assumptions for existing models of the curvature PDF are not fulfilled, chapter 6 focuses on an extension of existing models. This extension accounts for intermittency by decomposing the full ensemble into smaller sub-ensembles. We will see that in each sub-ensemble, the model assumptions are fulfilled, leading to a closed-form expression for the curvature PDF of the whole ensemble. This improves previous models by approximately 30%.

In the concluding chapter 7, the key results are summarised and potential directions for future projects are provided.

Chapter 2

Datasets

In this chapter, I will introduce the experimental and numerical datasets provided by our collaborators which were used for the analysis in this thesis. This includes an overview of the experimental configurations employed by Daniel Schanz, Andreas Schröder, Daniel Garaboa Paz, Johannes Bosbach, Florian Huhn, Matthew Bross, Matteo Novara and Christian J. Kähler (Schröder et al., 2022; Bosbach et al., 2021; Schanz et al., 2019), as well as the direct numerical simulations conducted by Damiano Capocci (Capocci et al., 2024; Capocci, 2024).

2.1 Experimental Data

Four different experimental datasets of three different flow types are analysed here. They consist of a turbulent von Kármán flow (vK), Rayleigh-Bénard convection (RBC) at two different Rayleigh numbers and a turbulent zero-pressure-gradient (ZPG) boundary layer over a flat plate. The experimental setups for the different flow types are described in sections 2.1.2- 2.1.4 and key properties and observables of the different configurations are provided in table 2.1. To aid with the comparison of the datasets a global coordinate system is used. That is the standard Rayleigh-Bénard convection setup where x- and y-directions define the horizontal plane and the z-direction is the vertical direction normal to the bottom plate. The coordinate system for the boundary layer is defined such that it has its wall-normal direction in z-direction rather than the commonly used y-direction. For the von Kármán flow the propellers are located along the z-axis.

As all of the experimental campaigns are of Lagrangian nature where tracer particles follow the flow, Lagrangian particle tracking needs to be applied (Schanz et al., 2016). This allows to generate trajectories of particles following the flow using snapshots of the flow recordings. In particular, for the experimental datasets presented here, the Shake-The-Box algorithm (Schröder and Schanz, 2023) is applied. This was done by our collaborators and the provided datasets include the full particle trajectories. The Shake-The-Box (STB) algorithm is based on a temporal predictor-corrector scheme, where the predicted positions of the next timestep are 'shaken' to match the actual particle positions in the next snapshot. A more detailed discussion of this method can be found in Schröder and Schanz (2023); Wieneke (2012); Jahn et al. (2021).

In general, STB allows tracking particles and generating long particle trajectories in high densities with up to 100,000 particles per megapixel camera resolution while also avoiding to generate false, also known as ghost, trajectories (Schanz et al., 2016). Histograms of the trajectory lengths for the datasets discussed below are shown in figure 2.1, highlighting the amount of trajectories captured by STB and the tracking capability over extended periods.

2.1.1 Estimation of Experimental Error

To estimate the experimental error for all four datasets, we use spectral analysis of the particle positions (Gesemann et al., 2016) where the third derivative of the particle position is assumed to be noise (Kalman, 1960). The experimental error is given by the noise level of the amplitude spectrum, the spectrum has a negative slope until it reaches a constant plateau at high frequencies. This plateau represents noise, therefore the height of the plateau estimates the experimental positional error Δx. The frequency of where this transition occurs is called crossover frequency f_c and will be used as a smoothing parameter when fitting trajectories (sec. 3.1.3).

This error estimation could lead to inaccuracies in torsion measurements, as the third derivative of particle positions appears in the numerator of the torsion calculation. In section 3.3.2, I will present tests of the implemented torsion calculation to ensure numerical accuracy. This issue will be revisited when presenting torsion PDFs, including a comparison with DNS results from the literature.

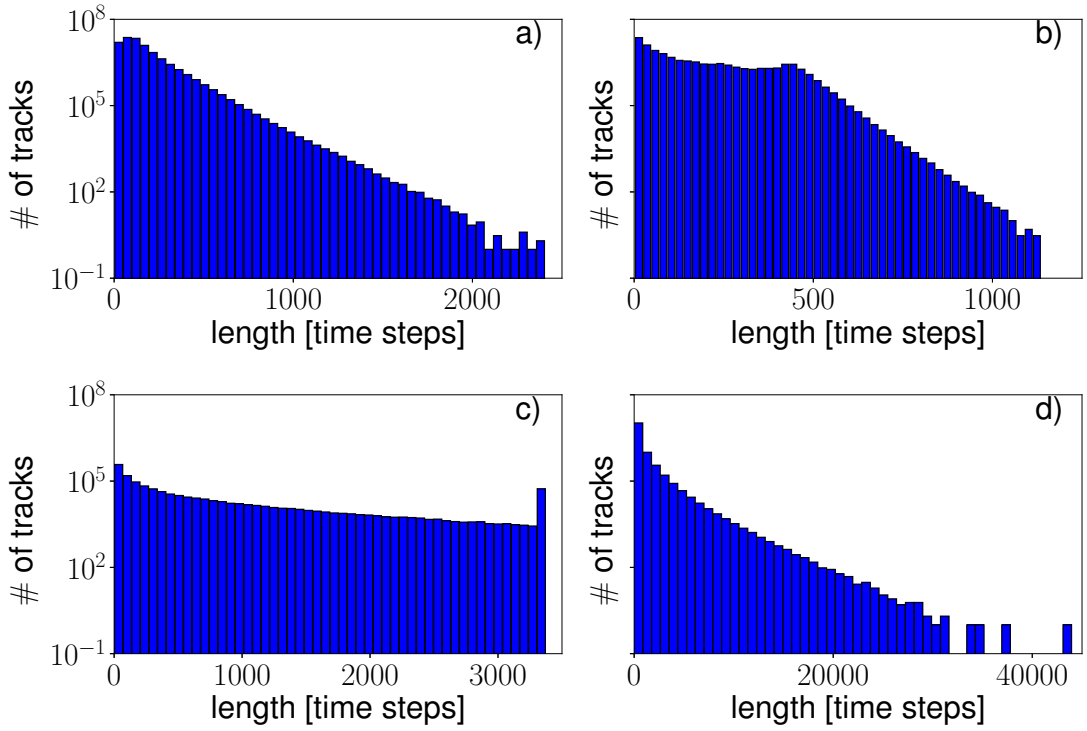

Figure 2.1: Histograms of trajectory lengths for the full measurement volume for a) von Kármán flow, b) boundary layer, c) RBC I, d) RBC II. For the analysis only trajectories with a minimal length of 100 time steps are considered.

	vK	RBC I	RBC II	ZPG BL
Re_λ	270	147	186	108
Re_τ	–	–	–	2295
τ_η [s]	0.013	0.35	0.18	0.0023
f [Hz]	1250	20	30	1000
$\tau_\eta \cdot f$	16.25	7	5.4	2.3
η [mm]	0.1	2.3	1.7	0.186
Δx [μm]	3	22	24	30
$\eta/\Delta x$	33	96	70	6.2
f_c	$(0.15, 0.15, 0.18)$	$(0.18, 0.18, 0.18)$	$(0.22, 0.22, 0.22)$	$(0.25, 0.2, 0.25)$
ℓ [μm]	20	300	220	300
η/ℓ	5	0.77	0.77	0.62
$St[10^{-3}]$	0.1	0.80 ± 0.17	0.80 ± 0.17	10
f_p [Hz]	0.5	–	–	–
$\boldsymbol{U}_\infty$ [m/s]	–	–	–	$(7, 0, 0)$
$Ra[10^8]$	–	5.25 ± 0.06	15.3 ± 0.3	–
Pr	–	0.7	0.7	–
ΔT [K]	–	4.03 ± 0.06	11.8 ± 0.2	–
Γ	–	1	1	–
λ_b [mm]	–	11.5	8.5	–
V [cm^3]	$0.4 \times 0.15 \times 0.4$	$55^2\pi \times 110$	$55^2\pi \times 110$	$280 \times 80 \times 25$
V_m [cm^3]	$0.4 \times 0.15 \times 0.4$	$52.5^2\pi \times 104.5$	$52.5^2\pi \times 104.5$	$100 \times 80 \times 1$
N	92739514	1287242	12150782	99286611
N_p	7347897506	234735856	748721661	4754436563

Table 2.1: Parameters and key observables of the experimental datasets, von Kármán flow (vK), Rayleigh-Bénard convection with different Raleigh numbers (RBC I and RBC II) and the turbulent ZPG boundary layer. The Taylor-scale Reynolds number is $Re_\lambda = \sqrt{15}(U_{\text{rms}})^2\eta^2/\nu^2$ with U_{rms} the root-mean-square of the velocity fluctuations in the different directions, η the Kolmogorov length scale, τ_η the Kolmogorov time scale and ν the viscosity. The friction Reynolds number is $Re_\tau = \frac{u_\tau \delta}{\nu}$, with $u_\tau = \sqrt{\tau_W/\rho}$ where τ_W is the wall-shear stress, δ the boundary-layer thickness and ρ the density. The camera and sampling frequency is f and Δx the experimental error estimated spectrally as noise (Gesemann et al., 2016) where the height of the spectra when it becomes constant and the frequency of this transition is the crossover frequency f_c. The spatial uncertainty estimated using smooth correlation functions with expected zero-crossings is ℓ, an explanation of this parameter can be found in sec. 3.1.2. The ratio of the particles' response time and the time scale of the flow is the Stokes number St (eq. (1.9)). Flow type-specific properties are the propeller frequency f_p for von Kármán flow and for the boundary layer the free stream velocity $\boldsymbol{U}_\infty$. For RBC, we have the Rayleigh number $Ra = g\alpha\Delta T H^3/(\nu\kappa)$, and the Prandtl number is $Pr = \nu/\kappa$, with g the gravitational acceleration, α the isobaric expansion coefficient, κ the thermal diffusivity, H the cell height and ΔT the temperature difference between top and bottom plate. The aspect ratio is given by Γ and $\lambda_b = H/(2Nu)$ is the thermal boundary layer thickness where Nu is the Nusselt number. The volume V is the volume captured by the camera systems, while V_m the sub-volume considered for calculations of presented statistics. The total number of trajectories in the full measurement volume V is denoted by N with distributions of trajectory lengths shown in figure 2.1. The number of datapoints N_p considered in the analysis only includes points in the sub-volume V_m and from trajectories that are longer than 100 timesteps.

2.1.2 Von Kármán Flow

The dataset of the von Kármán flow was generated at the von Kármán facility at the Max Planck Institute Göttingen by the German Aerospace Center (DLR) Göttingen (Schröder et al., 2022). The experimental setup consisted of a water tank with 500 mm diameter with two counter rotating propellers installed along the z-axis, rotating with a frequency of 0.5 Hz (fig. 2.2). This results in a Taylor Reynolds number of 270. Cooling plates at the top and bottom of the chamber ensured a constant temperature in the flow chamber with tubes being connected to the these plates. This allowed filling and draining of the flow chamber as required to remove unwanted air bubbles and to add tracer particles. The tracer particles were polystyrene Dynoseeds TS20 with 20 μm diameter which are nearly neutrally buoyant in water with a density of $\rho = 1.05$ g/cm^3. In the given flow conditions, this resulted in a Stokes number $St \approx 10^{-4}$ which allowed us to neglect any effects the particles might have on the flow in the analysis. The propeller movement induced a small volume in the centre of the chamber where turbulence can be assumed to be approximately homogeneous and isotropic (see dashed circle in the right panel of fig. 2.2). This small volume was illuminated by a high-frequency laser where a camera system of four Phantom v640 cameras operating at 1250 Hz recorded the positions of the illuminated particles in the sub-volume. Due to memory limitations of the cameras, the maximum length of a recording was 1.12 s, containing 14,000 snapshots. The recordings of several runs were then processed by the Shake-the-Box-algorithm, generating trajectories up to $\approx$ 2500 time steps long. The histogram of the trajectory lengths can be found in figure 2.1 a) and a visualisation of a subset of particle trajectories colour-coded by the velocity is presented in figure 2.3.

2.1.3 Rayleigh-Bénard Convection

The experiments for the two datasets of a Rayleigh-Bénard convection, referred to as RBC I and RBC II, were conducted at the DLR Göttingen (Bosbach et al., 2021) in a cylindrical Rayleigh-Bénard convection cell aspect ratio of $\Gamma = 1$ and height $H = 1.1$ m. The bottom plate was an electrically heated aluminium plate to ensure constant heating, for the top plate a transparent water perfused plate was installed for cooling purposes. The cylinder was filled with air at atmospheric pressure leading to a Prandtl number of $Pr = 0.7$. The tracer

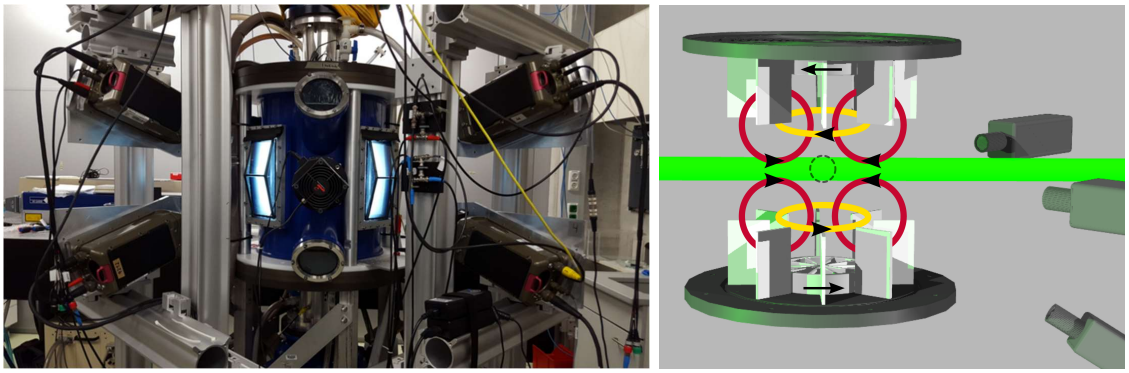

Figure 2.2: Left: Experimental setup of the von Kármán facility at the MPI Göttingen including the water tank with the camera setup, figure from Buchwald et al. (2022). Right: Sketch of experimental setup and view inside the water tank. The fluid is swirled by the two propellers located at the top and bottom of the water tank. In a small sub-volume in the middle of the flow chamber, indicated by the dashed circle, turbulence can be assumed to be approximately homogeneous and isotropic, figure from Jucha (2014).

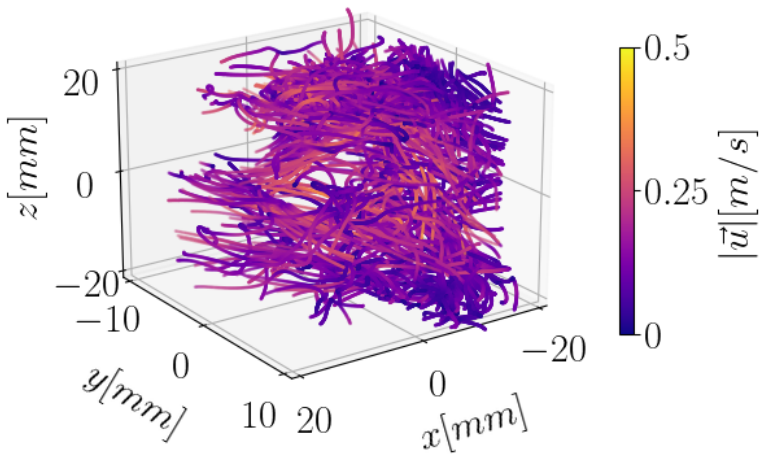

Figure 2.3: Visualisation of a subset of particle trajectories in von Kármán flow. The color indicates the magnitude of the velocity, darker shades (purple) indicating small velocities and light colors higher velocities (yellow).

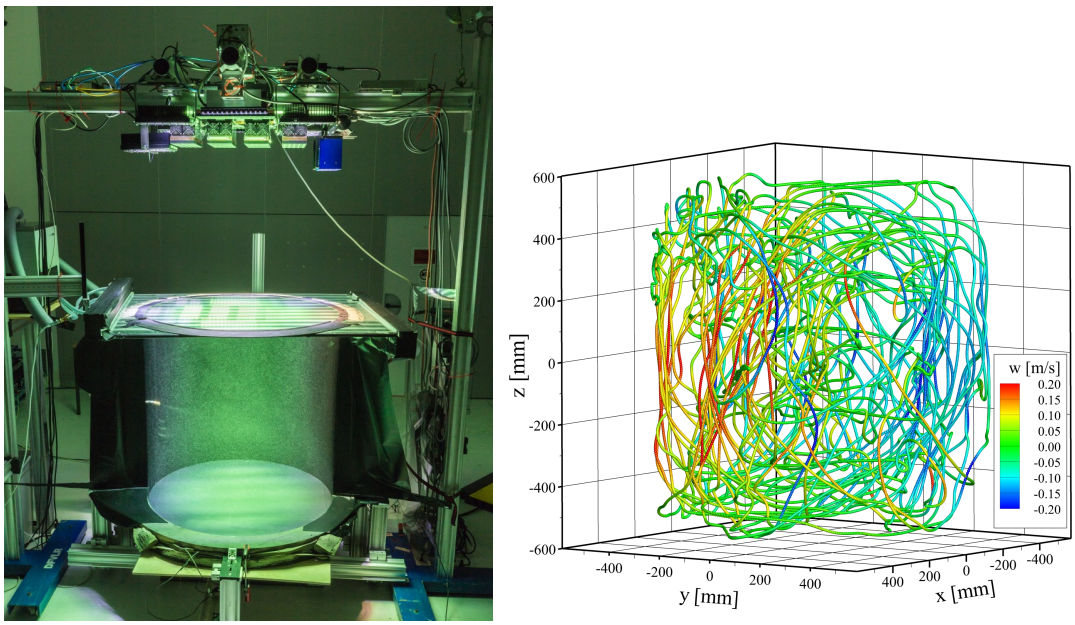

Figure 2.4: Left: Experimental setup of the Rayleigh-Bénard convection during the experiment. The cylinder is filled with air and helium filled soap bubbles and illuminated from the top. Right: Long trajectory capturing over 1000 free fall times colour coded by vertical velocity. It is possible to see the convection cell with up-welling fluid (red) in one half and down-welling fluid (blue) in the other half. Figure courtesy of J. Bosbach (Bosbach et al., 2021).

particles for this experiment were specially designed helium-filled soap bubbles. By modifying the bubble film solution, the average life expectancy was increased to 326 s compared to the commercially available solution with an average lifetime of 97 s (Huhn et al., 2017). This resulted in very long trajectories, the histograms of the trajectory lengths are presented in figure 2.1 c) for RBC I and d) for RBC II. A single example trajectory is presented in the right panel of figure 2.4, capturing over 1000 free fall times. The average diameter of the particles was 370 μm and with a Stokes number of $\approx 8 \cdot 10^{-4}$, this allowed particles to follow turbulent fluctuations and to act as passive tracers. The flow was illuminated by 849 pulsed high-power LEDs which were located above the transparent top plate. The LEDs were synchronised with a camera system, consisting of six scientific CMOS cameras, recording the illuminated particles (fig. 2.4 (a)). The two datasets provided have different Rayleigh numbers, the first one has $Ra = 5.25 \cdot 10^8$ with a Taylor Reynolds number of 147 (referred to as RBC I) and the second one has $Ra = 1.53 \cdot 10^9$ and $Re_\lambda = 186$ (RBC II). The cameras operated at 20 Hz for RBC I and 30 Hz for RBC II. Within this thesis, the focus is on the bulk. Therefore, we conditioned the statistics on wall distance in both vertical and

horizontal directions resulting in the measurement domains V_m reported in table 2.1. With a Prandtl number of 0.7, the thermal boundary layer λ_b (eq. (1.51)) should be thicker than the velocity boundary layer. However, for the RBC II case, it was estimated that after 2 λ_b the average velocity is 92% of the maximal velocity. To disregard any effects of the walls, data points at distances of 25.5 $mm = 3\ \lambda_b$ were discarded. For simplicity, the same distances were used for the RBC I case, resulting in distances of less than 2.2 λ_b from the wall being discarded. Additional relevant parameters can be found in table 2.1, and more details about the experiments and additional flow visualisations can be found in Bosbach et al. (2021); Godbersen et al. (2021).

2.1.4 Turbulent Boundary Layer

The experiment for the turbulent boundary layer dataset was part of the joint experimental campaign of the DLR Göttingen and the Universität der Bundeswehr (University of German Armed Forces) Munich and was conducted at the atmospheric wind tunnel in Munich (Schanz et al., 2019). The free stream velocity of the analysed dataset is 7 m/s and the part analysed is where zero-pressure-gradient (ZPG) conditions were present. This was achieved through a specific setup in the test section (fig. 2.5). The test section was in total 22 m long with a cross section of 1.8 $\times$ 1.8 m^2 and the model (fig. 2.5 b)) was installed a few meters downstream in the test section (fig. 2.5 c)). Over the first 4 m the flow followed a flat plate where a ZPG boundary layer formed. After this two curvilinear flow deflections were installed through a 1.17 m long plate angled at 18° followed by a flat plate. That generated a small favourable-pressure-gradient region, followed by an adverse-pressure-gradient region.

To record the flow a camera system of 12 high speed cameras was installed, operating at 1000 Hz. This allowed to capture a volume of approximately 2800 $\times$ 800 $\times$ 250 mm^3 in streamwise $\times$ spanwise $\times$ wall-normal direction including the full ZPG region with a length of 1800 mm. Ten high power LED arrays, operating at 2000 Hz, were installed above the wind tunnel to illuminate the flow, setting the wall-normal extent that was recorded to 250 mm (fig. 2.5 c)). The flow was seeded with helium filled soap bubbles (HFSB) with a response time of 30 μs (Scarano et al., 2015), resulting in a Stokes number of 0.01 based on the free-stream velocity and displacement thickness of the flow. Therefore, no inertial effects of the particles on the flow are expected and the HFSB were approximated as passive tracers

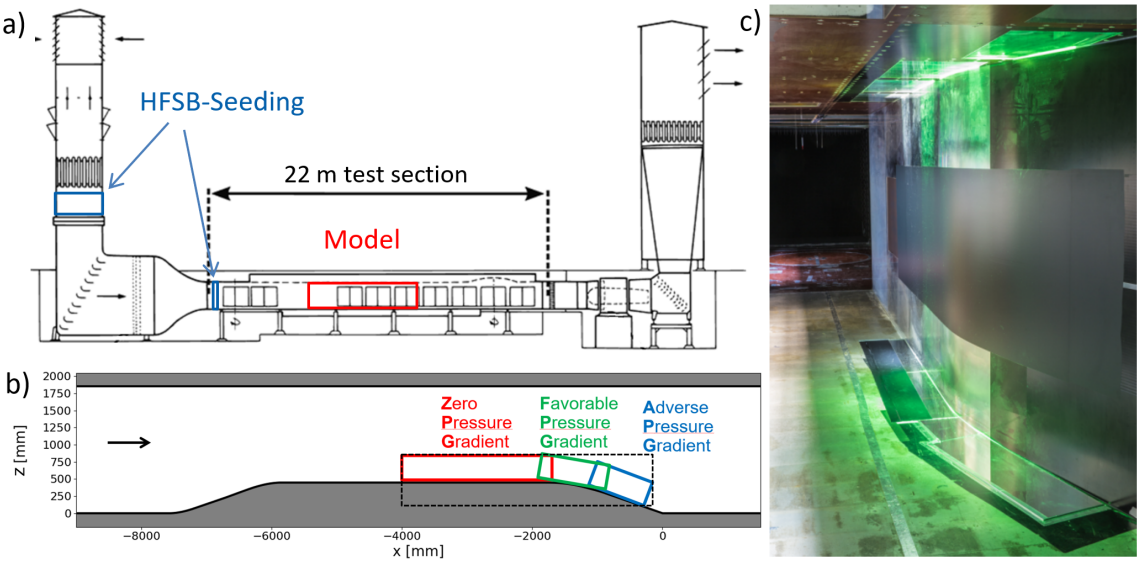

Figure 2.5: a) Sketch of the experimental setup of the wind tunnel with an approximate location of the model. The setup allows to seed the flow at two different points, for the analysed dataset the flow was seeded with HFSB as tracers directly in front of the test section. b) Detailed profile of wall-normal direction of the model in the test section with indicated pressure gradients. c) The wind tunnel during an experiment, with particles illuminated by LEDs. All figures from Schanz et al. (2019).

for the analysis. This setup was able to track up to 600,000 bubbles instantaneously. For each run, 1382 images were processed by STB to generate trajectories. A visualisation of a subset of the particles can be found in the top panel of figure 2.6 where the colour indicates the streamwise velocity, which increases with the distance to the wall and the distribution of trajectory lengths is presented in figure 2.1 b). In the logarithmic layer, the velocity profile follows the logarithmic law (eq. (1.59), fig. 2.6, middle). For the analysis only a sub-volume of the logarithmic layer was used, as it is not possible to define global Kolmogorov scales in a boundary layer. In the bottom panel of figure 2.6, the local Kolmogorov length scale as a function of wall distance is shown, calculated based on methods presented in Falkovich et al. (2012). This allows us to compare the different flow types based on the underlying physics and remove Reynolds number effects. To balance convergence of the data analysis and the assumption of constant Kolmogorov scales, the volume used for the analysis was restricted to $z^+ = 153 - 287$. In this sub-volume the Kolmogorov length scale varies η between 174.24 μm and 186.14 μm and the time scale τ_η between 2.02 ms and 2.56 ms, resulting in a Taylor Reynolds number of 108.

Further analysis of Eulerian and Lagrangian statistics obtained from the same dataset

can be found in Bross et al. (2023).

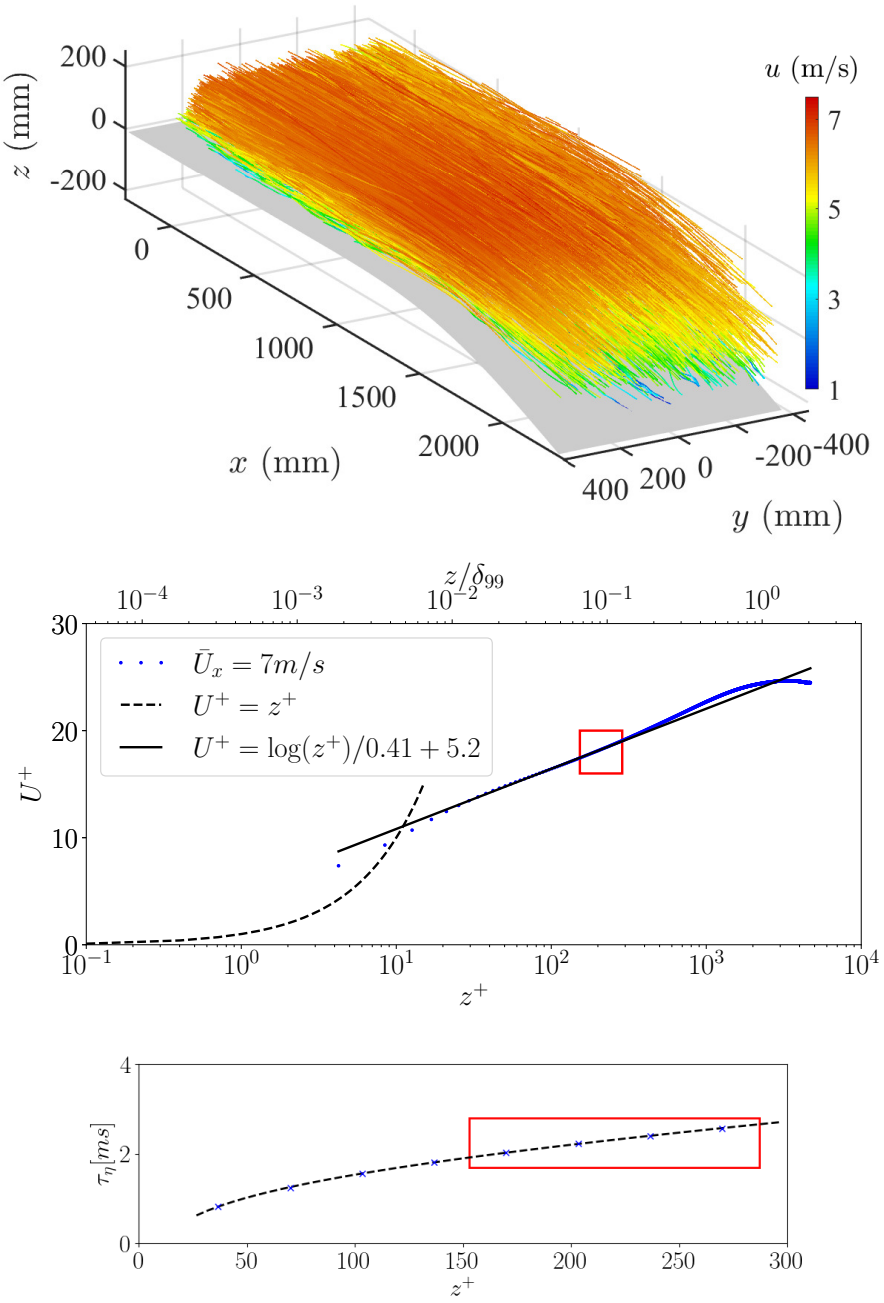

Figure 2.6: Top: Visualisation of a subset of trajectories coloured by the streamwise velocity. It can be seen that the velocity changes with the distance to the wall. Figure courtesy of M. Bross. Middle: Velocity profile as a function of the wall distance. For $z^+ \approx 30 - 400$, the velocity profile follows the log-law. Bottom: Kolmogorov time scale as a function of the wall distance measured at different heights. The red box in the middle and bottom figure indicates the part of the log-layer used for the analysis.

2.2 Numerical Data

This section focuses on the details of direct numerical simulations that generated the datasets of magnetohydrodynamic (MHD) turbulence provided by Damiano Capocci (Capocci et al., 2024; Capocci, 2024). The governing equations of MHD are given by equations (1.60)-(1.63). As a numerical concept hyperdiffusivity was introduced, resulting in (Borue and Orszag, 1995):

$$\frac{\partial \boldsymbol{u}}{\partial t} + \boldsymbol{u}\cdot\nabla\boldsymbol{u} = -\nabla p + \boldsymbol{B}\cdot\nabla\boldsymbol{B} + \nu_\alpha(-1)^{\alpha+1}\nabla^{2\alpha}\boldsymbol{u} + \boldsymbol{F} \tag{2.1}$$

$$\frac{\partial \boldsymbol{B}}{\partial t} + \boldsymbol{u}\cdot\nabla\boldsymbol{B} = \boldsymbol{B}\cdot\nabla\boldsymbol{u} + \mu_\alpha(-1)^{\alpha+1}\nabla^{2\alpha}\boldsymbol{B} \tag{2.2}$$

$$\nabla\cdot\boldsymbol{u} = 0 \tag{2.3}$$

$$\nabla\cdot\boldsymbol{B} = 0 \tag{2.4}$$

where $\boldsymbol{u}$ is the velocity field and $\boldsymbol{B}$ the magnetic field in Alfvén units. To extend the inertial range, the standard diffusion operators have been replaced by powers $\alpha \geq 1$ where ν_α is the kinematic hyperviscosity and μ_α the magnetic hyperdiffusivity. For $\alpha = 1$ these equations are the governing equations for MHD with standard viscosity. The concept of hyperdiffusivity also allows to define hyperdiffusive Kolmogorov length scales (Borue and Orszag, 1995):

$$\eta_\alpha^u = (\nu_\alpha^3/\varepsilon_u)^{\frac{1}{6\alpha-2}} \tag{2.5}$$

$$\eta_\alpha^b = (\mu_\alpha^3/\varepsilon_b)^{\frac{1}{6\alpha-2}}\,. \tag{2.6}$$

and also a Reynolds number based on the integral scale Reynolds number (Capocci et al., 2024):

$$Re = C\left(\frac{L_u}{l_d}\right)^{4/3} \tag{2.7}$$

where L_u is the integral scale and $l_d = \pi/\mathrm{argmax}(k^2 E_u(k))$ the effective dissipation range scale. C is a constant that is estimated by fitting the integral scale Reynolds number of standard diffusive data to the modified Reynolds number in equation (2.7). This is based on a method suggested by Spyksma et al. (2012). Equations (2.1) - (2.4) were solved using fully dealiased Fourier pseudospectral methods in a triply periodic $(2\pi)^3$ domain (Patterson Jr and Orszag, 1971; Canuto et al., 1988) with two-thirds dealiasing (Orszag, 1971), resulting in

	A1	A2	A3	A4	B10
B_0	0	0	0	0	10
$B_0/b_{z_{rms}}$	0	0	0	0	12.7
N	1024	2048	1024	2048	1024
α	1	1	5	5	10
E_u	0.75	0.73	0.70	0.66	3.52
E_b	0.33	0.38	0.48	0.54	0.31
ν_α	4.2×10^{-4}	2.0×10^{-4}	5×10^{-23}	5×10^{-26}	5×10^{-23}
ε_u	0.22	0.22	0.31	0.33	0.32
ε_b	0.53	0.52	0.43	0.43	0.40
L_u	0.55	0.55	0.53	0.51	1.56
τ	0.77	0.79	0.78	0.81	1.08
Re	936	2144	4272	9931	7501
$k_{\max}$	341	682	341	682	341
$k_{\max}/k_{\mathrm{diss},u}$	1.46	1.68	1.45	1.38	1.45
$k_{\max}/k_{\mathrm{diss},b}$	1.17	1.35	1.43	1.37	1.44
$\Delta t/\tau$	1.3	1.1	1.5	1.1	0.8
#	11	18	40	18	20

Table 2.2: Parameters and key observables of the numerical datasets. The magnetic background field is B_0, $b_{z_{rms}}$ is the root-mean-squared of the magnetic field fluctuations in z-direction, parallel to the magnetic field, and the number of grid points per coordinate is N. The exponent of the Laplacian is α, and E_u and E_b are the mean total kinetic and magnetic energy, respectively. The kinematic hyperviscosity is ν_α and using that the magnetic Prandtl number Pm is of unity, this also gives the magnetic diffusivity μ_α where $Pm = \nu_\alpha/\mu_\alpha = 1$. The kinetic and magnetic energy dissipation rates are given by ε_u and ε_b, the longitudinal integral scale is $L_u = 3\pi/(4E_u)\int_0^{k_{\max}} \mathrm{d}k E_u(k)/k$ and $\tau = L_u/\sqrt{2E_u/3}$ is the large-scale eddy-turnover time. The integral Reynolds number is Re, calculated using equation (2.7). The ratio $k_{\max}/k_{\mathrm{diss},u/b}$ is the ratio of the largest resolved wavenumber component after dealiasing $k_{\max}$ and the dissipative wavenumbers based on the hyperdiffusive Kolmogorov scales defined in equations (2.5)-(2.6). In total # snapshots were used to calculate the statistics and were sampled with a mean period of Δt. The dataset B10 is not statistically stationary, therefore the parameters L_u, τ and Re were calculated in the interval $t/\tau \in [95, 98]$ only, see figure 2.7.

$k_{max} \approx 1/3N$. To achieve a time advancement, a second-order Runge-Kutta scheme was implemented. The spatial resolution was chosen such that $\eta_\alpha^u/\Delta x \gtrsim 1.3$ and $\eta_\alpha^b/\Delta x \gtrsim 1.3$ (Donzis et al., 2008; Wan et al., 2010) where $\Delta x = 2\pi/N$ and N is the number of grid points per coordinate, the simulations ran in total on N^3 grid points. For the forcing $\boldsymbol{F}$ a Ornstein-Uhlenbeck process, active in the wavenumber band $k \in [2.5, 5]$, was used.

In total, five numerical datasets were analysed. The details of the numerical simulations and key properties are summarised in table 2.2. Standard diffusivity, where $\alpha = 1$, was used for datasets A1 and A2, while for the remaining datasets hyperdiffusivity with $\alpha = 5$ was

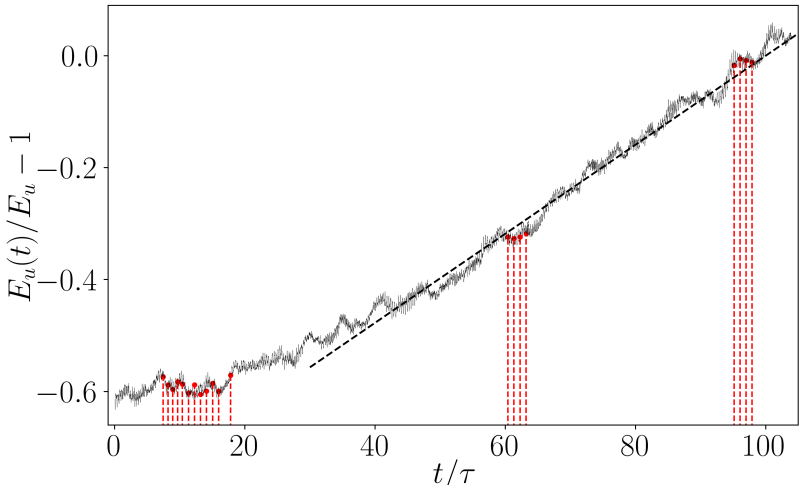

Figure 2.7: Time series of the kinetic energy for the dataset B10 with a magnetic background field $B_0 = 10$, normalised using the mean E_u of $E_u(t)$. To estimate L_u, τ and Re the samples in $t/\tau \in [95, 98]$ were used, for the analysis in chapter 5, the samples in $t/\tau \in [5, 20]$ where $B0/b_{z_{rms}} = 12.7$. The red lines indicate the samples for this datasets and the dashed line shows the linear growth of the kinetic energy. Figure courtesy of D. Capocci.

used. For all datasets, we used $\nu_\alpha = \mu_\alpha$, such that $Pm = 1$. The B10 dataset has a magnetic background field $B_0 = 10$ in z-direction. The datasets analysed only include the fluctuations of magnetic and velocity fields, where $\langle u_i \rangle = \langle b_i \rangle = 0$ for $i \in \{x, y, z\}$. For the datasets with no magnetic background field $B_0 = 0$, a number of snapshots were selected after reaching statistical stationarity with the large-scale turnover time as sampling period. For the dataset with non-zero magnetic background field, the kinetic energy is increasing (fig. 2.7) and the snapshots are sampled randomly within regions where the kinetic energy was approximately constant (see the red lines in fig. 2.7). For the estimation of L_u, τ and Re provided in table 2.2 the samples in $t/\tau \in [95, 98]$ were used. For the analysis in chapter 5, the samples in $t/\tau \in [5, 20]$ where $B_0/b_{z_{rms}} = 12.7$ were used.

The kinetic and magnetic energy spectra of the different datasets can be found in figure 2.8. For subfigures (a) and (b) the differences between standard diffusivity (dashed lines) and hyperdiffusivity (solid lines) become clear where, for the magnetic and kinetic spectra, hyperdiffusivity leads to more energy in smaller scales before a sharp drop off at the dissipating scales. For the large scales, hyperdiffusivity does not have a strong impact, also known as the bottleneck effect (Haugen and Brandenburg, 2004; Frisch et al., 2008). For the four datasets the kinetic energy spectra have a peak around the forced scales while the magnetic

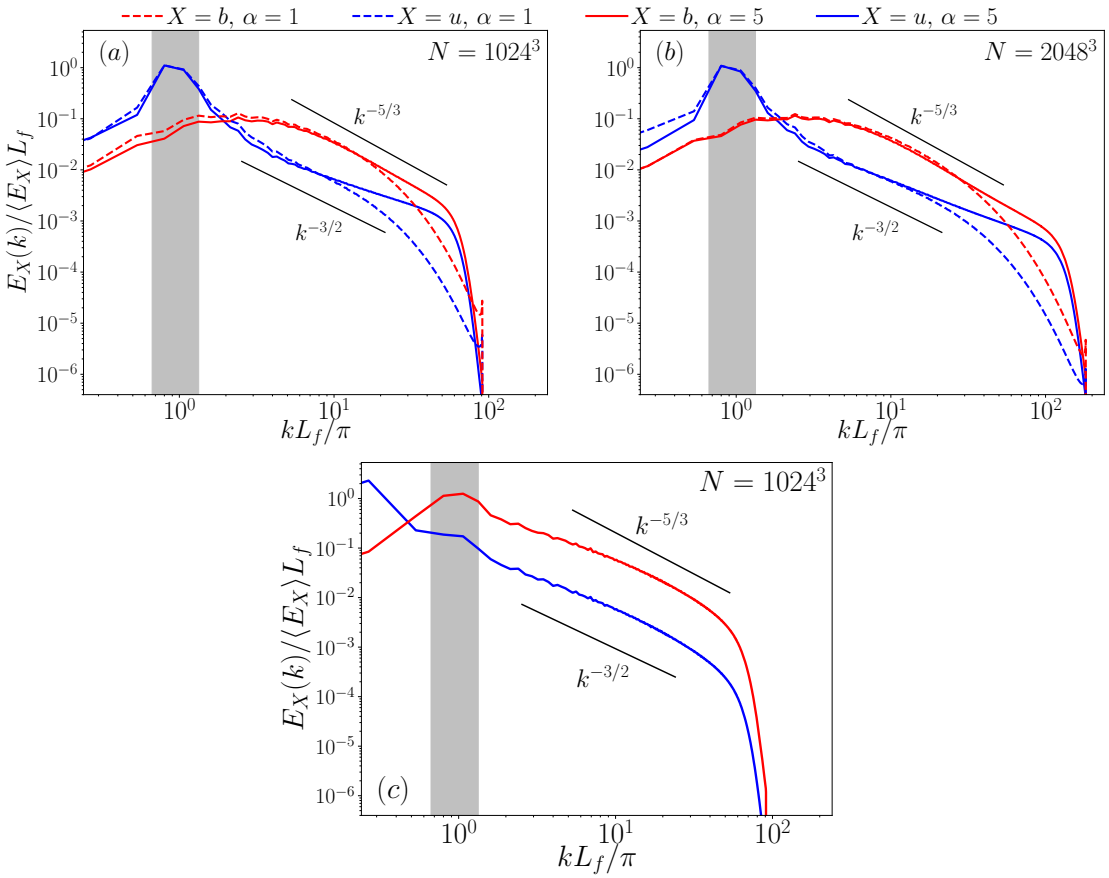

Figure 2.8: Time-averaged energy spectra of velocity $E_u(k)$ and magnetic $E_b(k)$ fields: comparison between (a) datasets A1 and A3, (b) datasets A2 and A4 while (c) is referring to dataset B10. The grey region indicates the wavenumber band $k \in [2.5, 5.0]$ where the velocity field is forced. Figure courtesy of D. Capocci.

energy spectra are more flat as the magnetic field is not forced directly and maintained by the velocity field only. For scales between the forcing scales and dissipative scales, a $k^{-3/2}$- and a $k^{-5/3}$-reference line are provided. The exact power laws in the inertial range are unclear across all datasets but for the kinetic energy, the spectrum is approximately following a $k^{-3/2}$-law which extends to smaller scales for hyperdiffusivity. For standard viscosity the magnetic energy spectrum does not follow a clear power law between the two scales. The spectral scaling of the magnetic energy is closer to $k^{-5/3}$ when using hyperdiffusivity. Due to the effect of unit magnetic Prandtl number, the dissipating wavenumbers of the kinetic and magnetic energy spectra are similar.

By introducing a magnetic background field, the spectrum (fig. 2.8 (c)) differs significantly from the previous discussed spectra. The kinetic energy spectrum does not have its peak at the forcing scales and is shifted to larger scales, indicating an inverse energy transfer,

most likely a result of a partial two dimensionalisation of the flow as expected in the presence of a strong background field (Alexakis, 2011; Gallet and Doering, 2015). For the magnetic spectrum, we can see that energy can now get transferred directly between the magnetic and kinetic energy, resulting in a peak in the magnetic energy spectrum at the forcing scales. This direct transfer is mediated by the spatially and temporally constant background field.

In figure 2.9, the comparison between the energy fluxes is shown, where subfigures (a) and (b) compare the effect of hyperdiffusivity and standard diffusivity at two different resolutions (1024 for subfigure (a) and 2048 for subfigure (b)). Specifically, for each dataset the total energy flux and the corresponding kinetic and magnetic subfluxes are shown (eqs. (1.67)-(1.69)). In subfigures (a) and (b), the hyperdiffusive datasets are characterised by more extended plateaux compared to the standard diffusive datasets and by the presence of an approximate *equipartition range* between kinetic and magnetic subfluxes. The approximation works better for the higher-resolved dataset A4.

In figure 2.9 (c), we show the fluxes of the dataset B10. The two main differences with respect to figures 2.9 (a) and (b) are that the subfluxes tend to be *scale independent* and that they do not reach the equipartition in the small scales.

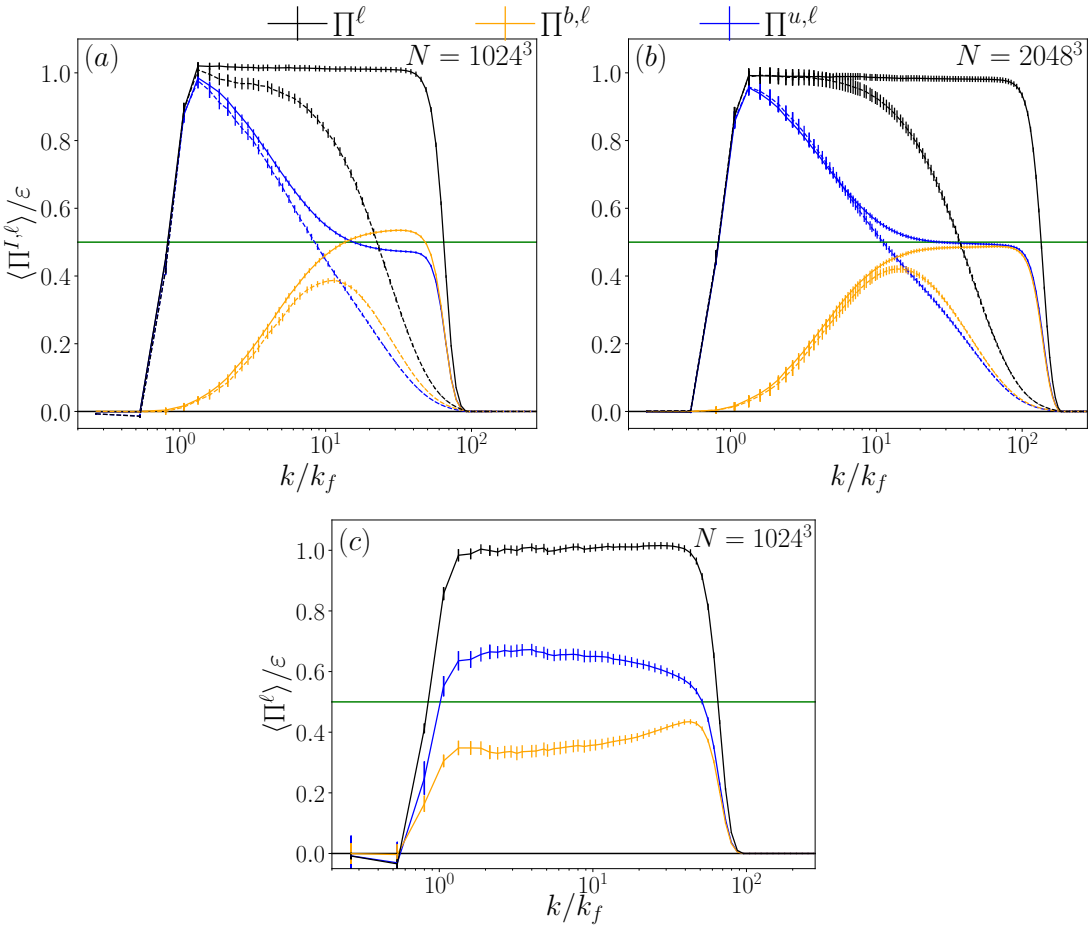

Figure 2.9: Scale filtered total (black), kinetic (blue) and magnetic (yellow) energy fluxes. Comparison between (a) datasets A1 and A3, (b) A2 and A4 where dashed lines refer to standard diffusive datasets (A1, A2). Panel (c) refers to B10. A green reference line at $\langle \Pi^{\ell} \rangle / \varepsilon = 0.5$ is shown. The error bars indicate one standard error. Figure courtesy of D. Capocci.

Chapter 3

Methods and Implementation

For this thesis, I calculated statistics of two types of datasets, that is, tracer particle tracks obtained in laboratory experiments and data obtained by numerical simulation. For the two types of data different numerical methods are used which will be outlined in what follows.

3.1 Numerical Methods for Experimental Data

For the analysis of the provided data we developed a trajectory analyser called TARA which can calculate different statistical properties of Lagrangian trajectories. The raw data was provided in multiple *.npy*-files per dataset, each containing the 3D position and time of many Lagrangian particle trajectories generated by the Shake-the-Box algorithm. TARA underwent three main development stages:

1. Initial version provided by Julian Weigel (Weigel et al., 2020) (object orientated)

2. Extension for curvature and torsion statistics and change to a functional approach

3. Implementation of *trackfit* (Schanz et al., 2016) for the calculation of derivatives

A requirement of all versions was that the trajectories needed to be longer than 100 time steps. That is to ensure convergence of the B-Splines fitted to the particle positions. In figure 2.1 the histograms of the trajectory lengths of the different datasets are shown, where it can be seen that by conditioning on trajectories longer than 100 time steps only a small portion of the data is neglected.

I will now give an overview of the different stages and conclude with a brief summary about the current implementation of the code.

3.1.1 Initial Version

The initial provided version included the calculation of velocity, acceleration, curvature and torsion statistics as well as conditioned statistics for the acceleration and the calculation of autocorrelation functions. This version used an object orientated approach and included several steps. In the first step, the raw data of the trajectories was fitted and third order time derivatives were calculated using B-Splines, allowing to calculate curvature and torsion. For each trajectory the position, velocity, acceleration, curvature and torsion were saved in a separate *.csv*-file . Here, a filtering operation was incorporated that allowed to select trajectory parts conditioned on the location of the particle. The histograms were calculated for each trajectory separately using user-defined boundaries and were added up to global histograms in the final step. To calculate autocorrelation functions, the pre-processed files of the trajectories containing acceleration were used. The different functions outlined here will be explained in more detail in the next section.

This version was partially parallelised, resulting in a significant speed up in calculation time. However, the imposed trajectory specific output created a huge memory demand which was not justifiable. Therefore, a redesign and restructuring of TARA was necessary.

3.1.2 Upgraded Version

During the redesign of TARA, I implemented the full parallelisation of the algorithm, improving the memory usage, and a change to a more functional approach. Additionally, I added functions to calculate conditional statistics for curvature and torsion. Here, I will give a detailed overview of all steps in the code.

Calculation of Velocity, Acceleration and Time Derivative of Acceleration

B-Splines are fitted to the particle positions to obtain smooth trajectories. By taking derivatives of these trajectories, the velocity, acceleration and time derivative of the acceleration can be calculated. B-Splines are smooth curves constructed by combining piecewise polyno-

mial functions $B_{i,k;t}(x)$ of order k to fit a set of data points (de Boor, 1978). Each basis function $B_{i,k;t}(x)$ is defined only over a small range with smooth transitions between different basis functions. These transition points are called knots t. These knots are calculated by an optimisation algorithm that captures the rapid changes of the curve, such that the complexity of the data is preserved. The fitted curve $S(x)$ is calculated by:

$$S(x) = \sum_{i=0}^{n-1} c_i B_{i,k;t}(x) \tag{3.1}$$

where c_i are the B-Spline coefficients, determined through the control points. Control points are influencing the shape of the fitted curve and are chosen to minimise the difference between the curve and the data points.

Here, we used B-Splines of order 5, ensuring that derivatives up to order 3 are continuous and each direction was fitted separately. By introducing a smoothness parameter s, a spatial uncertainty can be introduced. The relation between the spatial uncertainty ℓ and the smoothness parameter s will be shown next, together with the estimation of the smoothness parameter using the zero-crossing of the autocorrelation function of the acceleration.

Autocorrelation Function and Estimation of Smoothness Parameter

Correlation functions are an additional way to characterise the datasets as discussed in section 1.2. For the autocorrelation function of the acceleration a zero-crossing at $\approx 2\tau_\eta$ can be expected for all datasets considered here (Mordant, Crawford and Bodenschatz, 2004; Yeung and Pope, 1989; Ni et al., 2012; Stelzenmuller et al., 2017) which will be used to estimate the smoothness parameter s. The autocorrelation function of the i^{th} acceleration component a_i is defined as a function of the time lag τ:

$$R_i(\tau) = \langle a_i(t)\ a_i(t+\tau) \rangle \tag{3.2}$$

where no summation over indices is implied. In TARA, a simpler version of this equation is implemented as large amounts of data are available to ensure convergence and to decrease the computational cost. That is, only trajectories that lie fully in the measurement volume and are longer than a maximal time lag τ_{max} are considered. For these trajectories, the

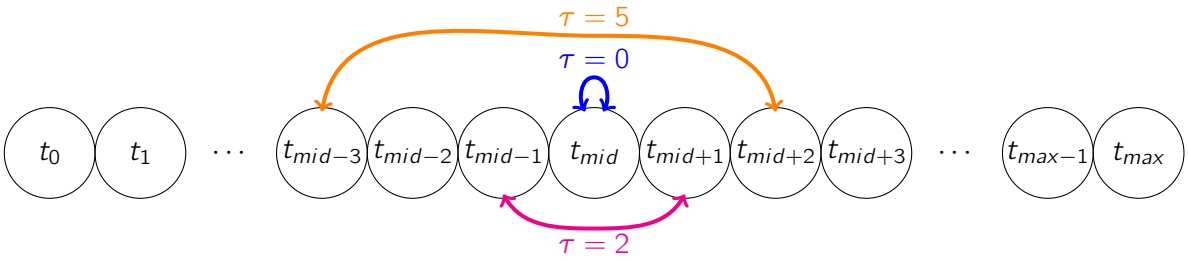

Figure 3.1: Sketch of the calculation of autocorrelation coefficients. Each point represents a time step, where $t_i = i$. The mid point is defined as the rounded-down integer of $t_{max}/2$.

correlation coefficients are calculated:

$$C_i(\tau) = \begin{cases} a_i(t_{mid} - \tau/2)\ a_i(t_{mid} + \tau/2) & \text{if } \tau/2 \in \mathbb{N} \\ a_i(t_{mid} - \tau/2 - 0.5)\ a_i(t_{mid} + \tau/2 - 0.5) & \text{if } \tau/2 \notin \mathbb{N} \end{cases} \tag{3.3}$$

where t_{mid} is the time step half of the total trajectory length. A sketch on the calculation of the correlation coefficients is presented figure 3.1. The correlation coefficients for each $\tau = 0, \ldots, \tau_{max}$ are averaged over the whole ensemble of trajectories to get the autocorrelation function.

In figure 3.2, the acceleration autocorrelation functions in y-directions for different smoothing parameters are shown (left column) as well as the autocorrelation functions in all directions for the chosen smoothness parameter (right column) which are 0.02, 0.3,0.22 and 0.3 for von Kármán flow, RBC I, RBC II and the boundary layer respectively. In the following, we will see that this can be connected to the spatial uncertainty ℓ from table 2.1. The values were chosen such that the autocorrelation functions are smooth, that the shape for small times can be estimated by a parabola, and that the zero crossing is $\approx 2\tau_\eta$ for von Kármán flow, RBC I and RBC II. The zero crossing for the boundary layer was not considered as the Kolmogorov units were only provided with the implementation of *trackfit*. In the bottom row of figure 3.2, the Kolmogorov time scale of the sub-volume (fig. 2.6) was used to normalise the time scale while the autocorrelation function was calculated using data from the whole logarithmic layer.

The smoothness parameter s can be connected to a spatial uncertainty ℓ (Dierckx, 1982). For a set of data points $\{(x_i, y_i)\}$, in the case of trajectories, this would be $\{(t_i, x_i)\}$, we used B-Splines to find the function $S(x) = y$. Here, y_i is a measured data point with a spatial

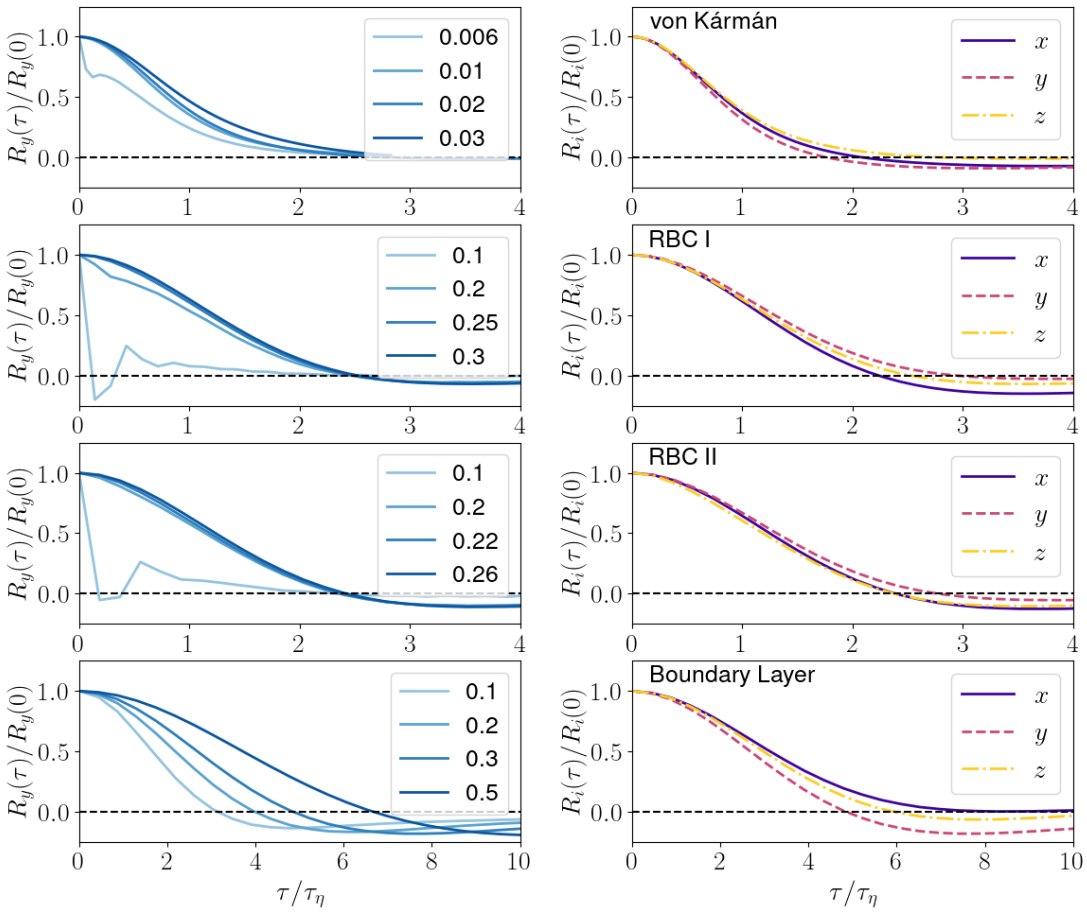

Figure 3.2: Acceleration autocorrelation functions for the different datasets for different values of the smoothness parameter (left column, increasing from light to dark blue) and for the different directions (right column, x in dark blue, y in purple and z in yellow) for the chosen smoothness parameter. It should be noted that for the boundary layer the Kolmogorov time scale estimated in the sub-volume was used while for the calculation of the autocorrelation function the whole log-layer ($z^+ = 40 - 500$) was used.

uncertainty ℓ and the real position $y_{\text{true}}(x)$ is given by:

$$y_{\text{true}}(x) = y(x) \pm \ell\,. \tag{3.4}$$

To account for the spatial uncertainty, we allow:

$$\sum_i (w_i(S_i - y_i))^2 \leq s \tag{3.5}$$

where $w_i = 1/\ell$, resulting in

$$\sum_i (S_i - y_i)^2 \leq s\ell^2 := s'\,. \tag{3.6}$$

The implemented version of the B-Splines used the python function *splrep* (SciPy Developers, 2024) where it is suggested that:

$$m - \sqrt{2m} \leq s \leq m + \sqrt{2m}. \tag{3.7}$$

where m is the number of data points. We therefore chose s such that $s = m$, thus:

$$s' = m\ell^2\,. \tag{3.8}$$

This connects the smoothing of the trajectory with the spatial uncertainty and the trajectory length. The smoothing s' allows the fitted curve to deviate from the original data points.

Calculation of Moments

As part of the analysis, the first four statistical moments are calculated (eqs. (1.10)-(1.13)). For this, all data points of a trajectory that lie in the measurement volume are considered. This is different to the requirement for the autocorrelation function where the full trajectory has to lie in the measurement volume as the calculation of the moments does not include a time lag. The moments are calculated using the discrete versions of equations (1.10)-(1.13) as shown in equation (1.16) for the mean.

Calculation of PDFs

For the calculation of PDFs and joint PDFs, in-build functions from python are used to first calculate histograms $H(x)$. The normalisation to PDFs is handled in the post processing such that:

$$1/A \int dx H(x) = \int dx P(x) = 1 \tag{3.9}$$

with A the normalisation factor $A = \int dx H(x)$ and $P(x)$ the PDF of the variable x. For joint PDFs $P(x, y)$ this becomes:

$$\int dx \int dy P(x, y) = 1\,. \tag{3.10}$$

For the curvature and torsion, logarithmic bins are used. When using logarithmic bins, special care needs to be taken, as the calculated PDF is $P^*(log(x))$ while the PDF of interest is $P(x)$. Using that $g(x) = e^x$, the PDF $P(x)$ can be calculated as (Siegrist, 2022):

$$P(x) = P^*(g^{-1}(x))|\frac{d}{dy} g^{-1}(x)| \tag{3.11}$$

$$= P^*(\log x)\frac{1}{|x|}\,. \tag{3.12}$$

Conditional Statistics

For the calculation of the moments and histograms, an additional function is implemented to calculate statistics conditioned on the coarse-grained acceleration. For each sub-ensemble a sub-ensemble is created from which the statistics are calculated using the functions as outlined above. For a given array of values of the coarse-grained acceleration $\{\alpha_1, \alpha_2, \ldots, \alpha_n\}$, points are assigned to sub-ensemble i where $i = 1, \ldots, n$ if $\alpha \in [\alpha_i - 0.05\alpha_i, \alpha_i + 0.05\alpha_i]$.

Code Architecture

The updated code was fully parallelised to speed up the computation time, such that each core calculated statistics of a different *.npy*-file. Additionally, there was a requirement to store less data. To overcome this issue, the different properties of a trajectory are not saved any more and are calculated each time when calculating the statistics. This generally increases computing time but the advantage of saving memory outweighs the additional computing

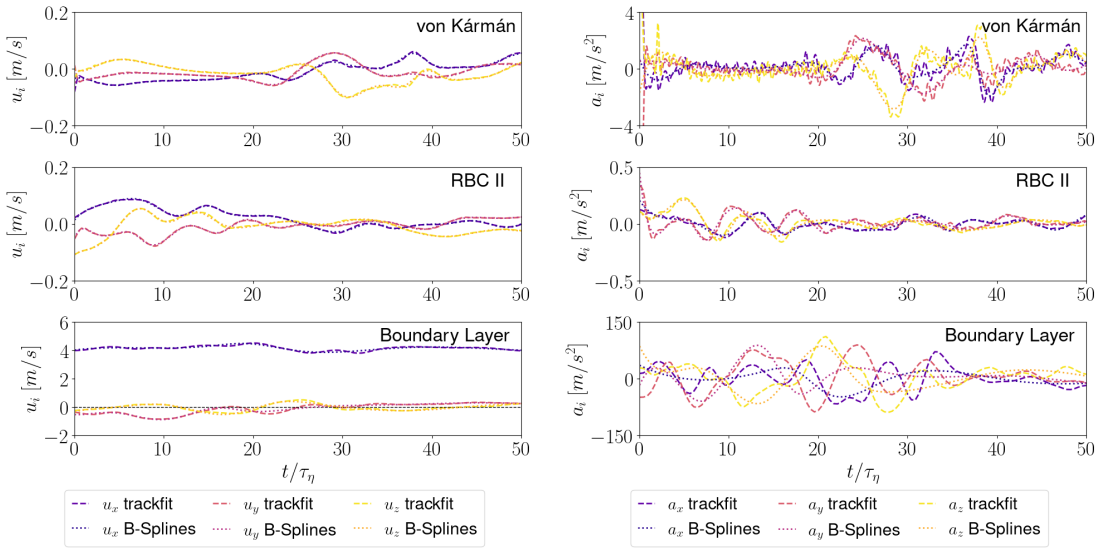

Figure 3.3: Velocity and acceleration component time series of an example trajectory of the three flow types, calculating using the B-Splines (dotted) method and *trackfit* (dashed) with x in blue, y in pink and z in yellow.

time.

3.1.3 Trackfit

In the last upgrade, I implemented the use of the provided the DLR algorithm *trackfit* (Schanz et al., 2016) for the calculation of the derivatives up to order three. It is a highly optimised algorithm, specifically developed for the provided Lagrangian data providing more accurate results. The raw particle positions are fitted using B-Splines of order three in combination with noise reduction where the third derivative of the time is assumed to be white noise. This is also used to estimate the experimental error and smoothing of the trajectories (Gesemann et al., 2016). In the amplitude spectra, the crossover frequency f_c is the transition where the spectra changes from a negative slope to a constant level for higher frequencies. The positional error Δx is estimated by the height of this constant level. The crossover frequency determines the regularisation parameter λ where $\lambda = 1/(\pi f_c)^3$ which is balancing the closeness to the data and smoothness of the resulting curve. A higher crossover frequency, and therefore a smaller λ means less smoothing of the trajectories. As mentioned, the third derivative is assumed to be white noise which should be kept in mind when calculating statistics of the torsion as this involves the third time derivative.

A comparison between the two fitting methods is shown in figure 3.3 where velocity and

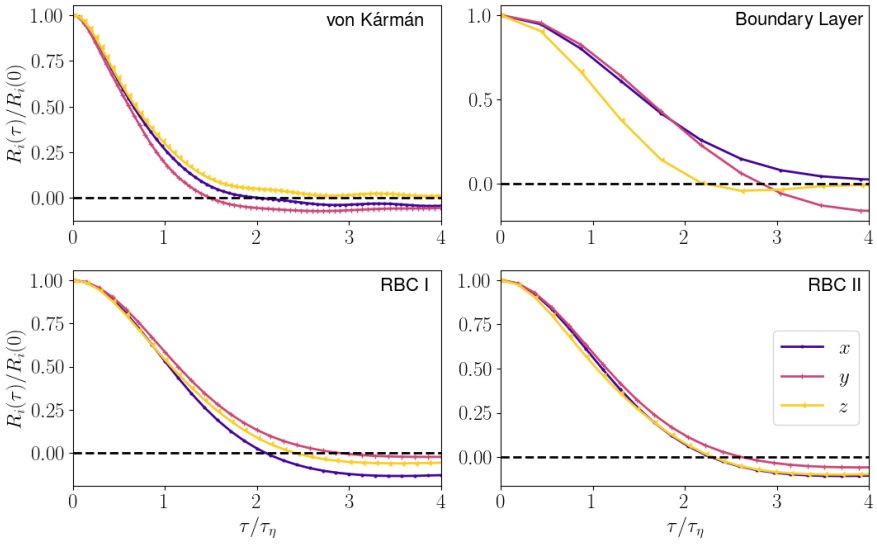

Figure 3.4: Autocorrelation functions of the acceleration components, where acceleration is calculated using *trackfit*. For all datasets, the expected zero-crossing around $2\tau_\eta$ can be found.

acceleration time series of a trajectory for the different datasets are shown. The velocity (left column) mainly fluctuates on larger scales where the differences between the two methods are small. However, on smaller scales (acceleration time series, right column), differences become more apparent. While *trackfit* has additional noise reduction, TARA was only able to reduce noise by smoothing, and therefore potentially lost information on smaller scales, which could be a potential explanation for the differences in the methods. The provided experimental uncertainty was approximately one order smaller than the estimated uncertainty based on the smoothness parameter.

Using *trackfit* allowed us to use the estimated experimental uncertainty while the autocorrelation function for the different datasets has the expected zero-crossing around $2\tau_\eta$ for all datasets, including the boundary layer which can be seen in figure 3.4.

3.2 Methods for DNS Data

The Eulerian datasets of MHD turbulence are provided in *hdf5*-files, containing magnetic or velocity vector potentials, where each field corresponds to a singe instant in time. By taking the curl of the respective fields, the magnetic field or velocity field can be calculated. Luca Biferale provided an existing *C* code that implemented a parallelised pseudospectral DNS

solver. I implemented a new module to calculate curvature statistics using provided routines for the Fourier transforms. To calculate the curvature one of the equations (1.95)-(1.81) needed to be implemented. We thoroughly tested the code and found that equation (1.95) gives reliable results. This test will be presented in the next section.

3.2.1 Calculation of PDFs and Moments

While for the experimental datasets a python in-built function was used to calculate the histograms, a function needed to be implemented for this in *C*. This also allowed the implementation of logarithmic bins for the curvature histograms where the normalisation of the histograms to a PDF is done in the post-processing as outlined in the previous section. The moments for the numerical datasets are calculated in the post-processing from the PDFs using equations (1.10)-(1.13).

3.2.2 Conditional Statistics

The conditional statistics are calculated on the value of the coarse-grained (magnetic or kinetic) dissipation. While for the experimental data, the coarse-grained acceleration was calculated when creating the sub-ensembles, the fields of the coarse-grained dissipation are calculated separately and stored. When calculating the conditioned histograms, these fields are read in to allocate the data points into the different sub-ensembles depending on the values of the coarse-grained dissipation. The statistics of the sub-ensembles are then calculated using the same methods as for the full dataset.

3.3 Testing

As part of the code development, I tested all newly implemented functions. This is either done by a comparison of the numerical results with analytic results where available or with numerical results of well established numerical methods.

3.3.1 Testing of Functions in TARA

The functions that needed testing in TARA were the calculation of the curvature and torsion and the calculation of the autocorrelation function. For both functions, we defined the error

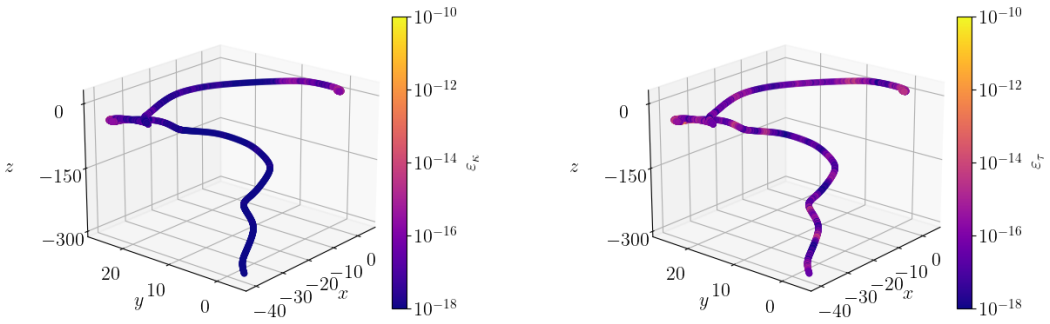

Figure 3.5: Squared difference between the curvature (left) and torsion (right) calculated using TARA and *odeint* of a trajectory in the ABC flow.

as the mean squared difference:

$$\varepsilon_x = \langle (x_{\text{analytic}} - x_{\text{numerical}})^2 \rangle \tag{3.13}$$

where x is a placeholder for the tested quantity.

Calculating the Curvature and Torsion

The two main observables in this work are curvature and torsion. To calculate these, we fit B-Splines to particle positions to calculate the derivatives. As a test flow, we used the ABC flow (Dombre et al., 1986):

$$\dot{x} = A \sin z + C \cos y$$
$$\dot{y} = B \sin x + A \cos z$$
$$\dot{z} = C \sin y + B \cos x.$$

with $A = 1.11, B = 2.09, C = 3.19$. To calculate the curvature and torsion, we used TARA to calculate all derivatives and compared that with the results when the first derivative is calculated using *odeint* (SciPy Community, 2023) and TARA for the second and third derivative. The squared differences between these two methods for a trajectory are shown in figure 3.5 and the mean square difference (eq. (3.13)) is less than 10^{-12} for the curvature and torsion.

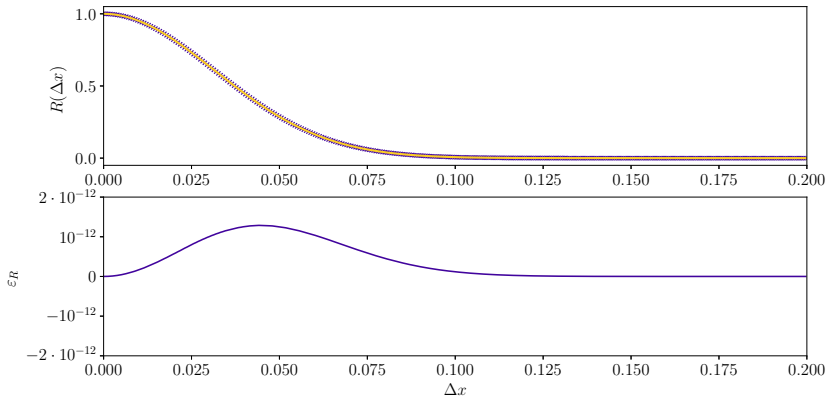

Figure 3.6: Top: Autocorrelation function of a Gaussian calculated using TARA (blue) and the analytical form (yellow). Bottom: Squared difference between numerically and analytically calculated autocorrelation function.

Autocorrelation Function

To test the implemented calculation of the autocorrelation function, we use a Gaussian signal where the autocorrelation function is also a Gaussian. For a Gaussian of the form:

$$f(x) = e^{-x^2/0.001} \tag{3.14}$$

the autocorrelation function is given by (Gubner, 2006):

$$R(\Delta x) = \int_{-\infty}^{\infty} dx f(x + \Delta x) f(x) = A e^{(-(\Delta x)^2/0.002)} \tag{3.15}$$

where A is a constant. A comparison between the analytic autocorrelation function and the autocorrelation function calculated using TARA is presented in figure 3.6 where the mean squared difference is smaller than 10^{-12}.

3.3.2 Testing of Code for Numerical Data

For the numerical data, the calculation of the curvature and the calculation of the PDFs needed to be tested. Due to the size and format of the data, we only compare the differences in the PDFs. We tested the calculation of the curvature PDFs using provided numerical data as well as a simple analytic test case where the curvature can be calculated analytically. In section 1.7.3, we derived three mathematically equivalent equations for the curvature of

stream lines and magnetic field lines. They are:

$$\kappa_u = \frac{\boldsymbol{u} \times \boldsymbol{u} \cdot \nabla \boldsymbol{u}}{|\boldsymbol{u}|^3} \tag{3.16}$$

$$= \hat{\boldsymbol{u}} \times \hat{\boldsymbol{u}} \cdot \nabla \hat{\boldsymbol{u}} \tag{3.17}$$

$$= \hat{\boldsymbol{u}} \cdot \nabla \hat{\boldsymbol{u}} \tag{3.18}$$

where $\boldsymbol{u}$ is the velocity field and $\hat{\boldsymbol{u}}$ the normalised velocity field. In figure 3.7 (a), the curvature PDFs of dataset A1 using the different curvature implementations are shown. As the three different versions lead to significant differences in the PDFs, we introduce a test vector field to find the correct implementation of the curvature

$$u = \sin(x)\cos(y) \tag{3.19}$$

$$v = -\cos(x)\sin(y) \tag{3.20}$$

$$w = 0 \tag{3.21}$$

which is divergence free, and the curvature can be calculated analytically:

$$\kappa = \frac{|\sin x \sin y(\cos^2 x + \cos^2 y)|}{(\cos^2 y \sin^2 x + \cos^2 x \sin^2 y)^{3/2}} \ . \tag{3.22}$$

Differences between Different Implementations

First, we will compare the different implementations of the curvature of the test field given by equations equations (3.16)-(3.18) with the curvature calculated analytically. The curvature histograms, where the curvature is calculated by the three different formulae that are analytically equivalent, can be found in figure 3.7 (b). When comparing the black curve, which is the histogram of the curvature calculated analytically, with the purple ((3.16)), pink ((3.17)) and yellow ((3.18)) curve representing the histograms of the three different implementations of the curvature, we can see that the core of the histogram is captured well by all implementations but differences in the tails can be noticed. For equation (3.16), we can see that the histogram of the curvature calculated by the analytic expression and the histogram of the curvature calculated numerically are identical.

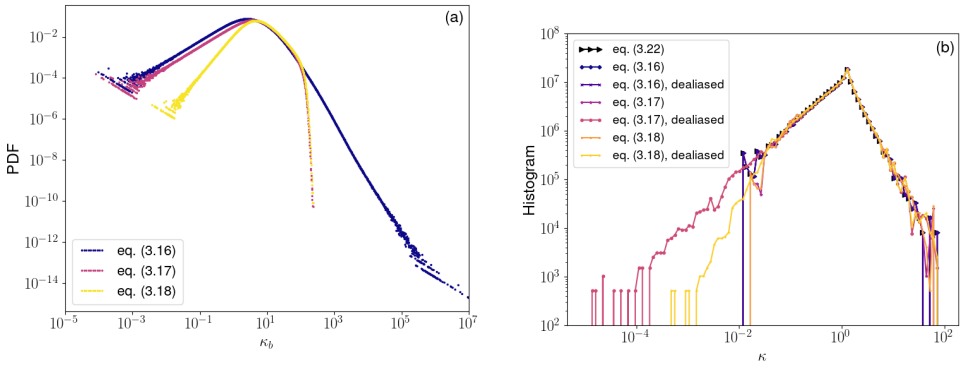

Figure 3.7: Curvature PDFs of (a) dataset A1 using the different implementations for the curvature and (b) the test field (eqs. (3.19)-(3.21)) with and without dealiasing of the non-linear term. The histograms of the curvature calculated analytically and calculated numerically using equation (3.16) are identical.

Effect of Dealiasing

Additionally, we also analysed the effect of dealiasing on the results. This is necessary as the calculation of the non-linear term in the Fourier space becomes a convolution. The test field given in equations (3.19)-(3.21), has a single wavevector $\boldsymbol{k} = (k_x, k_y) = (1, 1)$ and we calculated the curvature pseudospectrally using $N = 512$ Fourier modes in each direction. We over-resolve in such an extreme way to ensure that aliasing should not have an impact at all. For all cases, we decided to only dealias the non-linear term ($\boldsymbol{u} \cdot \nabla \boldsymbol{u}$ or $\hat{\boldsymbol{u}} \cdot \nabla \hat{\boldsymbol{u}}$) using 2/3 dealiasing. Calculating the unit vector $\hat{\boldsymbol{u}}$ introduces aliasing errors but up to our knowledge, no method is found to deal with these errors. We find that dealiasing has an impact on the cases including the normalised fields (eqs. (3.17), (3.18)) and only the implementation of equation (3.16) shows no differences between the analytic solution and implemented solution. We therefore used equation (3.16) for the analysis carried out in this work.

Chapter 4

Comparison of Lagrangian Datasets

In this chapter, I will present the results that are published in Hengster et al. (2024). The experimental data was provided by M. Bross, J. Bosbach, D. Schanz, A. Schröder, F. Huhn, M. Novara, D. Garaboa Paz, C. J. Kähler. J. Weigel provided the initial code that has been rewritten since (see sec. 3.1.2), M. Lellep helped with the code development. The analysis carried out and presented here was done by me under supervision of M. Linkmann.

This chapter gives an overview of the baseline statistics of the different experimental datasets described in section 2.1 consisting of velocity and acceleration statistics. We also present the curvature and torsion statistics, including the first measurements of the curvature PDF of Lagrangian trajectories in a boundary layer and the first reported torsion PDFs of Lagrangian trajectories of experimental data. Additionally, an analysis of the effect of anisotropy is presented, introduced either through propeller motion for the von Kármán flow, a large-scale circulation driven by a temperature gradient for RBC or a strong unidirectional flow for the boundary layer. This is done by the introduction of the curvature vector as outlined in section 1.7.1.

4.1 Velocity PDFs

For homogeneous and isotropic turbulence, Townsend (1947) and Batchelor (1953) first reported that the PDFs of velocity components are approximately Gaussian. In figure 4.1, we present the standard PDFs of all velocity components for each dataset. For the von Kármán flow, the velocity PDFs in x- and y-direction are slightly sub-Gaussian while in z-

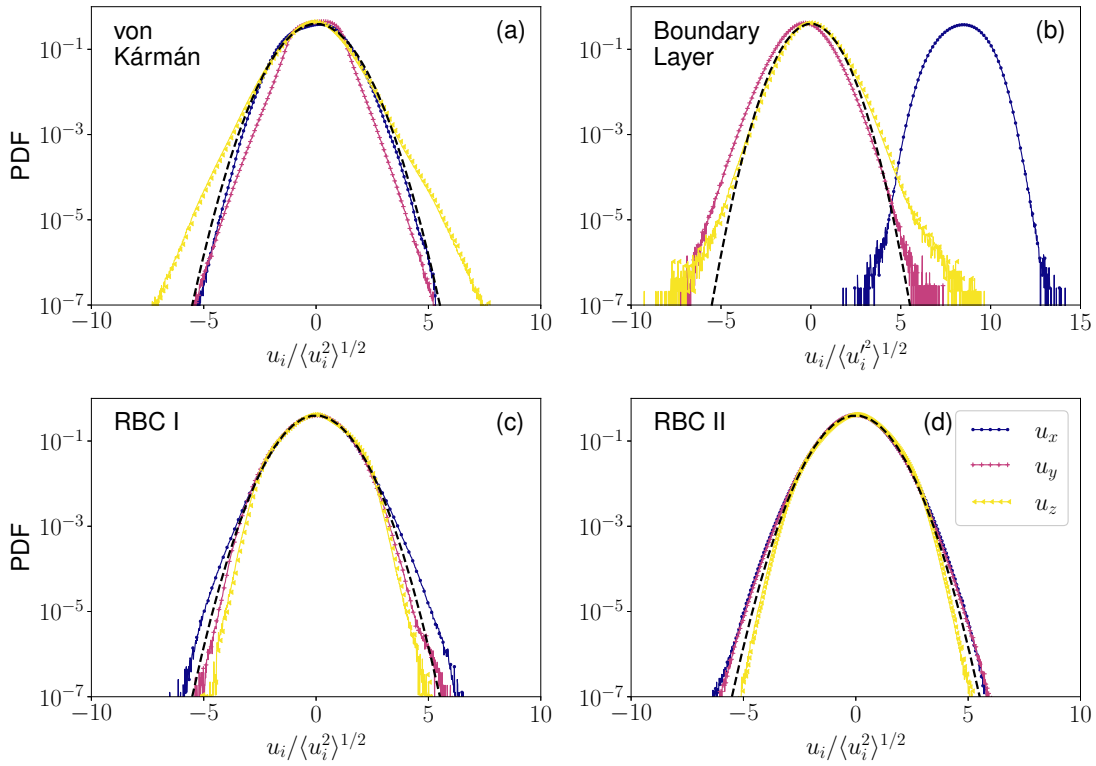

Figure 4.1: Standardised velocity component PDFs normalised using the rms for von Kármán and RBC and standard deviation for boundary layer. The dashed black line is a Gaussian with zero mean and unit standard deviation. The PDFs in x-, y- and z-direction are shown in blue, pink and yellow, respectively.

direction, normal to the propellers, the PDF has super-Gaussian tails, as can be seen from the data presented in figure 4.1 (a), with a flatness value or 3.44 (see table 4.1). This indicates that extreme velocity events are more likely in the z-direction compared to the x- and y-directions, confirming that von Kármán flow is not fully isotropic and large-scale dynamics are present (Ouellette et al., 2006). These are dominated by shearing and pumping modes as outlined in section 1.6.1. Furthermore, we find that the ratio of transverse (x- and y-components) and axial (z-component) rms velocity varies around 1.5 as found by Voth et al. (2002) for different propeller speeds, indicating that the large-scale dynamics do not depend strongly on the Reynolds number.

The PDFs of the velocity components in the bulk of Rayleigh-Bénard convection at two different Rayleigh numbers, $Ra = 5.25 \cdot 10^8$ (RBC I) and $Ra = 1.53 \cdot 10^9$ (RBC II) are shown in figure 4.1 (c) and (d), behave slightly differently. The PDF in x-direction of RBC I is slightly super-Gaussian while in y- and z-directions the PDFs are slightly sub-Gaussian

flow type	$(\sigma_{u_x},\sigma_{u_y},\sigma_{u_z})$ [m/s]	$\left(\frac{\langle u_x^4\rangle}{\sigma_{u_x}^4}, \frac{\langle u_y^4\rangle}{\sigma_{u_y}^4}, \frac{\langle u_z^4\rangle}{\sigma_{u_z}^4}\right)$
von Kármán	$(0.093, 0.083, 0.064)$	$(2.76, 2.32, 3.37)$
RBC I	$(0.028, 0.042, 0.049)$	$(3.18, 2.92, 2.83)$
RBC II	$(0.055, 0.057, 0.073)$	$(3.22, 3.14, 3.02)$
Boundary Layer	$(0.59, 0.40, 0.30)$	$(2.69, 3.29, 3.36)$

Table 4.1: Standard deviation and flatness of velocity component PDFs. For comparison a Gaussian has a flatness value of 3. Due to the large number of data points (see table 2.1) and the expected variance of kurtosis under normality (Fisher, 1930), fluctuations around the flatness value of 3 on the order of 10^{-5} are expected for a normal distribution. Therefore, the observed fluctuations indicate deviations from Gaussianity in the data.

(see table 4.1). For RBC II the flatness is higher for all three components, varying between 3.02 and 3.22, indicating an increase of extreme velocity events compared to RBC I. The differences between horizontal directions and the vertical direction become more apparent, resulting in super-Gaussian PDFs for the x- and y-direction and an approximately Gaussian PDF in z-direction. This may be connected to a more perturbed large-scale circulation, letting differences in x- and y-directions vanish. However, for both cases, the flatness is smallest in z-direction, indicating that less extreme velocity fluctuations are present in the direction of the temperature gradient.

The standard deviation is also increased for the RBC II case, implying more extreme velocity events, and thus a higher level of turbulence, which can be confirmed consulting the Taylor Reynolds number of 186 for RBC II and 147 for RBC I. With 270 the Taylor Reynolds number of the von Kármán flow is higher than for the two cases of RBC which indicates more extreme velocity events and is a potential reasoning for the higher deviations from a Gaussian for the velocity statistics of von Kármán flow compared to the RBC cases.

The final discussed dataset in this chapter is of the turbulent zero-pressure-gradient boundary layer where we only focus on a sub-volume in the logarithmic region as shown in figure 2.6. For this sub-volume the velocity component PDFs are shown in figure 4.1 and we found that the PDFs also near Gaussian. For the spanwise and wall-normal direction the PDFs are super-Gaussian with flatness values 3.29 and 3.36 respectively and zero mean while the PDF in streamwise direction has sub-Gaussian tails with a flatness value of 2.69 and a non-zero mean of $8.4\,\langle u_x^2\rangle^{1/2} \approx 4.95$ m/s.

4.2 Acceleration PDFs

Acceleration PDFs of Lagrangian particles have been calculated for numerical simulations of HIT (Bentkamp et al., 2019; Biferale, Boffetta, Celani, Devenish, Lanotte and Toschi, 2004; Lawson et al., 2018; Mordant, Lévêque and Pinton, 2004), experimental data of approximately homogeneous and isotropic turbulence (Porta et al., 2001; Lalescu and Wilczek, 2018; Lawson et al., 2018; Mordant, Lévêque and Pinton, 2004) and numerical data of Rayleigh-Bénard convection (Schumacher, 2009). The PDFs have wide tails with flatness values much higher than the value 3 for a Gaussian. In figure 4.2, we see that the PDFs of all acceleration components indeed are non Gaussian with heavy tails for all datasets. For both the von Kármán flow and Rayleigh-Bénard convection, we find that the results agree with the literature mentioned at the beginning of this section. For the two cases of RBC and the boundary layer, isotropy seems to be approximately restored on small scales with only small variations in the standard deviation and flatness of the different acceleration components, as it can be seen in table 4.2.

We will now compare the flatness of the acceleration PDFs with respect to the Taylor Reynolds number. From previous investigations, for example Yeung et al. (2006); Ishihara et al. (2007); Buaria and Sreenivasan (2022), we expect the flatness to increase with Reynolds number. This expectation is indeed confirmed given that the boundary layer has the smallest Taylor Reynolds number with 108 and flatness values between 7.7 and 9.9, which is followed RBC I with $Re_\lambda = 147$ and flatness values between 17.0 and 19.6, and the von Kármán flow has the highest Taylor Reynolds number of 270 and flatness values between 33.4 and 43.4, as shown in table 4.2. When comparing RBC I and RBC II, we would expect that the flatness of RBC II would be higher than for RBC I which is not the case. This might be due to the standard deviation of RBC II being three times higher than the standard deviation of RBC I. It should also be noted that both Taylor Reynolds numbers are of the same order, so the expected differences should not be large.

4.3 Curvature PDFs

For the curvature PDFs we expect power laws as reported in Braun et al. (2006) for numerical simulations of HIT, Xu et al. (2007) for von Kármán flow and Alards et al. (2017) for rotating

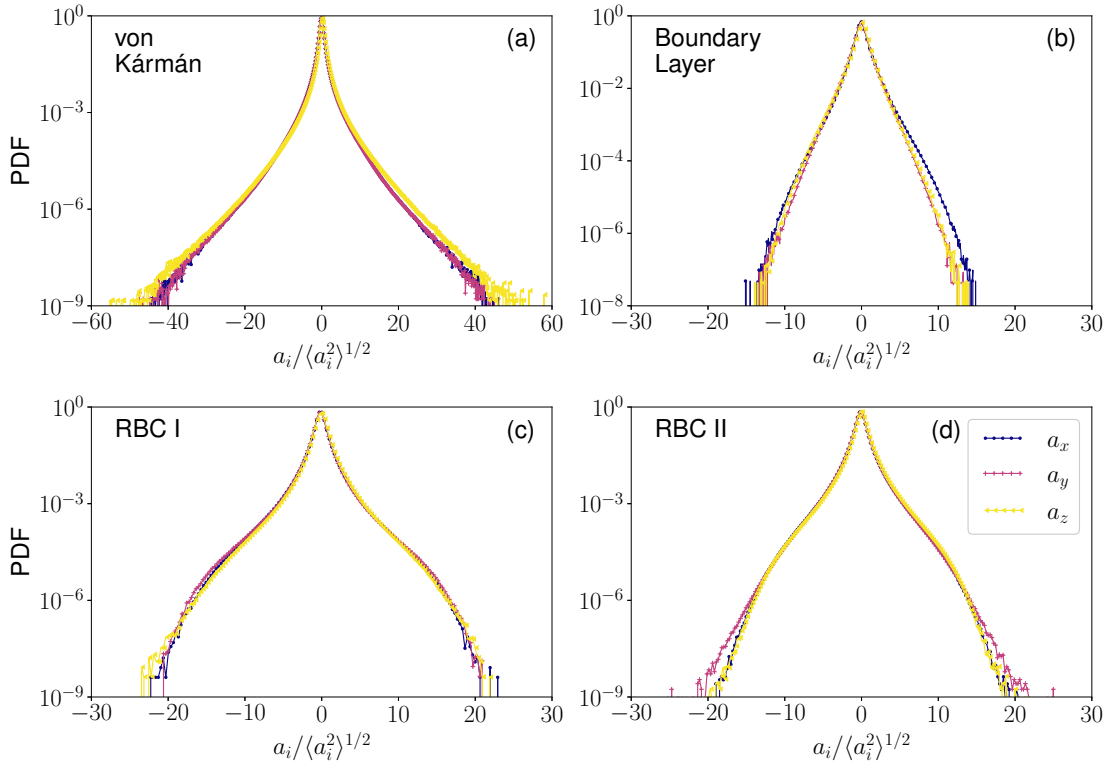

Figure 4.2: PDFs of acceleration components for all four datasets normalised using the rms values of the respective components. The PDFs in x-, y- and z-direction are shown in blue, pink and yellow, respectively.

flow type	$(\sigma_{a_x},\sigma_{a_y},\sigma_{a_z})$ [m/s^2]	$\left(\frac{\langle a_x^4\rangle}{\sigma_{a_x}^4}, \frac{\langle a_y^4\rangle}{\sigma_{a_y}^4}, \frac{\langle a_z^4\rangle}{\sigma_{a_z}^4}\right)$
von Kármán	(1.91, 1.89, 1.70)	(33.82, 33.44, 43.35)
RBC I	(0.024, 0.025, 0.026)	(18.75, 19.62, 17.01)
RBC II	(0.073, 0.074, 0.076)	(14.58, 14.08, 14.91)
Boundary Layer	(45.51, 40.17, 40, 69)	(9.89, 7.67, 8.63)

Table 4.2: Standard deviation and flatness of acceleration component PDFs for all four datasets.

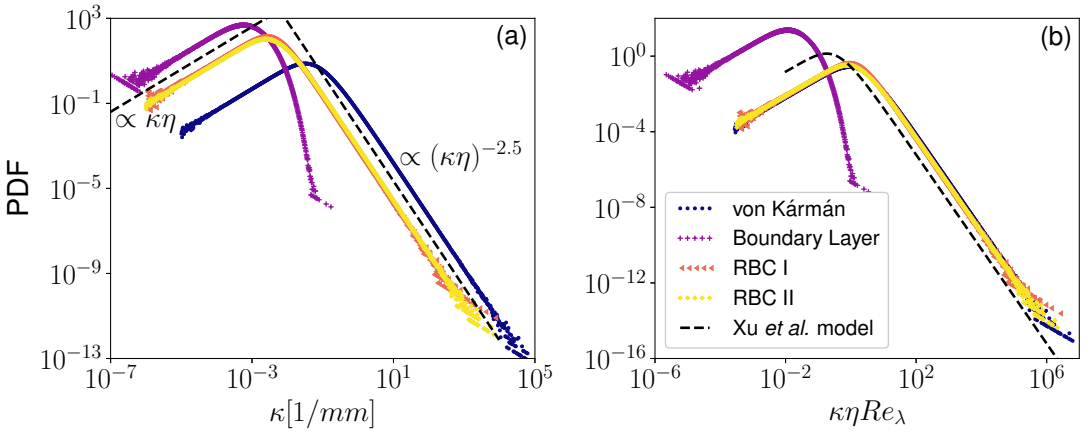

Figure 4.3: Comparison of the (a) curvature PDFs for all datasets and (b) re-scaled curvature PDFs using Heisenberg-Yaglom scaling (eq. 4.2).

and non-rotating RBC. All reported a linear PDF for small curvature values and a -2.5 power law for high values of the curvature. These exponents can be derived under the assumption that velocity and acceleration components are Gaussian independent variables (Xu et al., 2007), as described in section 1.7.4. Here, we provide a comparison of curvature PDFs across the four datasets to probe potential universality in the curvature PDFs in laboratory flows and to analyse the effect of anisotropy of the geometry of tracer particles. We also include a brief comparison of the model by Xu et al. (2007) before investigating models for the curvature PDF in more detail in chapter 6.

In figure 4.3 (a), the curvature PDFs of the different datasets are shown. We find that for von Kármán flow and Rayleigh-Bénard convection the PDFs have the expected linear PDF for small curvature values and $P(\kappa) \propto (\kappa\eta)^{-2.5}$ for high curvature values as presented in Braun et al. (2006); Xu et al. (2007); Alards et al. (2017). The curvature PDF of the boundary layer shows clear differences compared to the PDFs of the other two flow types. The left tail of the curvature PDF is linear but high curvature events are suppressed in the boundary layer and therefore the right tail of the curvature PDF of the boundary layer is no longer of power-law form. Generally, the curvature of the particle trajectories in the boundary layer (with the smallest Reynolds number) tends to be smaller compared to the other three datasets. The curvature of the two RBC cases is of the same order across the whole range of curvature values, while the trajectories in von Kárman flow tend to be more curved compared to the other datasets.

Non-dimensionalising the curvature using the rms of acceleration and velocity

$$\kappa = \frac{|\boldsymbol{a}_n|}{|\boldsymbol{u}|^2} \propto \frac{\langle a^2 \rangle^{1/2}}{\langle u^2 \rangle} \,. \tag{4.1}$$

allows us to take Reynolds numnber effects into account. For that, we utilise the definition of the Taylor Reynolds number (eq. (1.32)) and Heisenberg-Yaglom scaling (eq. (1.40)) under the assumption that a_0 is a constant, resulting in:

$$\begin{aligned}
\kappa \frac{\sigma_u^2}{\sigma_a} &= \kappa \frac{Re_\lambda (\varepsilon \nu)^{1/2}}{\sqrt{15}} \frac{1}{\sigma_a} \\
&\propto \kappa \frac{Re_\lambda (\varepsilon \nu)^{1/2}}{\sqrt{15}} \frac{1}{a_0^{1/2} \varepsilon^{3/4} \nu^{-1/4} \delta_{ij}} \\
&= \kappa \frac{Re_\lambda}{\sqrt{15 a_0} \varepsilon^{-1/4} \nu^{3/4}} \\
&\propto \kappa Re_\lambda \eta \,.
\end{aligned} \tag{4.2}$$

The re-scaled curvature PDFs are shown in figure 4.3 (b) where the curvature PDFs of the von Kármán flow and Rayleigh-Bénard convection for the two Rayleigh numbers collapse onto a master curve while the PDF of the turbulent boundary layer does not collapse onto this master curve. This is not a surprise as the curvature PDF of the boundary layer is phenomenologically different from the curvature PDFs of the other discussed datasets. Even when taking Reynolds number effects into account, the curvature tends to be smaller in the boundary layer compared to the other datasets. For the von Kármán flow and the bulk of RBC on the other hand it can be concluded that the curvature PDFs are determined by velocity and acceleration fluctuations. This means the curvature PDF is independent of the geometry of the flow or type of turbulence production, as suggested by Alards et al. (2017), at least for von Kármán and the bulk of RBC, and on this basis we suggest the same to hold more generally for flows with weak levels of anisotropy. In figure 4.3 (b), we also include a comparison of the model PDF derived by Xu et al. (2007) (eq. (1.99)) and the non-dimensionalised curvature PDFs of the four datasets. We can see that the tails of the model PDF and PDFs of the data have the same tails, however the peak is underestimated for the boundary layer and overestimated for the von Kármán flow and RBC. The model is based on independent Gaussian statistics for velocity and acceleration components. We have

seen in section 4.2 that the acceleration components are not Gaussian. A further discussion of this model, along with an improved model will be presented in chapter 6.

Now focusing on the curvature PDFs in the different datasets separately, shown in dark blue in figure 4.4, we can further analyse the origin of high and low curvature events and the effect of large-scale structures. The curvature is defined as $\kappa = |\boldsymbol{a}_n|/|\boldsymbol{u}|^2$, therefore high curvature can either originate from high normal accelerations or low velocity events. Biferale, Boffetta, Celani, Lanotte and Toschi (2004); Biferale and Toschi (2005) showed that the occurrence of vortex tubes, e.g. structures where high curvatures would be expected, is correlated to high acceleration events. However, Xu et al. (2007) showed that high curvature events are mainly generated by low velocity events, and that there is no strong correlation between high curvature events and high values of the normal acceleration. Low velocity events are less likely in a strong unidirectional flow, and therefore high curvature events are less likely, resulting in a suppression of the right tail of the curvature PDF.

Curvature statistics are affected by large-scale flow reversals (Xu et al., 2007), which occur on small time scales. To filter out these flow reversals, we average over different time scales. Ideally, the filter scale and the time scale of the flow reversals are comparable but the time scale of the flow reversals cannot be extracted from the provided data. For the filtered curvature it is then possible to connect curvature with the more intuitive idea of vorticity and to detect correlations between high-normal-acceleration events vortex filaments (Biferale and Toschi, 2005).

The filtering was only applied to the von Kármán flow and RBC as the boundary layer curvature PDF is phenomenologically different from the curvature PDFs of the other two flow types. For von Kármán flow, filter widths of one, five and ten Kolmogorov times (dark to light blue) were used to match filter scales in Xu et al. (2007) and compare the results. For the two cases of RBC, the filter scales are chosen to be below one free fall time which is approximately $10\tau_\eta$. Therefore for RBC one, five and seven Kolmogorov units were used as filter times. For all three datasets, filtering changes the shape of the PDFs. For small curvature events the probability of these small curvature events decreases with increasing filter scale. This compares well with the results reported by Xu et al. (2007). For high curvature events on the other hand, the PDFs in Xu et al. (2007) have also suppressed right tails where here the right tails of the PDFs seem to remain relatively stable for high curvature

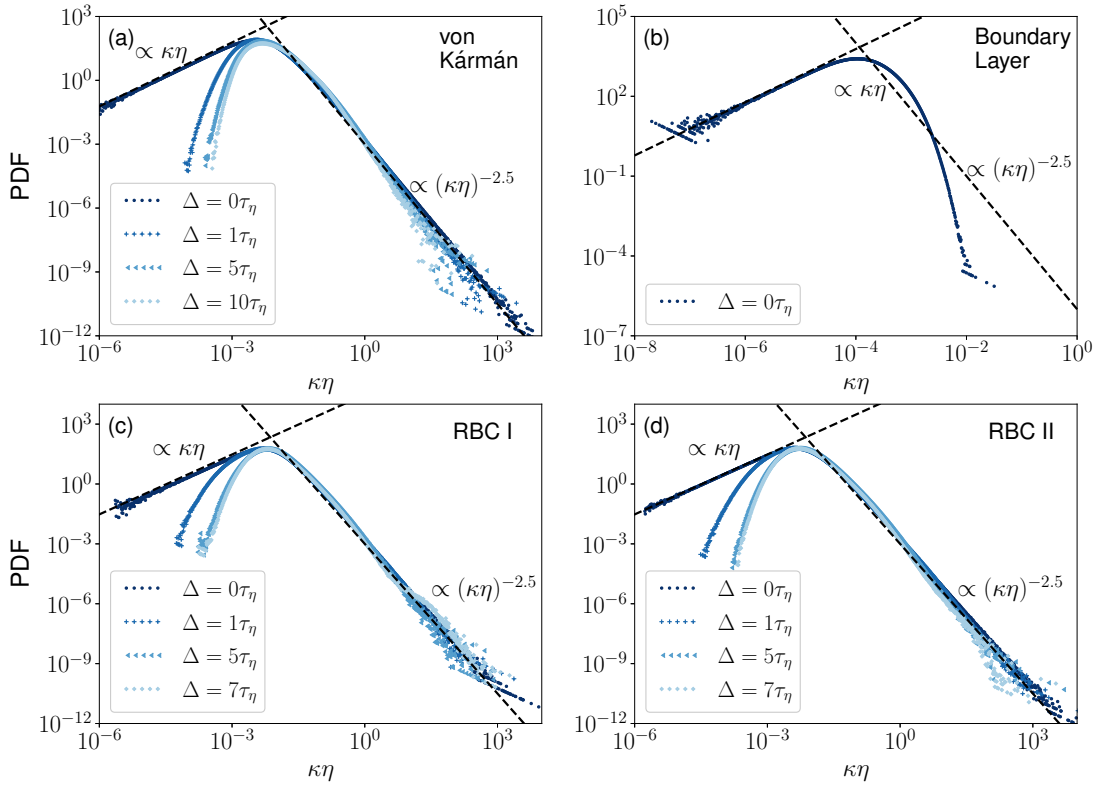

Figure 4.4: Curvature PDFs for all datasets and for von Kármán flow, RBC I and RBC II PDFs of the filtered torsion. Dark blue to light blue indicates an increasing filter scale, the maximal filter time is adjusted for the RBC cases to stay below the free fall time of approximately $10\tau_\eta$. References lines $\kappa\eta$ and $(\kappa\eta)^{-2.5}$ are shown for all datasets.

values.

4.4 Torsion PDFs

We will now consider the results of the torsion statistics. As the torsion involves the third time derivative, the measurements presented here have to be taken with caution. This is due to the fact that in the estimation of the experimental uncertainty, the third derivative is assumed to be noise as outlined in section 2.1.1. From the work on DNS of HIT by Scagliarini (2011), we are expecting a constant PDF for small torsion values and a PDF $\propto \tau^{-3}$. In figure 4.5 (a), we see that the PDFs for all datasets have the expected power laws. This is also the case for the boundary layer, despite differences in the curvature PDFs. Without non-dimensionalising and taking Reynolds number effects into account, the torsion of the RBC datasets and boundary layer is of similar order while the torsion PDF for von Kármán flow is shifted towards higher values.

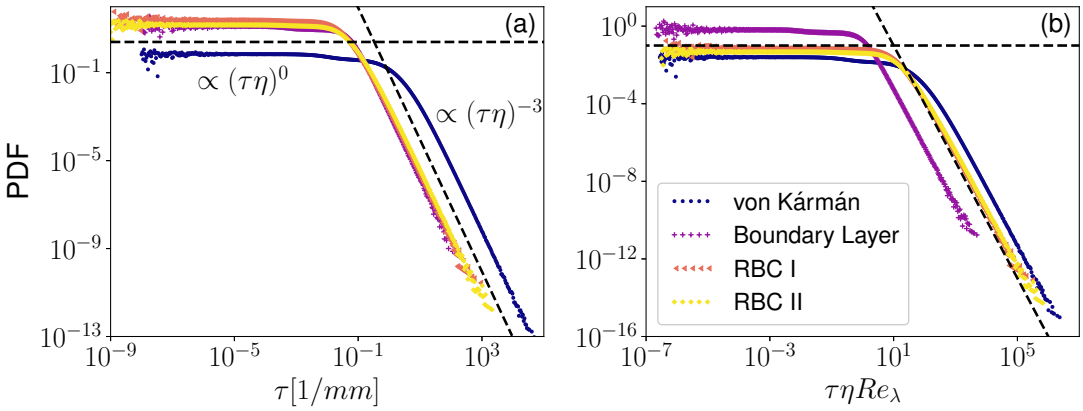

Figure 4.5: Comparison of (a) the torsion PDFs for all datasets and (b) torsion PDFs re-scaled using Heisenberg-Yaglom scaling (eq. 1.40).

The torsion can be non-dimensionalised in the same way as the curvature:

$$\tau = \frac{\boldsymbol{u}\cdot(\boldsymbol{a}\times\dot{\boldsymbol{a}})}{|\boldsymbol{u}|^6\kappa^2} \propto \frac{\langle u^2\rangle^{1/2}\langle a^2\rangle^{1/2}\frac{\langle a^2\rangle}{\langle u^2\rangle^{1/2}}}{\langle u^2\rangle^3\left(\frac{\langle a^2\rangle^{1/2}}{\langle u^2\rangle}\right)^2} = \frac{\langle a^2\rangle^{1/2}}{\langle u^2\rangle} \ . \tag{4.3}$$

Using this together with the Heisenberg-Yaglom re-scaling and the definition of the Taylor Reynolds number, the torsion PDFs can be re-scaled taking Reynolds number effects into account (fig. 4.5 (b)) as seen for the curvature (eq.(4.2)). While the torsion PDFs for all datasets become closer when re-scaled, they do not collapse onto a master curve like for the curvature and there is still a Re_λ dependence present where higher torsion becomes more likely with increasing Reynolds number. As outlined in section 3.1.3, torsion measurements have to be taken with caution which could be an explanation for this behaviour. When applying Heisenberg-Yaglom scaling to the torsion, we assume that a_0 is constant, which holds only in the absence of intermittency. Since torsion includes smaller scales through the third time derivative, intermittency effects may be more pronounced in torsion measurements than in curvature measurements.

While the PDFs of von Kármán flow and RBC are comparably close, the boundary layer torsion PDF is one order of magnitude higher for small torsion values, indicating that trajectories in a flow with a strong unidirectional mean flow are generally less twisted.

To filter large-scale flow reversals, the same filtering approach as for the curvature was used where the torsion gets averaged over different time intervals along the trajectory. This

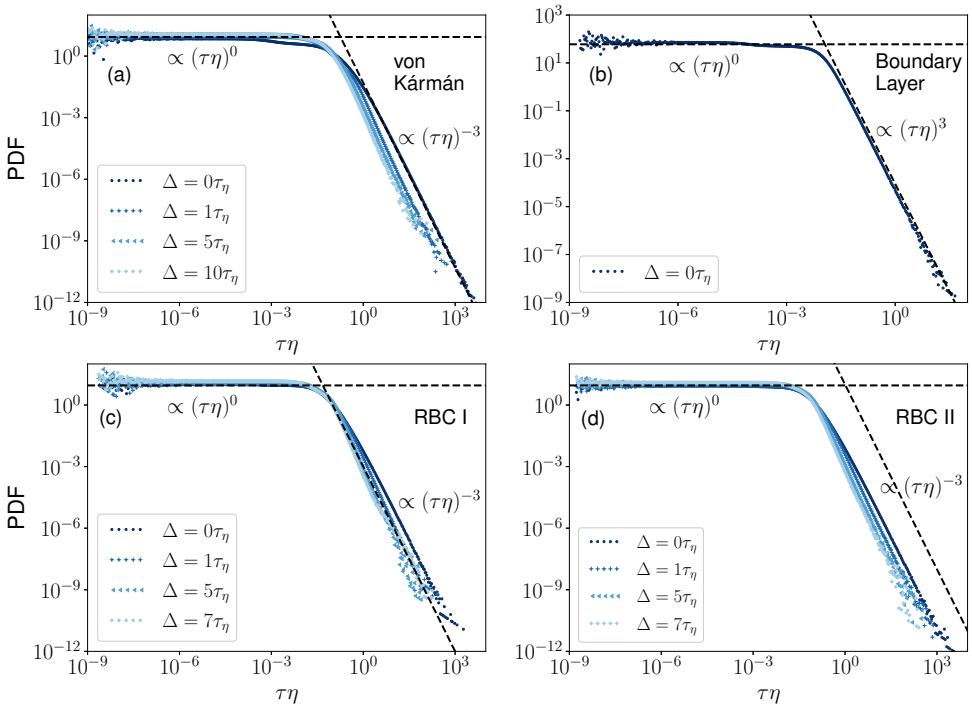

Figure 4.6: PDFs of the torsion for all datasets (dark blue) and for von Kármán flow, RBC I and RBC II PDFs of the filtered torsion. Dark blue to light blue indicates an increasing filter scale, the maximal filter time is adjusted for the RBC cases to stay below the free fall time of approximately $10\tau_\eta$. References lines $(\tau\eta)^0$ and $(\tau\eta)^{-3}$ are shown for all datasets.

filtering has only been applied to the datasets of the von Kármán flow and Rayleigh-Bénard convection where the opposite to the curvature is found. The PDF of small torsion values remains at its approximately constant level when filtered while the right tail of the PDFs get lighter with high torsion events becoming less likely with increasing filter width. This can be explained using the definition of the torsion, and substituting the curvature in:

$$|\tau| = \frac{\boldsymbol{u}\cdot(\boldsymbol{a}\times\dot{\boldsymbol{a}})}{|\boldsymbol{u}|^6\kappa^2} = \frac{\boldsymbol{u}\cdot(\boldsymbol{a}\times\dot{\boldsymbol{a}})}{|\boldsymbol{u}|^6\frac{|\boldsymbol{u}\times\boldsymbol{a}|^2}{|\boldsymbol{u}|^6}}$$
$$\propto \frac{|\dot{\boldsymbol{a}}|}{|\boldsymbol{u}||\boldsymbol{a}|}$$

By filtering out flow reversals, e.g. small velocity events, and assuming that $|\boldsymbol{a}|$ and $|\dot{\boldsymbol{a}}|$ are constant, the filtering therefore is expected to suppress high torsion events.

4.5 Curvature Vector

In sections 4.1 and 4.2, we have shown that all flow types are statistically anisotropic caused by large-scale motions, either due to propeller motion for von Kármán flow, a temperature gradient for Rayleigh-Bénard convection or a strong mean flow for the ZPG boundary layer. For small levels of anisotropy, for example introduced through propeller motion or a temperature gradient, these effects of anisotropy cannot be seen in curvature and torsion measurements, differences can be related back to the Reynolds number. For larger levels of anisotropy like a strong mean flow in the boundary layer, the effects cannot be related to a specific direction. This is expected as curvature and torsion are global measurements that are coordinate independent and mix information across the different spatial directions. To gain further insight into the effect of anisotropy, the curvature vector is introduced (eq. (1.78)) and we will discuss its statistics next.

The PDFs of the curvature vector components are presented in figure 4.7. The right tails follow the same -2.5 power law for von Kármán flow and RBC as for the full curvature PDF while for the boundary layer the tail differs from the -2.5 power law and is qualitatively similar to the right tail of the full curvature PDF. The left tail is now constant for small values of the curvature for all datasets and directions, which can be predicted assuming Gaussian random variables (sec. 1.7.1) for the velocity and acceleration components following the same arguments as presented by Xu et al. (2007) for the curvature. The differences in different directions become apparent when comparing the heights of the plateaux. For the boundary layer this can be seen directly in figure 4.7 (b) with differences between streamwise and wall-normal and spanwise directions being around one order of magnitude. For the other three datasets, we can see in the insets of the figure 4.7 (a), (c) and (d) that the plateau heights of the different directions differ markedly on a linear scale. For the von Kármán flow it is approximately 1.7 times more likely for the curvature to be small in x- and y-directions compared to the z-direction. For RBC I small curvature events are 2.5 more likely in z-direction compared to the x-direction and for RBC II the difference is 1.65. Therefore, it can be said that the anisotropy decreases with increasing Reynolds number for the two cases of Rayleigh-Bénard convection.

An intuitive way to explain these differences is to connect the curvature with velocity.

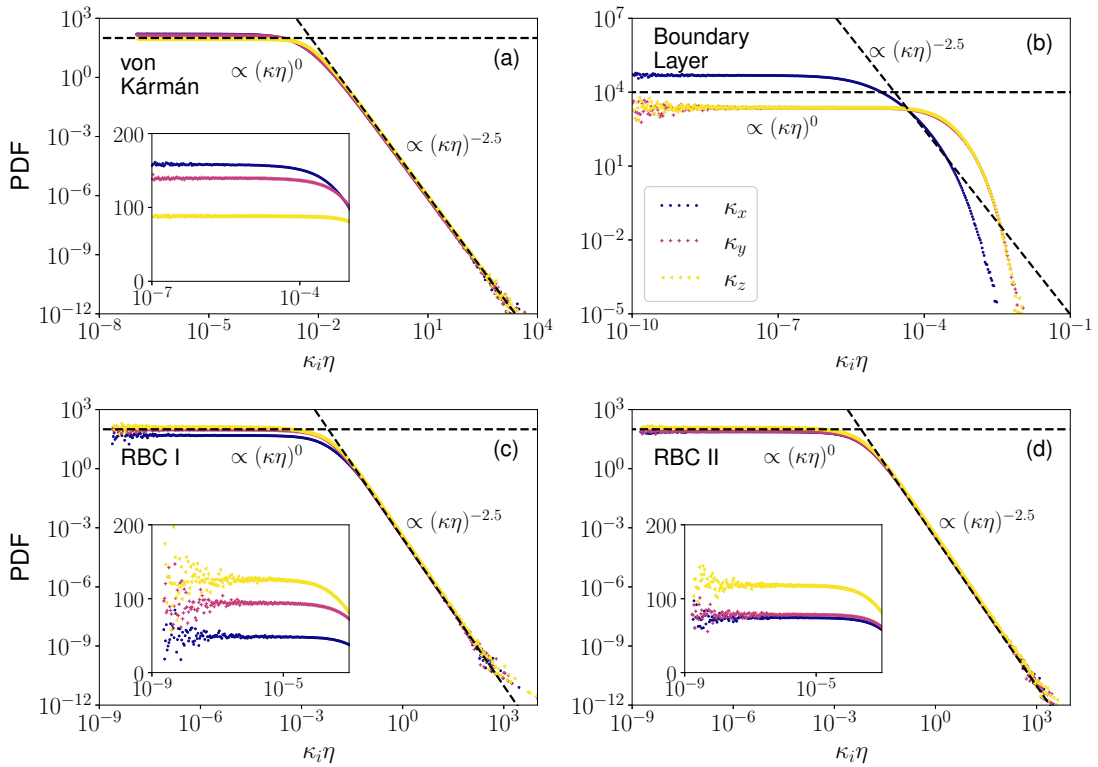

Figure 4.7: PDFs of the components of the curvature vector for the different datasets. References lines $(\kappa\eta)^0$ and $(\kappa\eta)^{-2.5}$ are shown for all cases.

If the velocity is high in one direction, the trajectory is more stretched in this direction and therefore would be less curved in that direction. This can be seen for the boundary layer where small curvature values are more likely in streamwise (x) direction compared to the spanwise (y) and wall-normal (z) direction. To further quantify this, we calculated the PDFs of the curvature vector conditioned on small velocities and large velocities. For small velocities, that is $u_i/\sigma_{u_i} \leq 0.1$ for von Kármán flow, RBC II and y- and z-component of the boundary layer and $\frac{u_x-\overline{u_x}}{\sigma_{u_x}} \leq -2$ for the stream-wise direction of the boundary layer and for large velocities, we are using $u_i/\sigma_{u_i} \geq 3$ for von Kármán flow, RBC II and y- and z-component of the boundary layer and $\frac{u_x-\overline{u_x}}{\sigma_{u_x}} \geq 2$ for the stream-wise direction of the boundary layer. As previously seen, differences for the two RBC datasets can be connected to Reynolds number effects, therefore only conditional PDFs for RBC II are calculated. For simplicity, only PDFs conditioned on the velocity in x-direction are shown. The right column of figure 4.8 shows the PDFs of curvature vector components conditioned on large velocities. The PDFs show an increased probability of small curvature events in x-direction which agrees with the physical intuition that trajectories are less curved in the direction of high velocity. Additionally, it can be seen that high curvature events are suppressed, resulting in change of the right tail of the curvature PDF, similar to the curvature PDF of the boundary layer. Conditioning on small velocities (fig. 4.8, left columns) lead to less small curvature events in x-direction compared to the other directions. This is not the case for the boundary layer, which might be caused by the filtering approach we took, where small velocities are still larger than zero, resulting in a higher likelihood of small curvature events in x-direction compared to the other two directions. An additional feature that can be observed for the boundary layer PDFs is the flattening of the right tail and forming a power law, indicating that a strong unidirectional flow is the origin for the change of the power law of the right tail for the curvature PDF of the boundary layer.

The presented curvature vector statistics, specifically for the boundary layer, indicate that high velocities in one direction lead to an increase of low curvature events and decrease of high curvature events in that direction. With only small velocities present in one direction, small curvature events are less likely compared to the other directions. For the boundary layer, it can be concluded that trajectories rarely curve against the direction of mean flow resulting in either helical or meandering trajectories.

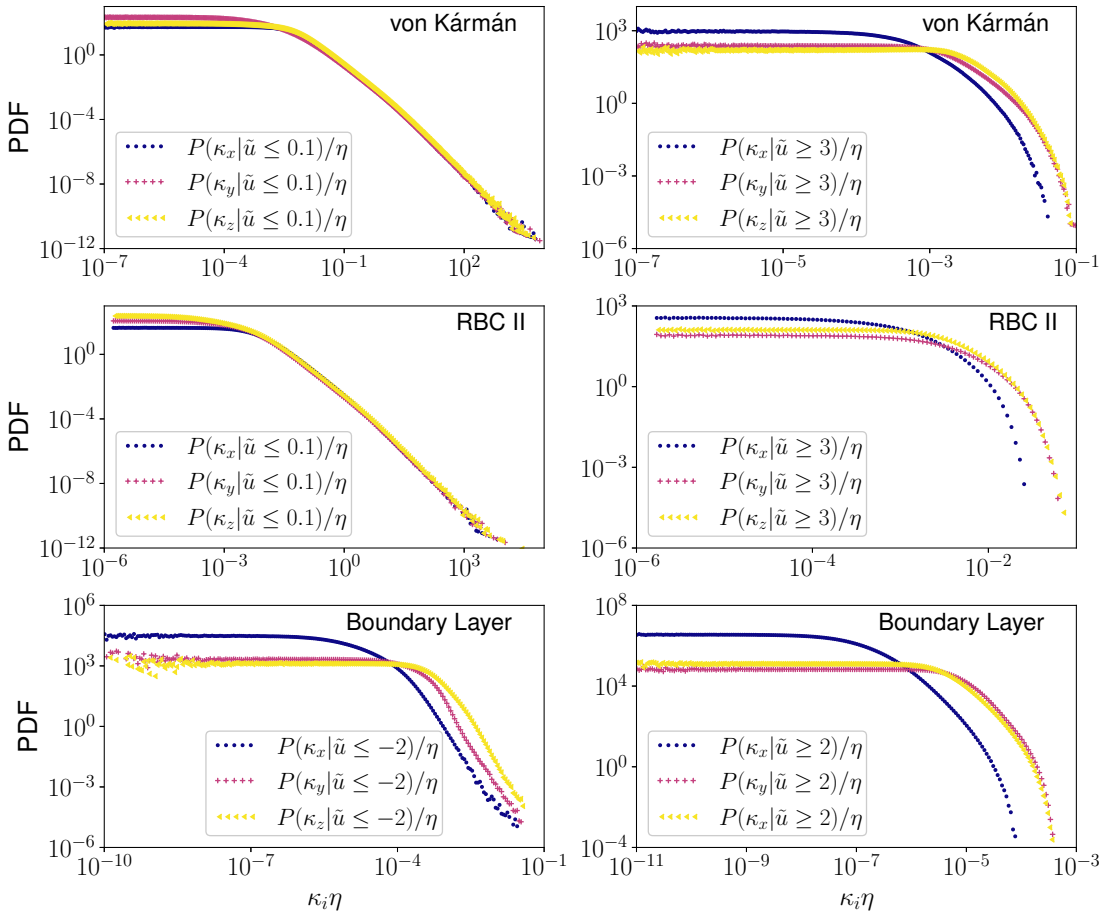

Figure 4.8: PDFs of the curvature vector components, conditioned on the velocity $\tilde{u}$. For von Kármán and RBC $\tilde{u} = |u_x/\sigma_{u_x}|$, for the boundary layer $\tilde{u} = \frac{u_x - \overline{u_x}}{\sigma_{u_x}}$.

4.6 Summary

In this project, we calculated Lagrangian statistics for four experimental datasets of three different types of turbulent flows. The focus was to study the effect of anisotropy on the geometry of tracer particle trajectories, for that, we introduced the curvature vector and calculated the statistics of its components. We connected the differences in the different components with large-scale motion introduced by the experimental setups.

The datasets we considered were von Kármán flow with $Re_\lambda = 270$, Rayleigh-Bénard convection (RBC) in the bulk at two different Rayleigh numbers $Ra = 5.3 \cdot 10^8$ and $Ra = 1.53 \cdot 10^9$ with $Re_\lambda = 147$ and 186 respectively and and a turbulent zero-pressure-gradient boundary layer in the logarithmic region where $Re_\tau = 2295$ and $Re_\lambda = 108$.

Firstly, we calculated the velocity and acceleration statistics, where for all four datasets the velocity statistics are near Gaussian. For von Kármán flow and RBC, the PDFs of all components have approximately zero mean while for the boundary layer, only the PDFs in spanwise and wall-normal direction have approximately zero mean, while in streamwise direction the mean is $8.4\langle u_x^2\rangle^{1/2}$. The acceleration PDFs all have wide tails as expected, and isotropy is restored on small scales for the boundary layer with only small variations in the PDFs in the different directions.

The power laws found for the curvature PDF of von Kármán flow and RBC agree with previous results from numerical simulations of homogeneous and isotropic turbulence (HIT) (Braun et al., 2006), experiments of von Kármán flow (Xu et al., 2007) and numerical simulations of Rayleigh-Bénard convection (Alards et al., 2017). The curvature PDF of the boundary layer has the same tail for small values of the curvature but deviates from the -2.5 power law for high values. This is most likely due to the strong unidirectional flow suppressing high-curvature events and a strong unidirectional flow breaks the apparent universal form of the curvature PDF. The curvature PDFs can be re-scaled using Heisenberg-Yaglom scaling to take Reynolds number effects into account, resulting in a collapse onto a master curve for von Kármán flow and RBC. The collapse for the boundary layer does not work as the shape of the PDF is phenomenologically different.

For the torsion PDFs, we find that all four datasets show the same scaling as for numerical simulations of homogeneous isotropic turbulence (Scagliarini, 2011) and RBC (Alards et al.,

2017). By re-scaling using Heisenberg-Yaglom scaling, the PDFs of von Kármán flow and RBC collapse onto a master curve while the torsion PDF of the boundary layer is shifted towards smaller values of the torsion.

For the components of the curvature vector, however, we observe marked differences between datasets and spatial directions. Firstly, the x-component of curvature vector is much more likely to be smaller in stream-wise direction compared to the span-wise and wall-normal direction for the ZPG boundary layer, reflecting the physical intuition that trajectories of particles with strong stream-wise velocity are less curved against the flow and more likely to meander in wall-normal and span-wise directions. Secondly, also for von Kámán flow and Rayleigh-Bénard convection we find differences in the low-curvature tails of the curvature vector PDFs in the respective spatial directions. A comparison between velocity statistics and curvature vector statistics reveals that low-curvature events occur mostly in directions where velocity fluctuations are stronger. This aligns with the observations made for the turbulent boundary layer.

In summary, through connecting the statistics of the curvature vector with that of velocity fluctuations we demonstrate that large-scale motion in a given spatial direction results in meandering rather than helical trajectories. Further work based on this project will be discussed in chapter 7.

Chapter 5

Curvature of Magnetic Field Lines

The work in this chapter was started during a research visit with Michael Wilczek at the University of Bayreuth in the summer of 2023 and the work presented here is currently being prepared for publication.

Magnetohydrodynamic (MHD) turbulence occurs in electrically conducting fluids such as liquid metals or plasmas in the fluid approximation. To describe the dynamics of the flow and the magnetic field, the Navier Stokes equations are coupled with the Maxwell equations as outlined in section 1.6.4. MHD turbulence is present, for example, in the Sun and also plays a crucial role in many geophysical phenomena, such as magnetic fields generated by liquid metals in planetary cores, such as the Earth's magnetic field. Magnetic field lines are a common concept to visualise magnetic fields and the shape of these lines are used to describe different phenomena related to MHD turbulence, specifically in astrophysics. To further help with the understanding of MHD turbulence, we studied the geometry of magnetic field lines and stream lines. This is also helpful to understand the effects of anisotropy, introduced through a magnetic background field, on the geometry of magnetic field lines and stream lines.

In this chapter, we will cover the curvature statistics of magnetic field lines and stream lines of the flow of the datasets described in section 2.2 where an Eulerian approach has been taken. The curvature of the magnetic field lines κ_b or stream lines κ_u in the Eulerian

setting, as introduced in section 1.7.3, are restated here for reference:

$$|\kappa_b| = \frac{|\boldsymbol{b} \times \boldsymbol{b} \cdot \nabla \boldsymbol{b}|}{|\boldsymbol{b}|^3} \tag{5.1}$$

$$|\kappa_u| = \frac{|\boldsymbol{u} \times \boldsymbol{u} \cdot \nabla \boldsymbol{u}|}{|\boldsymbol{u}|^3} \tag{5.2}$$

where $\boldsymbol{b}$ is the field of magnetic field fluctuations, $\boldsymbol{u}$ is the field of velocity fluctuations. The terms $\boldsymbol{b} \cdot \nabla \boldsymbol{b}$ and $\boldsymbol{u} \cdot \nabla \boldsymbol{u}$ are the magnetic tension and inertial term. To distinguish between the curvature of the magnetic field lines and stream lines, we use an index u for the curvature of the stream lines and b for the curvature of the magnetic field lines. In analogy to the statistics of the Lagrangian trajectories in the previous chapter, I will present the statistics of the magnetic field fluctuations and velocity field fluctuations, as these are the analogous terms to the velocity of Lagrangian trajectories when comparing the curvature equations of the magnetic field lines and stream lines with the curvature of Lagrangian trajectories (eq. (1.79)), and of the magnetic tension and inertial term components in analogy to the acceleration of the curvature of Lagrangian trajectories first. Subsequently, I will discuss the statistics of the curvature of the magnetic field lines and stream lines. To measure the effect of anisotropy introduced through a magnetic background field, I will discuss the statistics of the curvature vector.

5.1 Magnetic Field Fluctuations and Velocity Field Fluctuations

The PDFs of the magnetic field fluctuations and velocity field fluctuations of the x-direction are presented in figure 5.1. The PDFs of the other directions are similar, hence we only show the PDFs of one direction for the datasets with no magnetic background field. The details for the other components can be extracted from table 5.1 for the magnetic field PDFs and table 5.2 for the velocity PDFs. For the magnetic field fluctuations of the datasets with no magnetic background field (fig. 5.1 (a)) all PDFs have super-Gaussian tails as previously observed by Seta et al. (2020). The flatness values of the x-component vary between 3.82 and 4.93 where the flatness decreases with increasing Reynolds number as shown in table 5.1. By introducing a magnetic background field where $B_0 \approx 13\sigma_{b_z}$, the PDFs of the magnetic field fluctuations (fig. 5.1 (b)) are better approximated by a Gaussian with flatness values

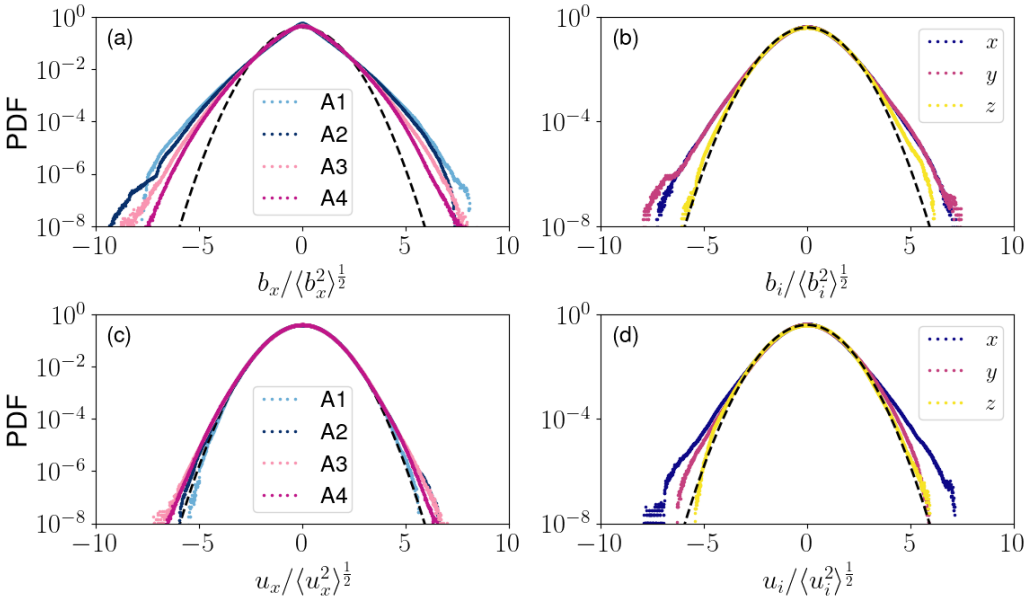

Figure 5.1: Standardised PDFs of the x-component for datasets A1-A4 (a) and all components for dataset B10 (b) of the magnetic field fluctuations and Standardised PDFs of the x-component for datasets A1-A4 (c) and all components for dataset B10 (d) of the velocity field fluctuations. The dashed line is a Gaussian with zero mean and variance of unity. For (a) and (c) the blue lines represent the standard diffusive datasets (A1 light blue and A2 dark blue) and pink lines represent the hyperdiffusive datasets (A3 light pink and A4 dark pink). For (b) and (d) the x-component is blue, the y-component pink and the z-component yellow.

Dataset	$(\sigma_{b_x},\sigma_{b_y},\sigma_{b_z})$	$\left(\frac{\langle b_x^4\rangle}{\sigma_{b_x}^4}, \frac{\langle b_y^4\rangle}{\sigma_{b_y}^4}, \frac{\langle b_z^4\rangle}{\sigma_{b_z}^4}\right)$	Re
A1	$(0.47, 0.47, 0.47)$	$(4.93, 4.81, 4.81)$	936
A2	$(0.51, 0.50, 0.51)$	$(4.65, 4.68, 4.67)$	2144
A3	$(0.57, 0.56, 0.57)$	$(3.99, 4.00, 3.97)$	4272
A4	$(0.61, 0.60, 0.60)$	$(3.82, 3.80, 3.79)$	9931
B10	$(0.78, 0.79, 0.86)$	$(3.42, 3.44, 3.14)$	7501

Table 5.1: Standard deviation and flatness of the magnetic field fluctuation components and Reynolds number. Datasets A1 and A2 are using standard diffusion and the remaining datasets are calculated using hyperdiffusivity.

Dataset	$(\sigma_{u_x},\sigma_{u_y},\sigma_{u_z})$	$\left(\frac{\langle u_x^4\rangle}{\sigma_{u_x}^4}, \frac{\langle u_y^4\rangle}{\sigma_{u_y}^4}, \frac{\langle u_z^4\rangle}{\sigma_{u_z}^4}\right)$	Re
A1	$(0.71, 0.71, 0.71)$	$(3.07, 3.13, 3.07)$	936
A2	$(0.71, 0.69, 0.70)$	$(3.07, 3.11, 3.10)$	2144
A3	$(0.69, 0.68, 0.69)$	$(3.12, 3.12, 3.14)$	4272
A4	$(0.67, 0.67, 0.67)$	$(3.10, 3.15, 3.14)$	9931
B10	$(0.92, 0.96, 1.07)$	$(3.42, 3.22, 3.06)$	7501

Table 5.2: Standard deviation and flatness of the velocity field fluctuation components and Reynolds number. Datasets A1 and A2 are using standard diffusion and the remaining datasets are calculated using hyperdiffusivity.

3.42, 3.44 and 3.14 in x-, y- and z-direction. The magnetic background field is in z-direction, resulting in the suppression of fluctuations parallel to the magnetic background field of the flow, as observed by Alexakis (2011) and Gallet and Doering (2015). The PDFs of the velocity fluctuations for the datasets without a magnetic background field are presented in figure 5.1 (c). The PDFs are near Gaussian with flatness values between 3.07 and 3.15 for the different components (table 5.2) with only small deviations between the different datasets. This aligns with results for MHD turbulence (Seta et al., 2020) and well known results in hydrodynamics (Townsend, 1947; Batchelor, 1953) and as seen in the previous section for the velocity statistics of Lagrangian tracer particles. By introducing a magnetic background field the deviations from a Gaussian are more significant (fig. 5.1 (d)) where the flatness values fluctuates between 3.06 and 3.42 for the different directions. The smallest flatness value of 3.06 is in the direction of the magnetic field (z-direction), indicating the suppression of extreme velocity events in that direction (Alexakis, 2011; Gallet and Doering, 2015).

5.2 Magnetic Tension and Inertial Term

The PDFs of the magnetic tension components are shown in the top row of figure 5.2 where it can clearly be seen that the PDFs are not Gaussian and have wide tails, reaching 10^{-10} around $100\sigma_{b\nabla b}$ for the datasets with no magnetic background field. Comparing that with the acceleration component PDFs as these are the terms analogue to the acceleration for the curvature of Lagrangian trajectories, we can see that the shapes of the PDFs are similar (Bentkamp et al., 2019; Hengster et al., 2024). The standard deviation is increasing with increasing Reynolds number for the datasets A1-A4. The effect of intermittency becomes apparent when comparing the flatness values of the standard diffusive datasets and the flatness values of the hyperdiffusive datasets. With increasing Reynolds number, more extreme events occur and the PDFs become wider, visible in the flatness (table 5.3) for the two types of viscosity. For the dataset with a magnetic background field, we find that less extreme events occur. This can seen especially for the z-direction, which has less extreme events with flatness value of 13.13 compared to the horizontal directions with flatness values of ≈ 18, indicating again the suppression of fluctuations in the direction parallel to the magnetic background field (Alexakis, 2011; Gallet and Doering, 2015).

The PDFs of the inertial term components are presented in figure 5.2 (c) and (d) and have the same shape as for the magnetic tension but are narrower for all cases (reaching 10^{-10} around $50\sigma_{u\nabla u}$) and therefore less intermittent than for the magnetic tension PDFs which has been shown in Carbone et al. (2004). This is also represented in the flatness values that are between 10.95 an 18.86 which can be related to the energy spectra (fig. 2.8) where less kinetic energy is in the small scales compared to magnetic energy. While the standard deviation is again increasing with increasing Reynolds number, the width of the PDFs only increases with Reynolds number when comparing the same type of diffusion operator. For the dataset with a magnetic background field, the partial two-dimensionalisation becomes visible by a suppression extreme events in z-direction compared to the other two directions.

5.3 Curvature PDFs

We will now discuss the statistics of the curvature of the magnetic field lines κ_b (eq. (5.1)) and the stream lines κ_u (eq. (5.2)) for the stream lines. The curvature PDFs for the

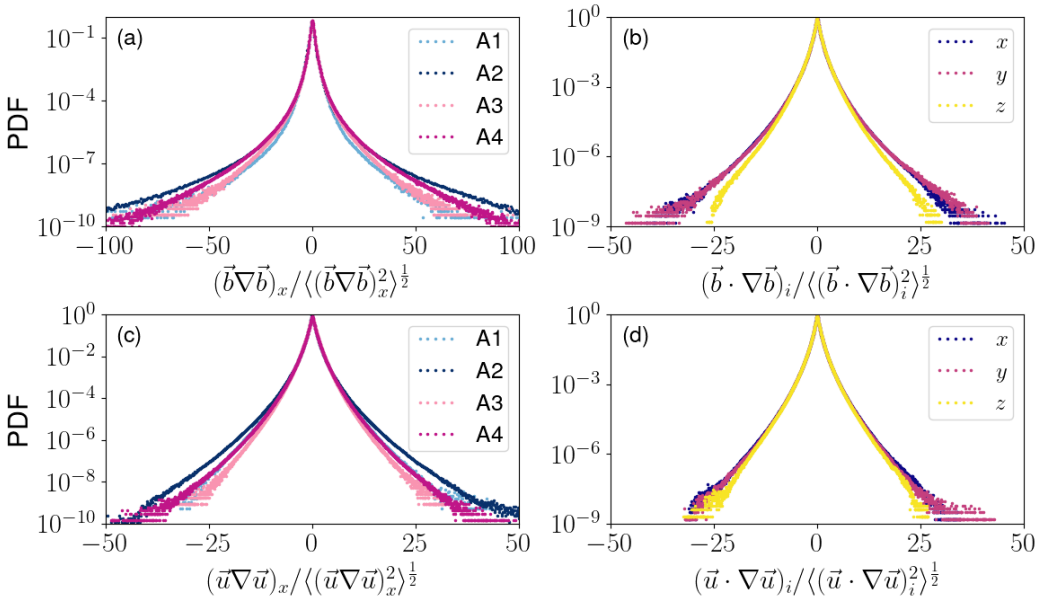

Figure 5.2: Standardised PDFs of the x-component for datasets A1-A4 (a) and all components for dataset B10 (b) of the magnetic tension and standardised PDFs of the x-component for datasets A1-A4 (c) and all components for dataset B10 (d) of the inertial term. For (a) and (c) the blue lines represent the standard diffusive datasets (A1 light blue and A2 dark blue) and pink lines represent the hyperdiffusive datasets (A3 light pink and A4 dark pink). For (b) and (d) the x-component is blue, the y-component pink and the z-component yellow.

Dataset	$(\sigma_{(\boldsymbol{b}\cdot\nabla\boldsymbol{b})_x}, \sigma_{(\boldsymbol{b}\cdot\nabla\boldsymbol{b})_y}, \sigma_{(\boldsymbol{b}\cdot\nabla\boldsymbol{b})_z})$	$\left(\frac{\langle(\boldsymbol{b}\cdot\nabla\boldsymbol{b})_x^4\rangle}{\sigma^4_{(\boldsymbol{b}\cdot\nabla\boldsymbol{b})_x}}, \frac{\langle(\boldsymbol{b}\cdot\nabla\boldsymbol{b})_y^4\rangle}{\sigma^4_{(\boldsymbol{b}\cdot\nabla\boldsymbol{b})_y}}, \frac{\langle(\boldsymbol{b}\cdot\nabla\boldsymbol{b})_z^4\rangle}{\sigma^4_{(\boldsymbol{b}\cdot\nabla\boldsymbol{b})_z}}\right)$	Re
A1	(1.97, 1.96, 1.96)	(17.18, 16.71, 16.11)	936
A2	(2.77, 2.77, 2.78)	(45.49, 41.27, 40.03)	2144
A3	(6.58, 6.57, 6.57)	(23.11, 22.84, 22.92)	4272
A4	(9.65, 9.65, 9.64)	(36.50, 36.80, 36.67)	9931
B10	(23.48, 23.42, 26.85)	(18.18, 17.99, 13.30)	7501

Table 5.3: Standard deviation and flatness of the magnetic tension components and Reynolds number. Datasets A1 and A2 are using standard diffusion and the remaining datasets are calculated using hyperdiffusivity.

Dataset	$(\sigma_{(\boldsymbol{u}\cdot\nabla\boldsymbol{u})_x}, \sigma_{(\boldsymbol{u}\cdot\nabla\boldsymbol{u})_y}, \sigma_{(\boldsymbol{u}\cdot\nabla\boldsymbol{u})_z})$	$\left(\frac{\langle(\boldsymbol{u}\cdot\nabla\boldsymbol{u})_x^4\rangle}{\sigma^4_{(\boldsymbol{u}\cdot\nabla\boldsymbol{u})_x}}, \frac{\langle(\boldsymbol{u}\cdot\nabla\boldsymbol{u})_y^4\rangle}{\sigma^4_{(\boldsymbol{u}\cdot\nabla\boldsymbol{u})_y}}, \frac{\langle(\boldsymbol{u}\cdot\nabla\boldsymbol{u})_z^4\rangle}{\sigma^4_{(\boldsymbol{u}\cdot\nabla\boldsymbol{u})_z}}\right)$	Re
A1	(7.93, 7.93, 7.89)	(13.91, 13.79, 13.97)	936
A2	(12.01, 12.03, 12.05)	(18.64, 18.86, 18.76)	2144
A3	(16.85, 16.84, 16.85)	(10.95, 11.02, 11.06)	4273
A4	(28.49, 28.46, 28.49)	(13.29, 13.09, 13.18)	9931
B10	(26.26, 25.75, 33.54)	(15.21, 14.57, 13.56)	7501

Table 5.4: Standard deviation and flatness of the inertial term components and Reynolds number. Datasets A1 and A2 are using standard diffusion and the remaining datasets are calculated using hyperdiffusivity.

different datasets (table 2.2) are presented in figure 5.3. Subfigure (a) shows the PDFs of the magnetic field line curvature and in subfigure (b) the PDFs normalised with the standard deviation of the magnetic field fluctuations and magnetic tension are shown. The PDFs of the curvature of stream lines and the stream line curvature normalised using the standard deviation of the velocity fluctuations and inertial term are shown in subfigures (c) and (d), respectively. For both types of diffusivity, the curvature PDFs of the magnetic field lines and the curvature PDFs of the stream lines have the same shape. That hyperdiffusion has no effect on the shape of the curvature PDF was already observed by Schekochihin et al. (2002) for the magnetic field line curvature. The results here show that this is also the case for the curvature of stream lines. For the curvature of the standard diffusive datasets (dark blue and purple) we observe that the curvature is more likely to be small compared to the hyperdiffusive datasets, while for the hyperdiffusive dataset the curvature tends to be higher, which might be related to the presence of more small-scale structures. Additionally, the differences between the different datasets are more apparent for the stream line curvature compared to the magnetic field line curvature. For the datasets with no magnetic background field, this correlates with the Reynolds number. For increasing Reynolds number the curvature PDF shifts towards higher curvature values. This can be connected with the smallest vortices, which are expected to be larger for a smaller Reynolds number. We will see that by taking the Reynolds number effects into account, the PDFs will collapse onto a master curve (fig. 5.3 (b), (d)).

The PDFs of the datasets with no magnetic background field all have the same shape, where the PDFs are linear for small values of the curvature. For high curvature values the magnetic field lines and stream lines behave differently. While for datasets without a background field the magnetic field lines exhibit a clear power law with exponents between -2.5 and -2.86 for high curvature values, the curvature PDFs of the stream lines only follow the power law for very high curvature values. These exponents are the predicted exponents by the models of Schekochihin et al. (2001) (-2.86) and of Xu et al. (2007) (-2.5), modified for the magnetic field line curvature by Yang et al. (2019). Both of the models are based on Gaussian statistics. However, we showed in the previous sections that these assumptions are generally not fulfilled for the presented datasets. That is, the PDFs of the small-scale fluctuations (inertial term and magnetic tension) have wide tails and even the large-scale

fluctuations of the magnetic field fluctuations are not approximately Gaussian.

The PDFs of the curvature of magnetic field lines and stream lines with a magnetic background field are linear for small values of the curvature and exhibit the same behaviour as the stream line curvature PDFs for high curvature values where the PDFs only follow a clear power law for very high curvature values. One might have expected a similar behaviour as for the curvature of Lagrangian trajectories in a boundary layer (Hengster et al., 2024) for the dataset with a magnetic background field where the power law of right tail vanishes and high curvature events are less likely but this is not the case here. While the ratio of the background field to the standard deviation is of the same order for the two cases with $\frac{U_\infty}{\sigma_{u_x}} \approx 12$, $\frac{B_0}{\sigma_{b_z}} \approx 13$, the curvature is calculated using the magnetic field fluctuations only. Therefore, the velocity and magnetic field fluctuations and the denominator stay of the same order across all datasets.

To take Reynolds number effects into account, we normalise using the standard deviation of the magnetic field fluctuations and magnetic tension for the curvature of magnetic field lines and the standard deviation of velocity fluctuations and the inertial term for the stream line curvature. For the curvature of the stream lines, we can derive the same scaling as for the curvature of the Lagrangian trajectories (eq.(4.2)):

$$\kappa_u \frac{\sigma_u^2}{\sigma_{\boldsymbol{u}\cdot\nabla\boldsymbol{u}}} \propto \kappa_u \frac{\sigma_u^2}{\varepsilon_u^{3/4}\nu^{-1/4}} \tag{5.3}$$

$$\propto \kappa_u \frac{\sigma_u^2 \nu^{3/4}}{(\varepsilon_u \nu)^{1/2}\varepsilon_u^{1/4}} \tag{5.4}$$

$$= \kappa_u Re_\lambda \eta_u \,. \tag{5.5}$$

In analogy, we define a measure for the curvature scaling of the magnetic field lines:

$$\kappa_b \frac{\sigma_b^2}{\sigma_{\boldsymbol{b}\cdot\nabla\boldsymbol{b}}} \propto \kappa_b \frac{\sigma_b^2}{\varepsilon_b^{3/4}\mu^{-1/4}} \tag{5.6}$$

$$= \kappa_b \frac{\sigma_b^2 \nu^{3/4}}{(\varepsilon_b \nu)^{1/2}\varepsilon_b^{1/4}} \tag{5.7}$$

$$\propto \kappa_u Rm\ \eta_b \tag{5.8}$$

where Rm is defined in analogy to the Taylor Reynolds number. It has been shown previously that re-scaling results in a master curve for the curvature PDF of Lagrangian tracer

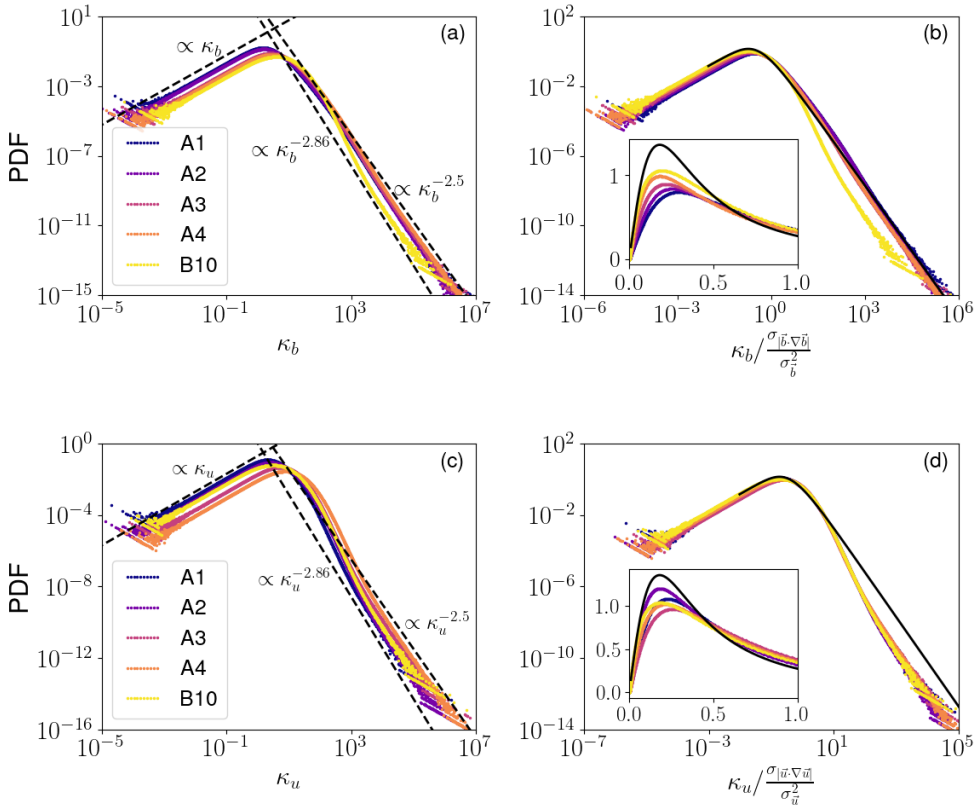

Figure 5.3: PDFs of the curvature of magnetic field lines (a) and stream lines (c), and normalised using the standard deviation of the magnetic field fluctuations and magnetic tension (b) and of the velocity fluctuations and inertial term (d) for the magnetic field lines and stream lines respectively on double logarithmic scales and linear scales in the inset. The colour gradient indicates the order of the datasets as presented in table 2.2. Reference lines based on the model predictions are shown in black in (a) and (c) and the PDF from the model by Xu et al. (2007), adapted for the curvature of magnetic field lines by Yang et al. (2019), (eq. (1.99)) in (b) and (d).

trajectories at different Reynolds numbers (Xu et al., 2007) and flow types (Hengster et al., 2024). For the magnetic field lines, we can see that the different PDFs with no magnetic background field indeed fall onto a master curve when taking Reynolds number equivalent Rm effects into account (fig. 5.3 (b)). The shape of the re-scaled PDFs compares well with model PDF of Xu et al. (2007) adapted by Yang et al. (2019) (black) but the peak is systematically overestimated by the model. However, the higher the Reynolds number is, the closer is the peak of the PDF to the peak of the model PDF (see inset of fig. 5.3 (b)). As we will see in the next chapter, the model for the curvature PDFs of Lagrangian trajectories can be improved by a decomposition in Gaussian sub-ensembles and we expect that, with the appropriate decomposition method, the model for the curvature PDF of the magnetic field lines can be improved further. The collapse onto a master curve also works for the left tail of the curvature PDF for the dataset with $B_0 = 10$ but for the right tail the PDF differs significantly from the model PDF as the shape is fundamentally different. The re-scaling of the curvature PDFs of the stream lines results in a master curve for all datasets (fig. 5.3 (d)). For small curvature values the master curve derived from data compares well with linear tail of the model PDF derived by Xu et al. (2007), but for high curvature values the two curves differ, caused by the different shape of the two curves. While for the magnetic field lines, there was a trend towards overestimation of the peaks, this is not the case for the stream line curvature. Generally, we can note that all peaks are closer to the peak of the model PDF for the curvature of the steam lines. To further investigate the effect of a magnetic background field on the geometry of magnetic field lines and stream lines, we will now focus on the statistics of the curvature vector.

5.4 Curvature Vector

The curvature vector in the Eulerian frame of reference is defined as:

$$\boldsymbol{\kappa}_b = \frac{\boldsymbol{b} \times (\boldsymbol{b} \cdot \nabla \boldsymbol{b})}{|\boldsymbol{b}|^3} \,.$$

This differs from the definition of the curvature vector in Schekochihin et al. (2001) by an additional cross product with $\hat{\boldsymbol{b}}$, while the definition in Schekochihin et al. (2001) is based on the definition of the curvature vector as the derivative of the tangent to a space curve

with respect to arc length. The definition of the curvature vector introduced here is parallel to the binormal vector and is perpendicular to the plane of a circle that approximates the curve locally. The curvature vector can be written as the ratio of the component of the magnetic tension force $\boldsymbol{f}_n = \hat{\boldsymbol{b}} \times \boldsymbol{b}\nabla\boldsymbol{b}$ orthogonal to the magnetic field and the strength of the magnetic field $|\boldsymbol{b}|^2$. The magnetic tension force is high when field lines are strongly bent (or curved). Therefore, smaller fluctuations in one direction lead to less curved field lines, resulting in a weaker tension force and therefore a smaller curvature in that direction. Smaller fluctuations in one direction can be caused by a strong magnetic background field that suppresses fluctuations parallel to the magnetic field, and therefore the curvature in that direction is expected to be smaller compared to the other two directions.

For simplicity, we compare the PDFs of the curvature vector components of datasets A4 with no magnetic background field (fig. 5.4 (a), (c)) and B10 with a magnetic background field where $B_0 = 10$ (fig. 5.4 (b), (d)). The curvature vector PDFs of the other datasets with no background field do not provide any additional insight with respect to the effect of anisotropy. For all curvature vector component PDFs, the left tail of the PDF is constant. This can be derived based on the assumption of Gaussian random variables (sec. 1.7.1). The right tail has the same power laws as seen for the curvature PDFs, that is an ≈ -2.5 power law for high curvature values of the magnetic field lines with no magnetic background field and for the other three cases for very high curvature values only. The effect of the background field can be seen by a quantitative comparison of the PDFs of the different components. While the curvature vector components PDFs of the dataset with no magnetic background field do not differ, the PDF of the z-component, parallel to the magnetic field, behaves differently to the PDFs of x- and y-components for the case with a magnetic background field. That is, the probability of small curvature is higher for the z-direction compared to the other two directions, resulting in magnetic field lines and stream lines being stretched along the z-axis. This can be related to the partial two-dimensionalisation of the magnetic field fluctuations, as outlined above (Alexakis, 2011; Gallet and Doering, 2015). Comparing the effect of the magnetic background field on the stream lines and magnetic field lines, we can see that the effect on the geometry of stream lines is less profound compared to the effect on the magnetic field lines.

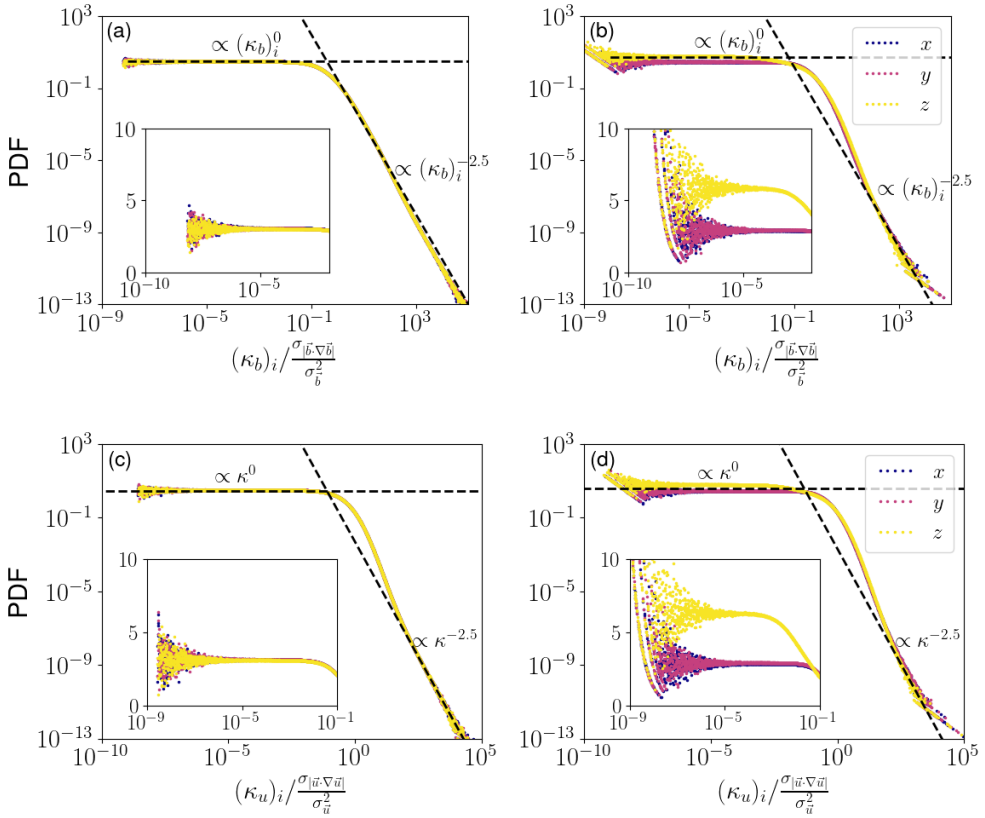

Figure 5.4: PDFs of the curvature vector components of magnetic field lines normalised using the standard deviation of the magnetic field fluctuations and magnetic tension on double logarithmic scales and semi-logarithmic scales in the inset of dataset A4 with no magnetic background field (a) and B10 with $B_0 = 10$ (b). In (c) and (d) the PDFs of the curvature vector components of the stream lines are shown for datasets A4 and B10 respectively. The dashed reference lines correspond to κ^0 and $\kappa^{-2.5}$.

5.5 Conclusions

In this chapter, we focused on the geometry of magnetic field lines and stream lines in MHD turbulence. While for the curvature of the Lagrangian trajectories the PDF of the curvature was clearly following a -2.5 power law for high curvature values, the power law for the curvature of magnetic field lines and stream lines cannot be determined exactly. The exponents of the power laws found here fluctuate between -2.86 and -2.5, which stem from the different models outlined in section 1.7.5. That agrees with previous works presented in section 1.7.4, where the power laws for different types of MHD data fluctuate between these two power laws.

Additionally, we analysed the impact of a magnetic background field on the geometry of stream lines and magnetic field lines by analysing the curvature vector statistics. The suppression of magnetic field fluctuations parallel to the magnetic field leads to less curved lines in that direction.

Chapter 6

Modelling of the Curvature PDF

This chapter presents the results from Hengster and Linkmann (2024) which is currently prepared for publication and provides additional analysis going beyond the scope of the paper. This work has also been presented at the GAMM Conference in 2022, the UK Fluids Conference in 2022, the European Fluid Mechanics conference in 2022, and the annual meeting of the APS DFD in 2022.

As part of chapter 4, the curvature PDFs of different flow types were discussed. We have compared the PDFs with models derived by Xu et al. (2007) for the experimental datasets and by Xu et al. (2007) and Schekochihin et al. (2001) for the numerical datasets. While for both types of data these models give a good approximation of the shape of the PDF, the peak is overestimated by $\approx 30\%$. The models are based on Gaussian statistics and do not take spatio-temporal intermittency into account. Here, I will cover a derivation of a model for the curvature PDF for von Kármán flow and Rayleigh-Bénard convection at the higher Rayleigh number (RBC II).

The model is based on a decomposition of the full ensemble into Gaussian sub-ensembles presented in Bentkamp et al. (2019). The authors showed that for DNS of homogeneous and isotropic turbulence the full ensemble can be split into sub-ensembles, where the acceleration PDFs are Gaussian by conditioning on the coarse-grained acceleration:

$$\alpha(t) = \int_{-\infty}^{\infty} d\tau G_\Theta(\tau) |\boldsymbol{a}^2(t+\tau)| \tag{6.1}$$

where $G_\Theta(\tau) = \frac{1}{\sqrt{2\pi\Theta^2}} e^{-\frac{\tau^2}{2\Theta^2}}$ is a Gaussian filter kernel with standard deviation Θ. Each

sub-ensemble is made up of trajectory parts where the coarse-grained acceleration of this part is in a predefined bin of the coarse-grained acceleration. The numerical set up of this is described in section 3.1.2. In total, 17 sub-ensembles are created, with the values being log-spaced between $0.003\langle\alpha\rangle$ and $54\langle\alpha\rangle$. The coarse-grained acceleration, also known as persistent acceleration, tends to be higher in regions with high levels of turbulence and lower in regions with less turbulence present. Therefore, by dividing the full ensemble into sub-ensembles conditioned on the coarse-grained acceleration, the data gets split into parts, where the flow tends to be more turbulent and less turbulent, and by that this method takes spatio-temporal intermittency into account. This concept is inspired by the Eulerian refined similarity hypothesis (Kolmogorov, 1962; Oboukhov, 1962), where the coarse-grained dissipation rate can be used to split full ensembles into simpler sub-ensembles. A difference to note is that the Eulerian filter scale used for the coarse-graining usually varies while for the Lagrangian approach used here this is a fixed filter scale (Homann et al., 2011).

Here, we first check if the decomposition method of Bentkamp et al. (2019) works for experimental data of weakly anisotropic flows, namely von Kármán flow and Rayleigh-Bénard convection. As we will see in the next section, the decomposition method works for the two datasets. Based on the model for the curvature PDF of Xu et al. (2007) and the decomposition, we derive an exact model expression and a closed-form approximation for the curvature PDF for the full ensemble.

The following sections will give an overview of the decomposition method, explain the derivation of the curvature PDF model and provide a comparison of the model with data. I will conclude with an outlook on how this model can be adapted for the curvature PDF of magnetic field lines and stream lines.

6.1 Velocity and Acceleration Statistics

In the first step, we will apply the decomposition method of Bentkamp et al. (2019) to experimental data of turbulent von Kármán flow and Rayleigh-Bénard convection and discuss the PDFs of velocity and acceleration components in the sub-ensembles. In chapter 4, we have seen that the PDFs of the velocity components for the full ensemble are near Gaussian. Therefore, it can be expected that this is also the case for the PDFs in the sub-ensembles.

	von Kármán	RBC II
β	0.15 ± 0.01	0.24 ± 0.05
γ	0.99 ± 0.02	1.09 ± 0.04

Table 6.1: Exponents for the scaling of the variance of velocity $\langle u^2 \rangle \propto \alpha^{\beta}$ and the acceleration $\langle a^2 \rangle \propto \alpha^{\gamma}$.

In figure 6.1 we can see that this is indeed the case for both flow types. This can also be further validated by the first four statistical moments (fig. 6.2), where the reference lines for the mean, skewness, and flatness for a Gaussian are shown. For the von Kármán flow (left column), we can see some significant deviations from the Gaussian values in the sub-ensembles where α is small. While for the first ones and the last ones, this might stem from a convergence issue (see the PDF of α in fig. 6.5), the first seven sub-ensembles are in the core of the PDF. A potential reason for that might be that these deviations are related to the anisotropy of the flow, caused by the propeller motion (Voth et al., 2002) and as discussed in section 1.6.1. For the Rayleigh-Bénard convection (right column), the deviations in the moments can most likely be connected to the convergence of the PDFs. For the further analysis, we decided to exclude the sub-ensembles that deviate significantly from a Gaussian, which are indicated by a grey markers in figures 6.2, 6.4, 6.5, and only show the PDFs in the remaining sub-ensembles. While the mean, skewness, and flatness are constant, the variance is increasing $\propto \alpha^{\beta}$. For von Kármán flow we found that $\langle u^2 | \alpha \rangle \propto \alpha^{0.14}$ and for Rayleigh-Bénard convection the variance scales $\propto \alpha^{0.24}$ (table 6.1).

In figure 6.3, we can see that, while the full PDF is far from a Gaussian with wide tails (red), the PDFs in the sub-ensembles are near Gaussian (blue). To examine and characterise the PDFs in the sub-ensembles in more detail, we calculate the first four moments of the acceleration components shown in figure 6.4 for von Kármán flow (left column) and Rayleigh-Bénard convection (right column). Firstly, we can observe that the mean fluctuates around zero and that the fluctuations are smaller for the acceleration components than for the velocity components. The deviations from zero increase with increasing α for both flow types. For the skewness of the acceleration components, the range of fluctuations is also smaller than for the skewness of the velocity components and close to zero, as expected for a Gaussian distribution. The fluctuations of the flatness are around three, which is the expected flatness value for a Gaussian, where the order of the fluctuations is the same for

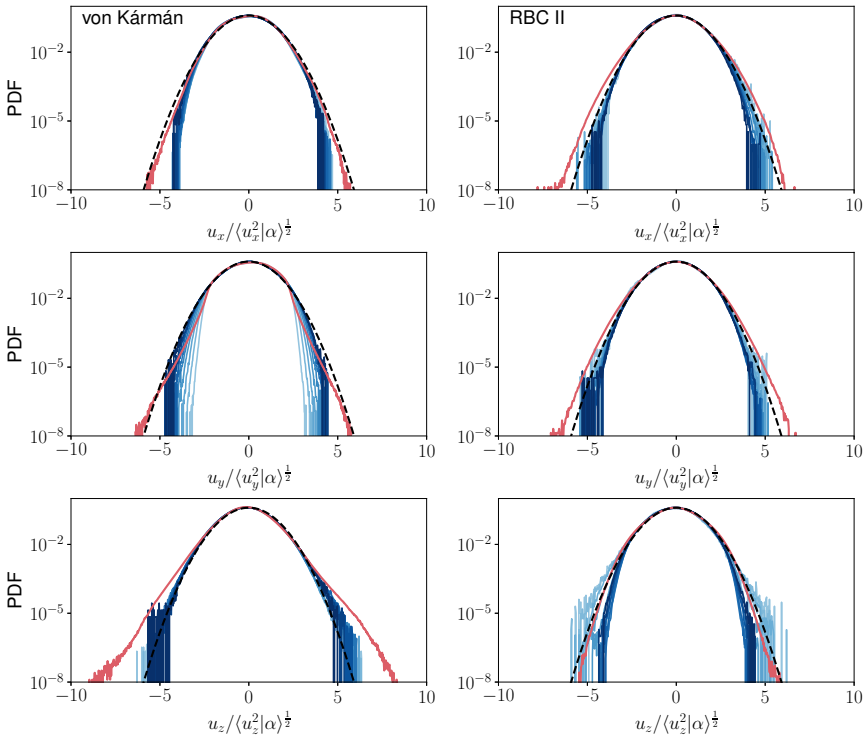

Figure 6.1: PDFs of velocity components, conditioned on the coarse-grained acceleration for von Kármán flow (left) and RBC II(right). The colour gradient indicates increasing α from light to dark blue. The PDF of the full ensemble is shown in red and the dashed line is a Gaussian with zero mean and standard deviation of unity.

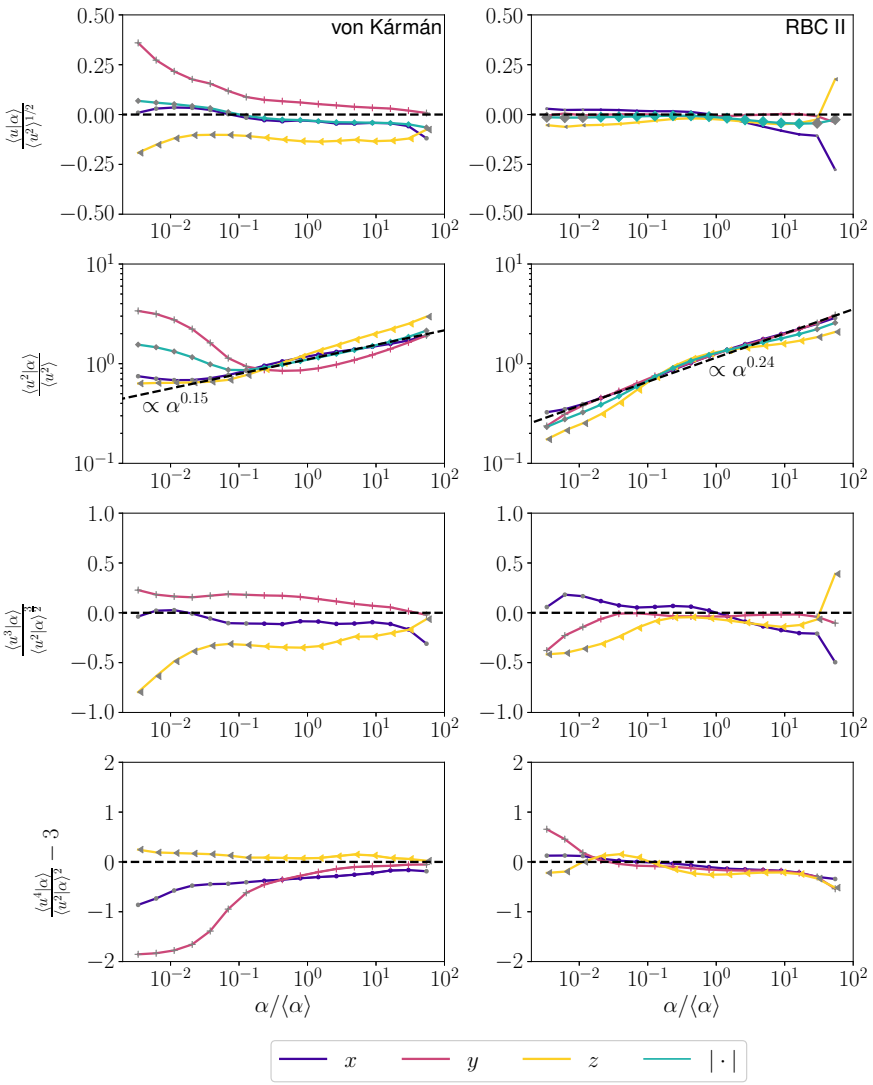

Figure 6.2: First four (from top to bottom: mean, variance, skewness and flatness) statistical moments of the velocity components and of the magnitude for mean and variance in the sub-ensembles as a function of the bin centres of the sub-ensembles. In the left column, the moments for von Kármán flow are shown, in the right column for RBC II.

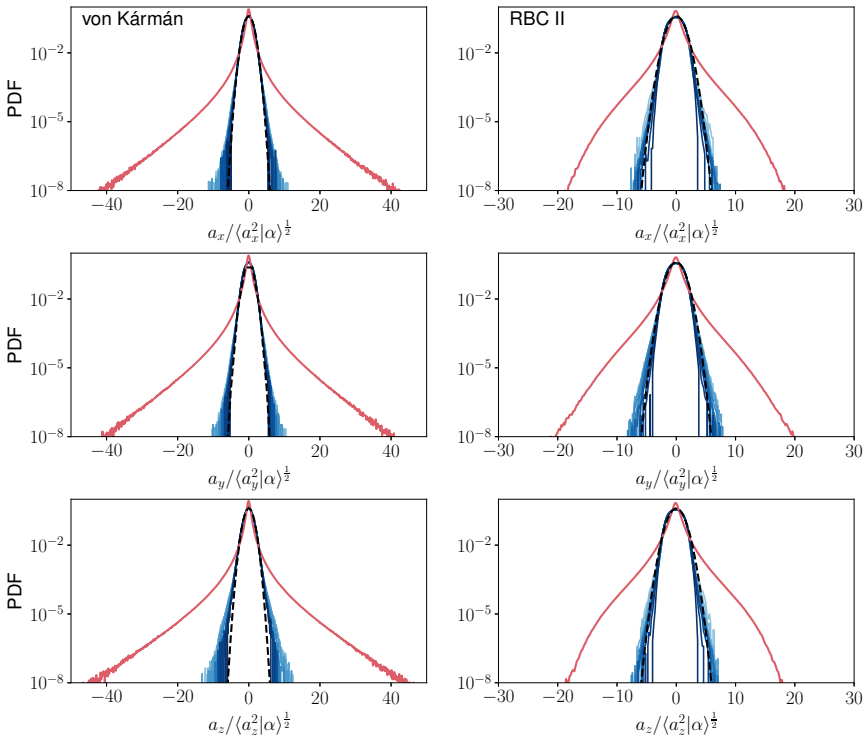

Figure 6.3: PDFs of acceleration components, conditioned on the coarse grained acceleration for von Kármán flow (left) and RBC (right). The colour gradient indicates increasing α from light to dark blue. The PDF of the full ensemble is shown in red and the dashed line is a Gaussian with zero mean and standard deviation of unity.

velocity and acceleration. However, it should be noted that the flatness of the acceleration components of the full ensemble is ≈ 35 for von Kármán flow and ≈ 14 for Rayleigh-Bénard convection (RBC) while the flatness values for the full ensemble of the velocity are around 3. For the variance, Bentkamp et al. (2019) found a linear scaling of the variance as a function of α. For the von Kármán flow, we found that the variance scales $\propto \alpha^{0.99}$, while for RBC $\langle a^2|\alpha\rangle \propto \alpha^{1.09}$, which agrees well with the findings of Bentkamp et al. (2019) for numerical simulations of homogeneous and isotropic turbulence. For both datasets, the level of anisotropy is much smaller for the acceleration compared to the velocity.

6.2 Coarse-Grained Acceleration

As outlined above, Bentkamp et al. (2019) introduced a technique to divide the full ensemble of Lagrangian trajectories into sub-ensembles where the PDFs of the acceleration components are almost Gaussian. This is done by conditioning on the coarse-grained acceleration α (eq. (6.1)). The PDFs of the coarse-grained acceleration using $\Theta = 3\,\tau_\eta$ as filter width

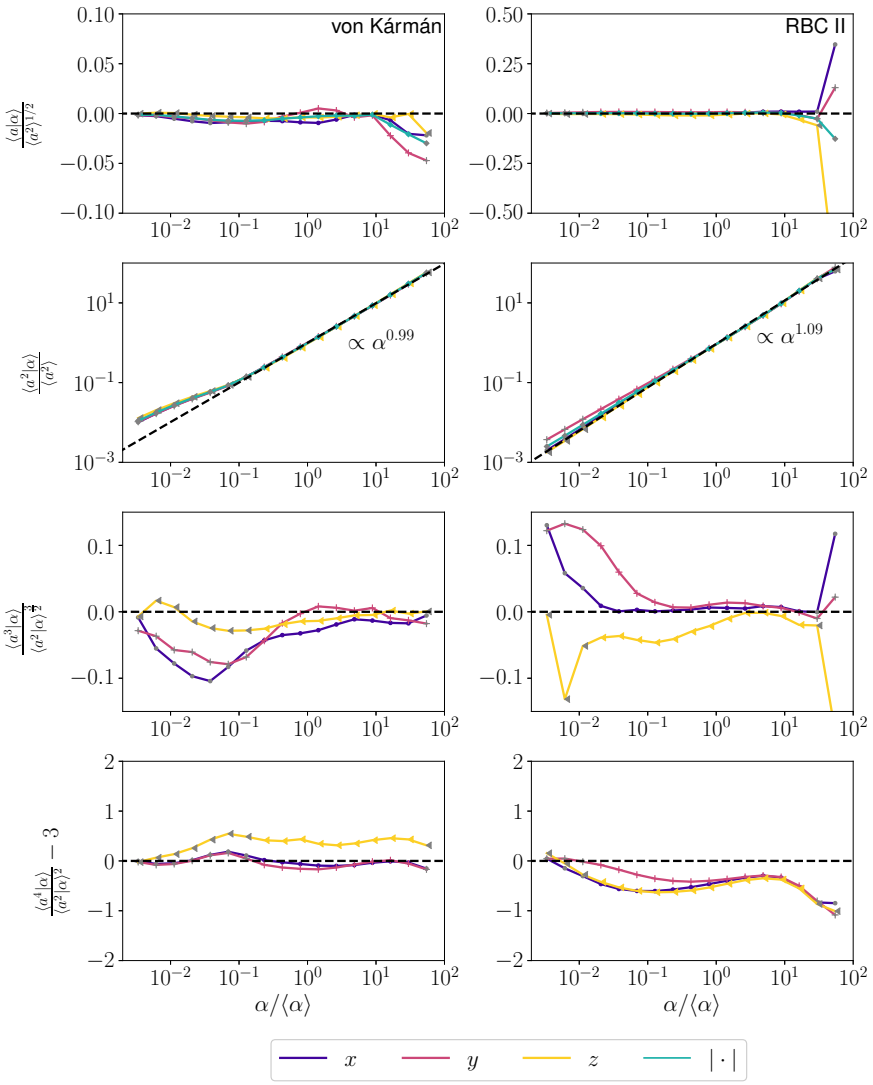

Figure 6.4: First four (from top to bottom: mean, variance, skewness and flatness) statistical moments of the acceleration components and magnitude for mean and variance in the sub-ensembles as a function of the bin centres of the sub-ensembles. In the left column, the moments for von Kármán flow are shown, in the right column for RBC II.

are shown in figure 6.5. For both von Kármán flow and RBC II, we fitted a log-normal distribution

$$f(x) = \frac{1}{x\sigma\sqrt{2\pi}} \exp\left(-\frac{(\ln(x)-\mu)^2}{2\sigma^2}\right) \tag{6.2}$$

with μ being the mean and σ the standard deviation of $\ln(x)$. The fitted parameters for the two datasets can be found in table 6.2. For both datasets the left tail of the PDFs is overestimated by the fit while the core is captured well. For the right tail the fit works better for the RBC dataset compared to the von Kármán flow. The PDF of the von Kármán

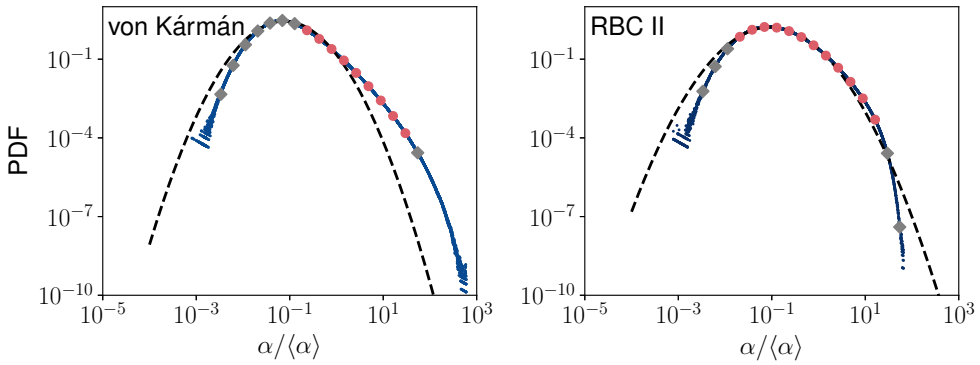

Figure 6.5: PDFs of the coarse grained acceleration α for von Kármán flow (left) and RBC II(right). The markers indicate the bin centres of the sub-ensembles, in red circles when considered for further analysis, in grey diamonds if neglected. A reasoning for that can be found in the text.

	von Kármán	RBC II
μ	-1.45 $\pm$ 0.15	-0.90 $\pm$ 0.10
σ	1.06 $\pm$ 0.11	1.20 $\pm$ 0.07

Table 6.2: Fitting parameters of the log-normal distribution for the PDFs of the coarse-grained acceleration.

flow has a more profound right tail compared to the fit. This shows that in von Kármán flow we can expect more extreme events of the coarse-grained acceleration compared to the Rayleigh-Bénard convection. The markers on the PDFs show the bin centres of the sub-ensembles that will be analysed in the following. We decided to fit log-normal distributions to compare our results with the results in Bentkamp et al. (2019) where good agreement for the right tail was found. Here, we find good agreement for RBC but for von Kármán flow the right tail is underestimated by the fit. We altered the filter range to improve the fitting of the right tail but that resulted in an extreme overestimation of the left tail. We found that the provided fit delivered the best results in the modelling of the curvature PDF.

6.3 Model for the Curvature PDF of Lagrangian Trajectories

As briefly outlined in section 1.7.5, a model for the curvature PDF can be derived under the assumption that velocity and acceleration components are independent Gaussian random variables (Xu et al., 2007). In the previous section, we have seen that the velocity and acceleration components have Gaussian PDFs in the sub-ensembles. In section 6.3.1 we will see

that the velocity and acceleration components in the sub-ensembles can be approximated as independent. The curvature is defined as $\kappa = |\boldsymbol{a}_n|/|\boldsymbol{u}|^2$. As this is a product of approximately independent variables in each sub-ensemble, we can derive an equation for the PDF of the product of $|\boldsymbol{a}_n|$ and $1/|\boldsymbol{u}|^2$. The cumulative distribution of the random variable $\kappa = a_n \cdot 1/u^2$ is given by:

$$\begin{aligned}
F_\kappa(x_\kappa) =& F(K \leq x_\kappa) = F(a_n \cdot 1/u^2 \leq x_\kappa) \\
=& F(a_n \cdot 1/u^2 \leq x_\kappa, a_n \geq 0) + F(a_n \cdot 1/u^2 \leq x_\kappa, a_n \leq 0) \\
=& F(1/u^2 \leq x_\kappa/a_n, a_n \geq 0) + F(1/u^2 \leq x_\kappa/a_n, a_n \leq 0) \\
=& \int_0^\infty P_{a_n}(x_{a_n}) \int_{-\infty}^{x_\kappa/x_{a_n}} P_{1/u^2}(x_{1/u^2}) d(x_{1/u^2}) dx_{a_n} \\
&+ \int_{-\infty}^0 P_{a_n}(x_{a_n}) \int_{x_\kappa/x_{a_n}}^\infty P_{1/u^2}(x_{1/u^2}) d(x_{1/u^2}) dx_{a_n} .
\end{aligned}$$

The PDF of κ is given by $\frac{d}{dx_\kappa} F_\kappa(x_\kappa)$:

$$\begin{aligned}
\frac{d}{dx_\kappa} F_\kappa(x_\kappa) =& P_\kappa(x_\kappa) && (6.3)\\
=& \frac{d}{dx_\kappa} \int_0^\infty P_{a_n}(x_{a_n}) \int_{-\infty}^{x_\kappa/x_{a_n}} P_{1/u^2}(x_{1/u^2}) d(x_{1/u^2}) dx_{a_n} && (6.4)\\
&+ \frac{d}{dx_\kappa} \int_{-\infty}^0 P_{a_n}(x_{a_n}) \int_{x_\kappa/x_{a_n}}^\infty P_{1/u^2}(x_{1/u^2}) dx_{1/u^2} dx_{a_n} && (6.5)\\
=& \int_0^\infty P_{a_n}(x_{a_n}) \frac{d}{dx_\kappa} \int_{-\infty}^{x_\kappa/x_{a_n}} P_{1/u^2}(x_{1/u^2}) dx_{1/u^2} dx_{a_n} && (6.6)\\
&+ \int_{-\infty}^0 P_{a_n}(x_{a_n}) \frac{d}{dx_\kappa} \int_{x_\kappa/x_{a_n}}^\infty P_{1/u^2}(x_{1/u^2}) dx_{1/u^2} dx_{a_n} && (6.7)\\
=& \int_0^\infty P_{a_n}(x_{a_n}) \frac{1}{x_{a_n}} P_{1/u^2}(x_\kappa/x_{a_n}) dx_{a_n} - \int_{-\infty}^0 P_{a_n}(x_{a_n}) \frac{1}{x_{a_n}} P_{1/u^2}(x_\kappa/x_{a_n}) dx_{a_n} && (6.8)\\
& \int_0^\infty P_{a_n}(x_{a_n}) \frac{1}{|x_{a_n}|} P_{1/u^2}(x_\kappa/x_{a_n}) dx_{a_n} + \int_{-\infty}^0 P_{a_n}(x_{a_n}) \frac{1}{|x_{a_n}|} P_{1/u^2}(x_\kappa/x_{a_n}) dx_{a_n} && (6.9)\\
=& \int_{-\infty}^\infty P_{a_n}(x_{a_n}) \frac{1}{|x_{a_n}|} P_{1/u^2}(x_\kappa/x_{a_n}) dx_{a_n} . && (6.10)
\end{aligned}$$

To derive the curvature PDF, we therefore need the PDF of a_n and $1/u^2$. As acceleration and velocity components are approximately Gaussian variables in each sub-ensemble, the PDF of

$1/u^2$ is given by the inverse χ^2-distribution of order three:

$$P_{1/u^2}(x) = \frac{2^{-3/2}}{\Gamma(3/2)} x^{3/2-1} e^{(-1/(2x))} \tag{6.11}$$

where $\Gamma(\cdot)$ is the gamma function. The PDF of a_n can be approximated by a χ-distribution of order two:

$$P_{a_n}(x) = \begin{cases} x e^{-x^2/2}, & x \geq 0; \\ 0, & \text{otherwise.} \end{cases} \tag{6.12}$$

For isotropic turbulence (and weak levels of anisotropy) the normal acceleration can be approximated by two arbitrary components, for example x and y: $a_n = \sqrt{a_x^2 + a_y^2}$. Using these PDFs for the velocity and acceleration under the assumption that these are independent random variables, we can use equation (6.10) to derive the PDF of the non-dimensionalised curvature x_κ:

$$P_\kappa(x_\kappa) = \int_{-\infty}^{\infty} P_{a_n}(x_{a_n}) \frac{1}{|x_{a_n}|} P_{1/u^2}(x_\kappa / x_{a_n}) dx_{a_n} \tag{6.13}$$

$$= \int_0^{\infty} x_{a_n} e^{-x_{a_n}^2/2} \frac{1}{|x_{a_n}|} \frac{2^{-3/2}}{\Gamma(3/2)} (x_\kappa / x_{a_n})^{1/2} e^{-\frac{1}{2}\ (x_{a_n}/x_\kappa)} dx_{a_n} \tag{6.14}$$

$$= \frac{e^{x_\kappa^{-2}/16}}{16\sqrt{2\pi} x_\kappa^4} \left(\left(3 + \frac{1}{2x_\kappa^2} \right) K_{3/4}\left(\frac{1}{16x_\kappa^2} \right) \left(5 + \frac{1}{2x_\kappa^2} \right) K_{1/4}\left(\frac{1}{16x_\kappa^2} \right) \right) , \tag{6.15}$$

where $K_{1/4}$ and $K_{3/4}$ are modified Bessel functions of the second kind. This is the equation for the non-dimensionalised curvature PDF in a sub-ensemble, and therefore the notation will change to $P(x_\alpha)$ from here. The PDFs are non-dimensionalised using the variance $\langle |\boldsymbol{u}|^2 | \alpha \rangle = \left(\sigma_u^{(\alpha)} \right)^2$ and standard deviation $\langle |\boldsymbol{a}|^2 | \alpha \rangle^{1/2} = \sigma_a^{(\alpha)}$, non-dimensionalised using the mean of α:

$$\kappa \frac{\left(\sigma_u^{(\alpha)} \right)^2}{\sigma_a^{(\alpha)}} \propto \kappa \frac{\sigma_u^2}{\sigma_a} \frac{\alpha^{-\zeta}}{\langle \alpha \rangle^{-\zeta}} := x_\alpha \tag{6.16}$$

where σ_u and σ_a are the standard deviation of the full ensemble. The exponent ζ can be estimated from the scaling of the variances of the velocity and acceleration (table 6.1, figs 6.2 and 6.4):

$$x_\alpha \propto \frac{\left(\sigma_u^{(\alpha)} \right)^2}{\sigma_a^{(\alpha)}} \propto \frac{\alpha^\beta}{\alpha^{\gamma/2}} = \alpha^{-(\gamma/2-\beta)} := \alpha^{-\zeta} ,$$

for von Kármán flow, we get $\zeta = 0.35 \pm 0.03$ and for RBC $\zeta = 0.31 \pm 0.05$. Xu et al. (2007) suggested equation (6.15) as the PDF of the full curvature but this is not taking the effect of intermittency into account. With the presented decomposition, we are able to take spatio-temporal intermittency into account and derive a closed form expression for the curvature PDF for the full ensemble. For that, we use x_α as defined in equation (6.16) as a random variable for each sub-ensemble. As $\alpha \geq 0$, the set of possible α can be interpreted as an index set A, which leads to a formal definition of a stochastic process: $X : \alpha \mapsto x_\alpha$. This allows us to approximate the PDF of κ with the PDF for the expected value of X with respect to α. The relation between the curvature and the expected value of X is given by:

$$\langle X \rangle = \int_0^\infty d\alpha f(\alpha) x_\alpha = \kappa \frac{\sigma_u^2}{\sigma_a} \frac{\langle \alpha^{-\zeta} \rangle}{\langle \alpha \rangle^{-\zeta}} \tag{6.17}$$

where the PDF of the coarse-grained acceleration is given by $f(\alpha)$. Given that the set of x_α represents independent and identically distributed random variables, we can choose a value $\alpha^* \in A$, such that $(\alpha^*) = \langle \alpha^{-\zeta} \rangle$. This allows us to derive a formula for the curvature PDF $P_K(\kappa)$:

$$P_K(\kappa) = P_K \left(\frac{\sigma_a}{\sigma_u^2} \frac{\langle \alpha \rangle^{-\zeta}}{\langle \alpha^{-\zeta} \rangle} \langle X \rangle_\alpha \right) \tag{6.18}$$

$$= \frac{\sigma_u^2}{\sigma_a} \frac{\langle \alpha^{-\zeta} \rangle}{\langle \alpha \rangle^{-\zeta}} P(\langle X \rangle) \tag{6.19}$$

$$= \frac{\sigma_u^2}{\sigma_a} \frac{\langle \alpha^{-\zeta} \rangle}{\langle \alpha \rangle^{-\zeta}} P(x_{\alpha^*}) \ , \tag{6.20}$$

with $P(x_{\alpha^*})$ the PDF of the non-dimensionalised curvature in a sub-ensemble x_{α^*} given by equation (6.15). As an alternative approach, it is also possible to derive the full curvature PDF by using the law of total probability:

$$P_\kappa(\kappa) = \int d\alpha f(\alpha) P_\alpha(\kappa_\alpha) = \int d\alpha f(\alpha) c(\alpha) P(x_\alpha) \tag{6.21}$$

where $P_\alpha(\kappa_\alpha)$ the curvature PDF in a sub-ensemble α and $P_\alpha(\kappa_\alpha) = P(x_\alpha) c(\alpha)$ where $c(\alpha)$ is a non-dimensionalisation of the curvature. The PDF of the coarse-grained acceleration can either be obtained from data or from the log-normal fit with the parameters presented in table 6.2.

6.3.1 Validation of Model Assumptions

To derive the model for the curvature PDF, one of the main assumptions is that the velocity and acceleration components are independent. This is generally not true as shown by calculations of PDF quotients in Mordant, Crawford and Bodenschatz (2004). For two acceleration components, the PDF quotient is given by:

$$\frac{P(a_i, a_j)}{P(a_i)P(a_j)} \,. \tag{6.22}$$

We therefore calculated the PDF quotients for all combinations of components for the full ensemble and different sub-ensembles. For simplicity only the quotients of a subset of component combinations for one sub-ensemble are shown (see fig. 6.6 for von Kármán flow and fig. 6.7 for RBC II). Across both datasets and for the different component combinations, we can see that the full ensemble has some clear dependencies, highlighted by areas where the quotient is not one. When restricting the calculations to a sub-ensemble, these dependencies become much weaker, specifically in the core of the PDFs.

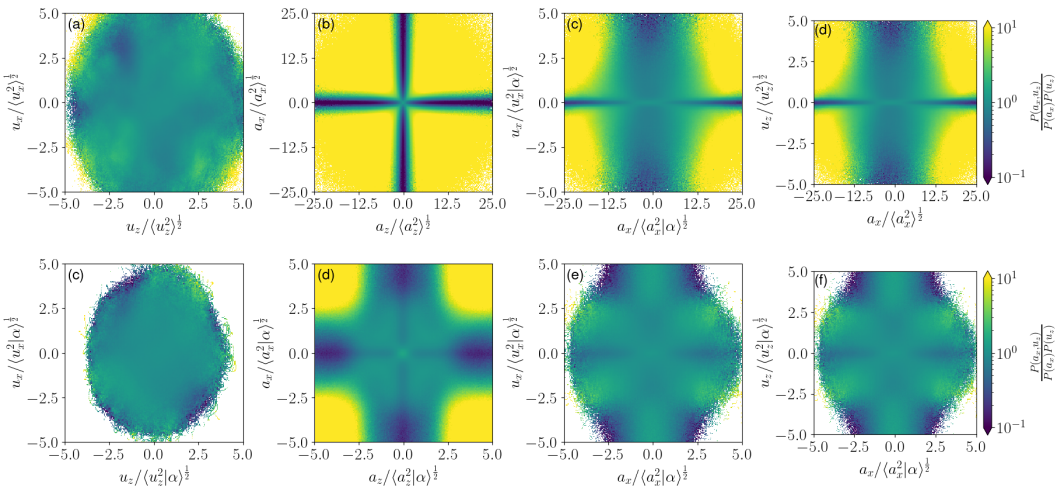

Figure 6.6: PDF quotients for different velocity and acceleration components in the full ensemble (top row) and in sub-ensemble $\alpha = 2.64\langle\alpha\rangle$ (bottom row) for von Kármán flow.

In figure 6.8 the quotient PDFs of three the sub-ensembles ($\alpha = 0.23\langle\alpha\rangle$, $\alpha = 2.64\langle\alpha\rangle$ and $\alpha = 29.7\langle\alpha\rangle$) are shown. It is not possible to define a clear trend between the dependence and the coarse-grained acceleration. It becomes clear that the assumption of independence works differently well in the different sub-ensembles and should be kept in mind when applying

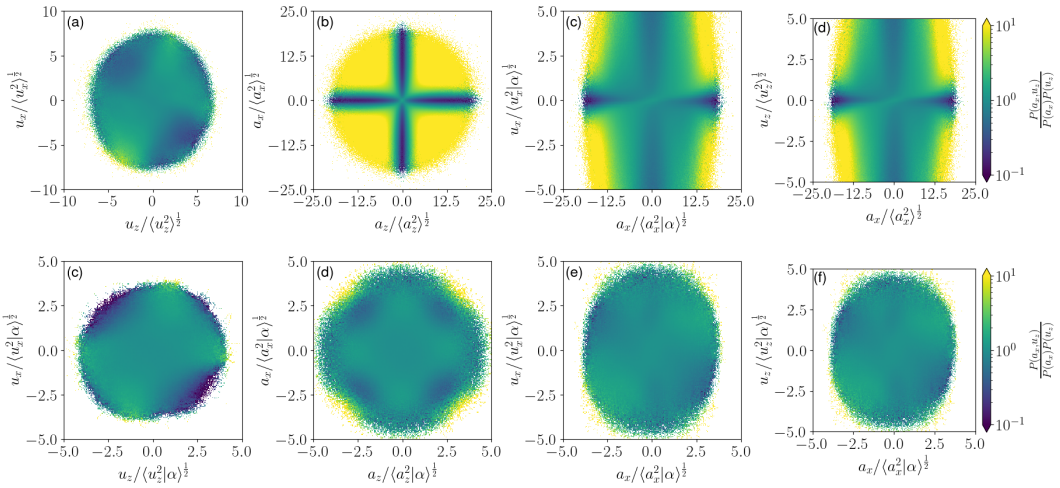

Figure 6.7: PDF quotients for different velocity and acceleration components in the full ensemble (top row) and in sub-ensemble $\alpha = 2.64\langle\alpha\rangle$ (bottom row) for Rayleigh-Bénard convection.

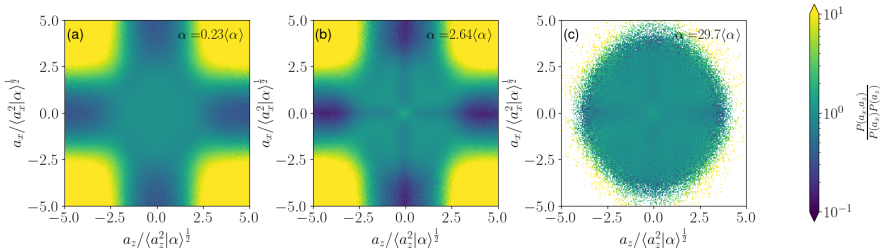

Figure 6.8: PDF quotients for two acceleration components in different sub-ensembles $\alpha = 0.23\langle\alpha\rangle,\ 2.64\langle\alpha\rangle,\ 29.7\langle\alpha\rangle$ for von Kármán flow.

the model of the curvature PDF to the data. Overall, we can see a decrease of dependence compared to the full ensemble. Therefore, we expect the effect of the dependence to be smaller in the derived model PDF for the curvature compared to the model by Xu et al. (2007) for the full ensemble. To further reduce these dependencies, the sub-ensembles could be created over a smaller range, for example 2% rather than the 5% used here.

6.3.2 Comparison of Model and Data

We can now compare the results from the derived model PDFs with the curvature PDF obtained from data. In the top row of figure 6.9, the curvature PDFs in the sub-ensembles for the two datasets are presented. For both datasets the tails of the PDFs are the same as for the full curvature PDF and as predicted by the model from Xu et al. (2007). The

PDFs are shifted towards higher curvature values with the increase of the coarse-grained acceleration, indicating that trajectories tend to be more curved in more turbulent regions of the flow. Using the proposed re-scaling (eq. (6.16)), the PDFs collapse onto a master curve (fig. 6.9 bottom row). This master curve agrees well with the PDF derived based on Gaussian random variables for the velocity and acceleration components (eq. (6.15), shown in red).

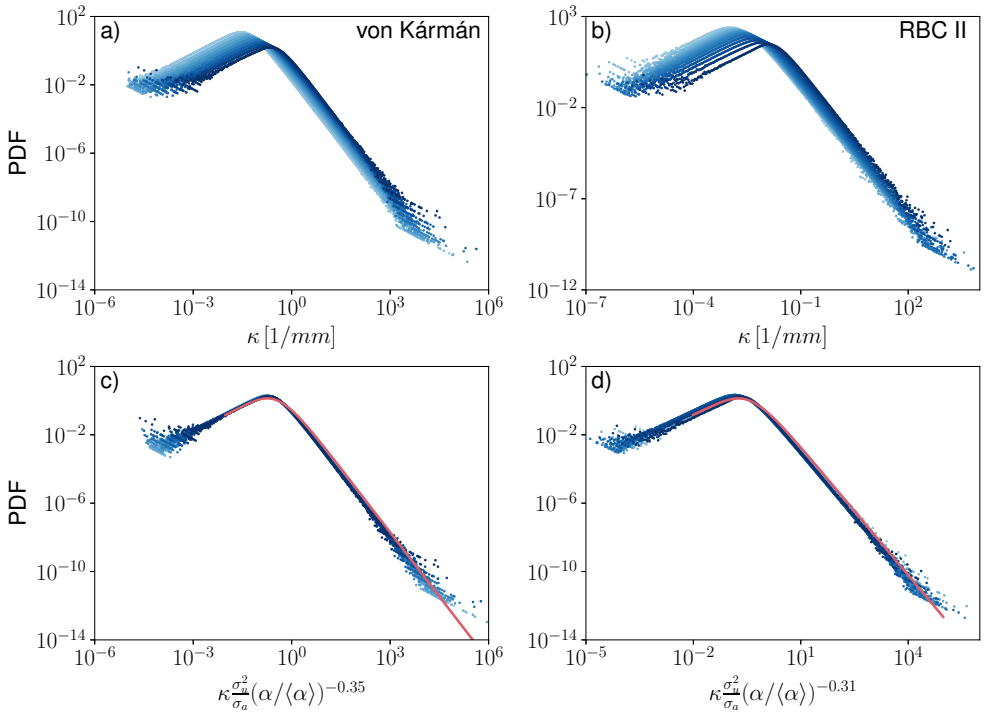

Figure 6.9: Curvature PDFs (top row) in the sub-ensembles for von Kármán flow (left) and Rayleigh-Bénard convection (right) and non-dimensionalised curvature PDFs (bottom row) using equation (6.16) and a comparison with the model PDF based on Gaussian random variables (eq. (6.15)) shown in red. The value of α increases from light to dark blue.

We can now compare the PDFs of the non-dimensionalised curvature for the full ensembles obtained from data and the model PDFs (fig. 6.10) for both datasets. The curvature PDF obtained from data is shown in black. The model PDF (eq. (6.20), blue) overestimates the peak for both datasets while the PDFs derived from the law of total probability underestimate the peak slightly. For both datasets these differences are less than 5%. The differences might be caused by the differences between the non-dimensionalised curvature PDFs in the sub-ensembles and the analytic curve (fig. 6.9), the uncertainty of the exponent ζ (table 6.1) or the deviations of the log-normal fit to the PDF of the coarse-grained accel-

eration (fig. 6.5). Interestingly, the PDFs derived using the log-normal fit for the PDF of α result in a PDF closer to the PDF obtained from data. Overall, we can see that for both datasets, agreement is good between model, theory, and data and all model PDFs presented here are an improvement of the model presented by Xu et al. (2007), where the peak was underestimated by $\approx 30\%$.

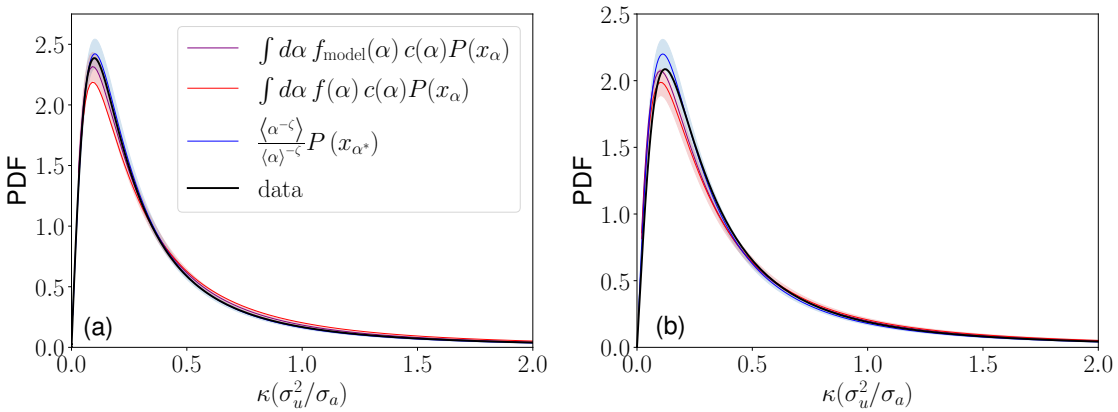

Figure 6.10: Curvature PDFs non-dimensionalised using the global velocity and acceleration standard deviations for von Kármán flow (a) and RBC II (b) obtained from data (black) compared with PDFs obtained by the law of total probability using the log-normal fit for the PDF of the coarse-grained acceleration (purple) and the α-PDF obtained from data (red) and the model PDF (eq. (6.20), blue). The shaded areas refer to 5% uncertainty.

6.4 Model for the Curvature PDF of Magnetic Field Lines and Stream Lines

This section will give an overview of how the model described above could be adapted for magnetic field lines and stream lines in magnetohydrodynamic turbulence. This is part of the project in collaboration with Michael Wilczek based on the work described in chapter 5. The analysis is exploratory and still work in progress but I will explain the basic concepts of the idea behind the model and present the first preliminary results. As we have seen in chapter 5, the model PDF by Xu et al. (2007), adapted by Yang et al. (2019) for stream lines and magnetic field lines, gives a good approximation on the curvature PDF of both stream lines and magnetic field lines but the assumptions for the model, that the components of velocity and inertia term and magnetic field and magnetic tension are independent Gaussian variables, are not fulfilled. This has been shown in Seta et al. (2020) for the magnetic field fluctuations

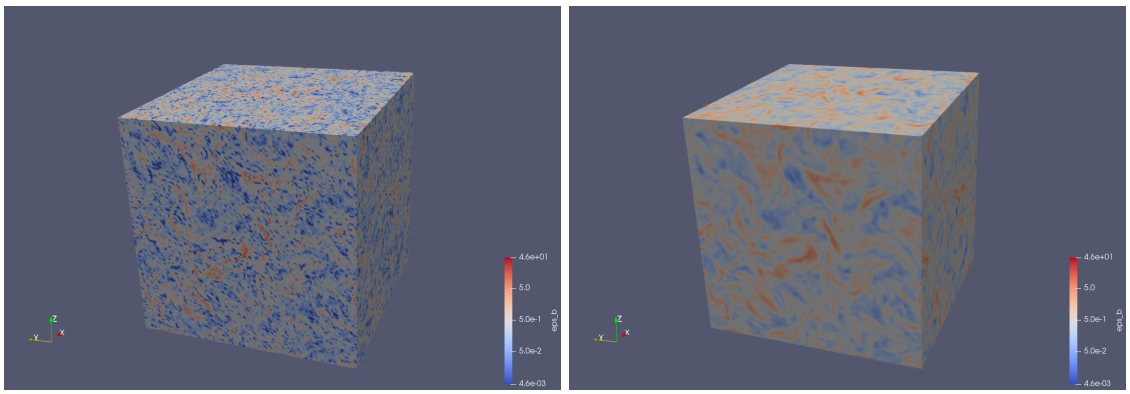

Figure 6.11: Visualisation of the magnetic dissipation rate ε_b (left) and of the magnetic coarse-grained dissipation rate for $L = 10\eta$ (right) for an example snapshot of the A1 dataset on a log-scale. Coarse-graining leads to a more homogeneous field with less sharp gradients.

and in chapter 5 for the magnetic field fluctuations, magnetic tension and inertial term. In analogy to the model for the curvature PDF of Lagrangian trajectories, we attempted to find a decomposition method that splits the full ensemble into Gaussian sub-ensembles. Homann et al. (2011) showed that by conditioning the velocity increments $\delta_L^{\parallel} u$ on the dissipation rate coarse-grained over length scale L, the PDFs of the velocity increments are near Gaussian. Here, we used the coarse-grained dissipation rate:

$$\varepsilon_L(\boldsymbol{x}) = \int d^3 r G_L(\boldsymbol{r}) \varepsilon(\boldsymbol{x} + \boldsymbol{r}), \tag{6.23}$$

where ε can be the velocity or magnetic dissipation rate. In figure 6.11, a visualisation of the effect of coarse-graining can be seen where we show the unfiltered dissipation rate ε_b in the left subfigure and in the right subfigure dissipation rate coarse-grained over length scale $L = 10\eta$. Generally, we see less extreme events when the dissipation rate is coarse-grained, which can also be seen in the PDFs of the coarse-grained dissipation rate when coarse-grained over different length scales (fig. 6.12).

In figure 6.13, the PDFs of the magnetic field fluctuations and magnetic tension components for the full ensemble and sub-ensembles are shown. For both observables, the PDFs are not statistically converged, and therefore it is not clear if this decomposition method would work. We also calculated the PDFs in the sub-ensembles which seem to be more converged. However, the shape, specifically the right tail, of these PDFs differs between the different sub-ensembles, indicating that we might have chosen the wrong variable for the

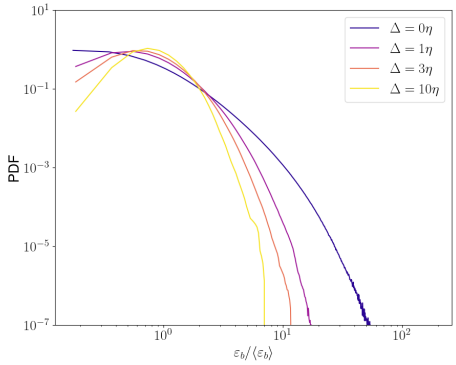

Figure 6.12: PDF of coarse-grained dissipation rate for different length scales $L = 0$, 1η, 3η, 10η. With increasing coarse-graining scales, extreme events become less likely.

decomposition. Potential future steps would include to create sub-ensembles by conditioning on the coarse-grained magnetic tension, which would be more in analogy to the conditioning on the coarse-grained acceleration for the Lagrangian trajectories.

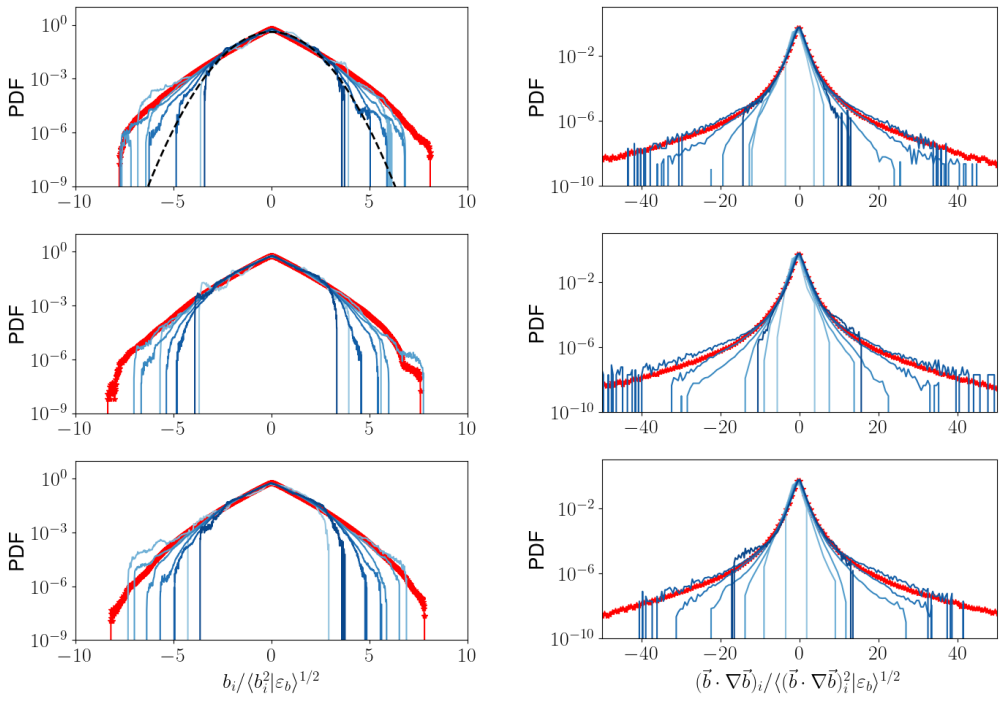

Figure 6.13: PDFs of the magnetic field fluctuations (left) and components of the magnetic tension (right) for the full ensemble shown in red and in sub-ensembles shown in blue. The coarse-grained dissipation rate increases from light blue to dark blue.

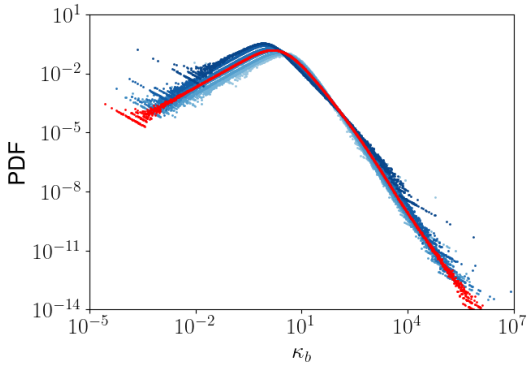

Figure 6.14: PDFs of the curvature of magnetic field lines for the full ensemble shown in red and for the sub-ensembles shown in blue where the coarse-grained dissipation rate increases from light blue to dark blue.

Chapter 7

Conclusions

This thesis covered the geometric description of turbulent flows through statistics of the curvature and torsion of Lagrangian tracer particle trajectories in von Kármán flow, Rayleigh-Bénard convection and a turbulent zero-pressure-gradient boundary layer as well as the curvature of magnetic field lines and stream lines in magnetohydrodynamic turbulence. As a measure of the effect of anisotropy, the curvature vector was introduced and we connected its statistics with large-scale motion. Additionally, we derived a model for the curvature probability density function (PDF) in von Kármán flow and Rayleigh-Bénard convection.

The first project focused on the comparison of statistics of four experimental datasets and the effects of anisotropy on the geometry of tracer particle trajectories. These datasets were von Kármán flow, Rayleigh-Bénard convection (RBC) at two different Rayleigh numbers, and a turbulent zero-pressure-gradient boundary layer in the logarithmic region with Taylor Reynolds numbers $Re_\lambda = 270$, 147, 186, and 108, respectively.

As a first step, we calculated the PDFs of instantaneous velocity, acceleration, curvature, and torsion of Lagrangian trajectories in these datasets. For all datasets, we found near Gaussian PDFs for the velocity components with zero mean, except the streamwise direction for the boundary layer. For the acceleration, isotropy is restored for the streamwise direction in the boundary layer and the PDFs of the acceleration components have wide tails. For the von Kármán flow and Rayleigh-Bénard convection, we found similar results for the curvature PDFs that compare well with previous works on numerical simulations of homogeneous and isotropic turbulence (Braun et al., 2006), experiments of von Kármán flow (Xu et al., 2007) and numerical simulations of Rayleigh-Bénard convection (Alards et al., 2017). That is, the

PDF is linear for small curvature values and has a -2.5 power law for high values. For small values of the curvature, the PDF for the boundary layer has the same linear PDF but for high curvature values the PDF does not follow the -2.5 power law, and high curvature events are suppressed. We expect this to be caused by the strong unidirectional flow in streamwise direction. Based on numerical simulations of homogeneous isotropic turbulence (Scagliarini, 2011) and RBC (Alards et al., 2017), for the torsion PDF a constant PDF for small values and a power law of -3 for high torsion values was expected which agrees with the results found here for all four experimental datasets.

To quantify effects of anisotropy, we introduced the curvature vector and calculated PDFs of its components. One of the main observations made are that the power law for small values changes to a constant PDF while the power law for high curvature values is preserved. Secondly, we were able to detect the direction of anisotropy in the statistics of the different components, caused by the geometry of the flow and experimental setup. Specifically, for von Kármán flow, this anisotropy aligned with the propeller axis, for RBC, the differences occurred between the direction parallel to the temperature gradient and the other two directions, and in the boundary layer, the component with mean flow behaved differently to the two remaining components.

To understand the origin of these differences, we connected the statistics of the curvature vector with velocity fluctuations. This showed that low-curvature events are more likely to occur where velocity fluctuations are stronger. In the case of the boundary layer, this results in meandering trajectories rather than trajectories that curve against the flow.

As von Kármán flow and RBC have the same power laws for curvature and torsion statistics, we used Heisenberg-Yaglom rescaling, which includes the Taylor Reynolds number, to show that the PDFs of the different datasets collapse onto master curves.

In the second project, we used data of direct numerical simulations of magnetohydrodynamic (MHD) turbulence. In total, we analysed five different datasets, of which four had no magnetic background field and one with a magnetic background field. We calculated statistics of the velocity, magnetic field fluctuations, inertial term components and magnetic tension components, where we found that the velocity fluctuations are near Gaussian across all datasets, while the probability density functions of the magnetic field fluctuations are super-Gaussian as found by Seta et al. (2020). For the dataset with a magnetic background

field, the magnetic field fluctuations are closer to a Gaussian. In the direction parallel to the magnetic background field, less extreme magnetic field fluctuations are present. For the inertial term components and magnetic tension components, we found PDFs with a similar shape of the acceleration component PDFs of Lagrangian trajectories, where the effect of intermittency is stronger for the magnetic tension components (Carbone et al., 2004). The component parallel to the magnetic background field has less extreme events in both, inertial term and magnetic tension which can be connected to the partial two-dimensionalisation of the flow (Alexakis, 2011; Gallet and Doering, 2015).

We calculated the curvature PDFs of the magnetic field lines and streamlines and compared our results with previous results of curvature PDFs in different settings of MHD turbulence (Schekochihin et al., 2001, 2002, 2004; Yang et al., 2019; Bandyopadhyay et al., 2020; Huang et al., 2020; Ji et al., 2022; Yuen and Lazarian, 2020; Adrian et al., 2000). We found that the PDF is linear for small values of the curvature and for high curvature values, the exponent of the power to fluctuate between -2.86 and -2.5, which agrees with the previously mentioned works.

We also calculated PDFs of the curvature vector components and analysed the effect of a magnetic background field. As a result, we found that the field lines tend to be less curved in the direction of the magnetic background field which can be connected to the suppression of magnetic field fluctuations parallel to the magnetic background field.

In the works by Schekochihin et al. (2001); Xu et al. (2007); Yang et al. (2019) models for the curvature PDF based on Gaussian statistics are presented. In the third project, we derived a closed-form model for the PDF of the curvature, taking spatio-temporal intermittency into account. The model by Xu et al. (2007) is based on the assumption of Gaussian random variables for the velocity and acceleration components, which we have seen is not correct for the acceleration components. Bentkamp et al. (2019) presented a decomposition of the whole ensemble into smaller sub-ensembles based on the coarse-grained acceleration, taking intermittency into account. These sub-ensemble have near Gaussian acceleration PDFs and this was the first time that this decomposition is applied to experimental data, namely von Kármán flow and Rayleigh-Bénard convection. This allowed us to write down the analytic expression for the curvature PDF in the sub-ensembles. Using the law of total probability, we derived a closed-form expression of the curvature of the full ensemble, which includes

a correction factor that takes spatio-temporal intermittency into account. Comparing this expression with numerical results of the PDF of the full ensemble, we found that the PDFs agree qualitatively and quantitatively.

We anticipate that this model is applicable to different complex systems with small levels of anisotropy, for example to the curvature of magnetic field lines in plasma turbulence. In a first attempt, we used the magnetic coarse-grained dissipation rate to decompose the full ensemble into sub-ensemble. However, this does not seem to work and further work needs to be done to find a suitable decomposition method.

7.1 Future Work

I will give a short overview of potential extensions of the discussed results.

An analysis of the effect of small-scale fluctuations, namely the acceleration, on the curvature vector statistics would help with the further understanding of the curvature vector. This could also lead to an exploration to quantify the strength of anisotropies, where boundary layer data with different free stream velocities or MHD data with different magnetic background field strengths could be analysed. A third possible direction would be to spatially decompose the flow by conditioning on turbulent superstructures, for example raising plumes in Rayleigh-Bénard convection.

An additional project based on the presented work could be the derivation of a model PDF for the curvature in MHD turbulence. As a initial step, we would suggest to use the coarse-grained magnetic tension or inertial term as an observable to condition on, in analogy to the method presented by Bentkamp et al. (2019) for Lagrangian trajectories.

References

Adrian, R. J., Meinhart, C. D. and Tomkins, C. D. (2000), 'Vortex organization in the outer region of the turbulent boundary layer', *J. Fluid Mech.* **422**, 1–54.

Alards, K. M. J., Rajaei, H., Del Castello, L., Kunnen, R. P. J., Toschi, F. and Clercx, H. J. H. (2017), 'Geometry of tracer trajectories in rotating turbulent flows', *Phys. Rev. Fluids* **2**, 044601.

Alexakis, A. (2011), 'Two-dimensional behavior of three-dimensional magnetohydrodynamic flow with a strong guiding field', *Phys. Rev. E* **84**, 056330.

Aluie, H. (2017), 'Coarse-grained incompressible magnetohydrodynamics: analyzing the turbulent cascades', *New J. Phys.* **19**(2), 025008.

Bandyopadhyay, R., Yang, Y., Matthaeus, W. H., Chasapis, A., Parashar, T. N., Russell, C. T., Strangeway, R. J., Torbert, R. B., Giles, B. L., Gershman, D. J., Pollock, C. J., Moore, T. E. and Burch, J. L. (2020), 'In situ measurement of curvature of magnetic field in turbulent space plasmas: A statistical study', *Astrophys. J. Lett.* **893**(1), L25.

Batchelor, G. K. (1953), *The Theory of Homogeneous Turbulence*, Cambridge University Press.

Bentkamp, L., Drivas, T., Lalescu, C. and Wilczek, M. (2022), 'The statistical geometry of material loops in turbulence', *Nat. Commun.* **13**, 2088.

Bentkamp, L., Lalescu, C. C. and Wilczek, M. (2019), 'Persistent accelerations disentangle Lagrangian turbulence', *Nat. Commun.* **10**, 3550.

Biferale, L., Boffetta, G., Celani, A., Devenish, B., Lanotte, A. and Toschi, F. (2004),

'Multifractal Statistics of Lagrangian Velocity and Acceleration in Turbulence', *Phys. Rev. Lett.* **93**, 064502.

Biferale, L., Boffetta, G., Celani, A., Lanotte, A. and Toschi, F. (2004), 'Particle trapping in three-dimensional fully developed turbulence', *Phys. Fluids* **17**(2), 021701.

Biferale, L. and Toschi, F. (2005), 'Joint statistics of acceleration and vorticity in fully developed turbulence', *J. Turbul.* **6**, N40.

Biskamp, D. (2003), *Magnetohydrodynamic Turbulence*, Cambridge University Press.

Borue, V. and Orszag, S. A. (1995), 'Forced three-dimensional homogeneous turbulence with hyperviscosity', *Europhys. Lett.* **29**(9), 687.

Bosbach, J., Schanz, D., Godbersen, P. and Schröder, A. (2021), 'Spatially and temporally resolved measurements of turbulent Rayleigh-Bénard convection by Lagrangian particle tracking of long-lived helium-filled soap bubbles', *Proceedings of 14th International Symposium on Particle Image Velocimetry - ISPIV 2021* . Munich, Germany.

Braun, W., Lillo, F. D. and Eckhardt, B. (2006), 'Geometry of particle paths in turbulent flows', *J. Turbul.* **7**, N62.

Bross, M., Schanz, D., Novara, M., Eich, F., Schröder, A. and Kähler, C. (2023), 'Turbulent superstructure statistics in a turbulent boundary layer with pressure gradients', *Eur. J. Mech. B Fluids* **101**, 209–218.

Buaria, D. and Sreenivasan, K. R. (2022), 'Scaling of acceleration statistics in high reynolds number turbulence', *Phys. Rev. Lett.* **128**, 234502.

Buchwald, T., Schanz, D., Gesemann, S. and Schröder, A. (2022), 'Investigation of universal small-scale structures in turbulence using Shake-The-Box Lagrangian Particle Tracking and FlowFit', *Proceedings of 20th International Symposium on Applications of Laser and Imaging Techniques to Fluid Mechanics* . Lisbon, Portugal.

Busse, A. (2009), 'Lagrangesche statistische Eigenschaften hydrodynamischer und magnetohydrodynamischer Turbulenz', PhD thesis, University of Bayreuth, Faculty of Mathematics, Physics and Computer Sciences, Bayreuth.

Buzzicotti, M., Linkmann, M., Aluie, H., Biferale, L., Brasseur, J. and Meneveau, C. (2018), 'Effect of filter type on the statistics of energy transfer between resolved and subfilter scales from a-priori analysis of direct numerical simulations of isotropic turbulence', *J. Turbul.* **19**(2), 167–197.

Bär, C. (2010), *Elementary Differential Geometry*, Cambridge University Press.

Canuto, C., Hussaini, M. Y., Quarteroni, A. and Zang, T. A. (1988), *Spectral Methods in Fluid Mechanics*, Springer–Verlag, New York.

Capocci, D. (2024), 'Governing physical mechanisms in (magneto)hydrodynamic turbulence', PhD thesis, Dept. Physics, University of Rome Tor Vergata.

Capocci, D., Johnson, P., Oughton, S., Biferale, L. and Linkmann, M. (2024), 'Energy flux decomposition in magnetohydrodynamic turbulence', *arXiv preprint arXiv:2402.10125* . in press.

Carbone, V., Bruno, R., Sorriso-Valvo, L. and Lepreti, F. (2004), 'Intermittency of magnetic turbulence in slow solar wind', *Planet. Space Sci.* **52**(10), 953–956. Nonlinear Processes in Solar System Plasmas.

de Boor, C. (1978), *A Practical Guide to Spline*, Vol. Volume 27, Springer New York, NY.

Dierckx, P. (1982), 'Algorithms for smoothing data with periodic and parametric splines', *Computer Graphics and Image Processing* **20**(2), 171–184.

Dombre, T., Frisch, U., Greene, J. M., Hénon, M., Mehr, A. and Soward, A. M. (1986), 'Chaotic streamlines in the abc flows', *J. Fluid Mech.* **167**, 353–391.

Donzis, D., Yeung, P. and Sreenivasan, K. (2008), 'Dissipation and enstrophy in isotropic turbulence: resolution effects and scaling in direct numerical simulations', *Phys. Fluids* **20**(4).

Falkovich, G., Xu, H., Pumir, A., Bodenschatz, E., Biferale, L., Boffetta, G., Lanotte, A. S. and Toschi, F. (2012), 'On Lagrangian single-particle statistics', *Phys. Fluids* **24**(5). 055102.

Fisher, R. A. (1930), 'The moments of the distribution for normal samples of measures of departure from normality', *Proc. R. soc. Lond. Ser. A-Contain. Pap. Math. Phys. Character* **130**(812).

Frisch, U. (1995), *Turbulence: The Legacy of A. N. Kolmogorov*, Cambridge University Press.

Frisch, U., Kurien, S., Pandit, R., Pauls, W., Ray, S. S., Wirth, A. and Zhu, J.-Z. (2008), 'Hyperviscosity, galerkin truncation, and bottlenecks in turbulence', *Phys. Rev. Lett.* **101**, 144501.

Gallet, B. and Doering, C. R. (2015), 'Exact two-dimensionalization of low-magnetic-reynolds-number flows subject to a strong magnetic field', *J. Fluid Mech.* **773**, 154–177.

Gesemann, S., Huhn, F., Schanz, D. and Schröder, A. (2016), 'From Particle Tracks to Velocity and Acceleration Fields Using B-Splines and Penalties', *Proceedings of 18th International Symposium on Applications of Laser Techniques to Fluid Mechanics* . Lisbon, Portugal.

Godbersen, P., Bosbach, J., Schanz, D. and Schröder, A. (2021), 'Beauty of turbulent convection: A particle tracking endeavor', *Phys. Rev. Fluids* **6**, 110509.

Grossmann, S. and Lohse, D. (2000), 'Scaling in thermal convection: a unifying theory', *J. Fluid Mech.* **407**, 27–56.

Gubner, J. A. (2006), *Probability and Random Processes for Electrical and Computer Engineers*, Cambridge University Press.

Haugen, N. E. L. and Brandenburg, A. (2004), 'Inertial range scaling in numerical turbulence with hyperviscosity', *Phys. Rev. E* **70**, 026405.

Heisenberg, W. (1948), 'Zur statistischen Theorie der Turbulenz', *Zeitschrift für Physik* **124**, 628–657.

Hengster, Y., Lellep, M., Weigel, J., Bross, M., Bosbach, J., Schanz, D., Schröder, A., Huhn, F., Novara, M., Garaboa Paz, D., Kähler, C. J. and Linkmann, M. (2024), 'Effects of anisotropy on the geometry of tracer particle trajectories in turbulent flows', *Eur. J. Mech. B Fluids* **103**, 284–298.

Hengster, Y. and Linkmann, M. (2024), 'Lagrangian curvature statistics from Gaussian subensembles in turbulence', *in preparation* .

Homann, H., Schulz, D. and Grauer, R. (2011), 'Conditional Eulerian and Lagrangian velocity increment statistics of fully developed turbulent flow', *Phys. Fluids* **23**(5), 055102.

Huang, S. Y., Zhang, J., Sahraoui, F., Yuan, Z. G., Deng, X. H., Jiang, K., Xu, S. B., Wei, Y. Y., He, L. H. and Zhang, Z. H. (2020), 'Observations of magnetic field line curvature and its role in the space plasma turbulence', *Astrophys. J. Lett.* **898**(1), L18.

Huhn, F., Schanz, D., Gesemann, S., Dierksheide, U., Meerendonk, R. and Schröder, A. (2017), 'Large-scale volumetric flow measurement in a pure thermal plume by dense tracking of helium-filled soap bubbles', *Exp. Fluids* **58**(116).

Ishihara, T., Kaneda, Y., Yokokawa, M., Itakura, K. and Uno, A. (2007), 'Small-scale statistics in high-resolution direct numerical simulation of turbulence: Reynolds number dependence of one-point velocity gradient statistics', *J. Fluid Mech.* **592**, 335–366.

Jahn, T., Schanz, D. and Schröder, A. (2021), 'Advanced iterative particle reconstruction for Lagrangian particle tracking', *Exp. Fluids* **62**(8), 179.

Ji, Y., Shen, C., Ren, N., Ma, L., Ma, Y. H. and Chen, X. (2022), 'Curvature of magnetic field and its role on plasma in turbulent magnetosheath', *Astrophys. J.* **941**(1), 67.

Jucha, J. (2014), 'Time-Symmetry Breaking in Turbulent Multi-Particle Dispersion', PhD thesis, Georg-August University School of Science.

Kalman, R. E. (1960), 'A New Approach to Linear Filtering and Prediction Problems', *J. Basic Eng.* **82**(1), 35–45.

Kolmogorov, A. N. (1941), 'The Local Structure of Turbulence in Incompressible Viscous Fluid for Very Large Reynolds' Numbers', *Akademiia Nauk SSSR Doklady* **30**, 301–305.

Kolmogorov, A. N. (1962), 'A refinement of previous hypotheses concerning the local structure of turbulence in a viscous incompressible fluid at high reynolds number', *J. Fluid Mech.* **13**(1), 82–85.

Lalescu, C. C. and Wilczek, M. (2018), 'Acceleration statistics of tracer particles in filtered turbulent fields', *J. Fluid Mech.* **847**, R2.

Lawson, J. M., Bodenschatz, E., Lalescu, C. C. and Wilczek, M. (2018), 'Bias in particle tracking acceleration measurement', *Exp. Fluids* **59**(11), 172.

Lemoine, M. (2023), 'Particle transport through localized interactions with sharp magnetic field bends in mhd turbulence', *J. Plasma Phys.* **89**(5), 175890501.

Maxey, M. R. and Riley, J. J. (1983), 'Equation of motion for a small rigid sphere in a nonuniform flow', *Phys. Fluids* **26**(4), 883–889.

Mordant, N., Crawford, A. and Bodenschatz, E. (2004), 'Three-Dimensional Structure of the Lagrangian Acceleration in Turbulent Flows', *Phys. Rev. Lett.* **93**, 214501.

Mordant, N., Lévêque, E. and Pinton, J. (2004), 'Experimental and numerical study of the Lagrangian dynamics of high Reynolds turbulence', *New J. Phys.* **6**(1), 116.

Mordant, N., Metz, P., Pinton, J. and Michel, O. (2002), 'Lagrangian measurement in fully developed turbulence', *AIP Conference Proceedings* **622**(1), 343–352.

Ni, R., Huang, S. and Xia, K. (2012), 'Lagrangian acceleration measurements in convective thermal turbulence', *J. Fluid Mech.* **692**, 395–419.

Oberbeck, A. (1879), 'Ueber die Wärmeleitung der Flüssigkeiten bei Berücksichtigung der Strömungen infolge von Temperaturdifferenzen', *Annalen der Physik* **243**(6), 271–292.

Oboukhov, A. M. (1962), 'Some specific features of atmospheric tubulence', *J. Fluid Mech.* **13**(1), 77–81.

Offermans, G. P., Biferale, L., Buzzicotti, M. and Linkmann, M. (2018), 'A priori study of the subgrid energy transfers for small-scale dynamo in kinematic and saturation regimes', *Phys. Plasmas* **25**(12), 122307.

Orszag, S. A. (1971), 'On the elimination of aliasing in finite-difference schemes by filtering high-wavenumber components', *J. Atmos. Sci.* **28**(6), 1074 – 1074.

Ouellette, N. T., Xu, H., Bourgoin, M. and Bodenschatz, E. (2006), 'Small-scale anisotropy in Lagrangian turbulence', *New J. Phys.* **8**(6), 102.

Patterson Jr, G. S. and Orszag, S. A. (1971), 'Spectral calculations of isotropic turbulence: Efficient removal of aliasing interactions', *Phys. Fluids* **14**(11), 2538–2541.

Pope, S. B. (2000), *Turbulent Flows*, Cambridge University Press.

Porta, A. L., Voth, G. A., Crawford, A., Alexander, J. and Bodenschatz, E. (2001), 'Fluid particle accelerations in fully developed turbulence', *Nature* **409**, 1017–1019.

Pressley, A. (2001), *Elementary Differential Geometry*, Springer.

Richardson, L. F. (2007), *Weather Prediction by Numerical Process*, Cambridge Mathematical Library, 2 edn, Cambridge University Press.

Scagliarini, A. (2011), 'Geometric properties of particle trajectories in turbulent flows', *J. Turbul.* **12**, N25.

Scarano, F., Ghaemi, S., Caridi, G. C. A., Bosbach, J., Dierksheide, U. and Sciacchitano, A. (2015), 'On the use of helium-filled soap bubbles for large-scale tomographic PIV in wind tunnel experiments', *Exp. Fluids* **56**, 42.

Schanz, D., Gesemann, S. and Schröder, A. (2016), 'Shake-The-Box: Lagrangian particle tracking at high particle image densities', *Exp. Fluids* **57**(5), 70.

Schanz, D., Schröder, A., Novara, M., Geisler, R., Agocs, J., Eich, F., Bross, M. and Kähler, C. J. (2019), 'Large-scale volumetric characterization of a turbulent boundary layer flow', *Proceedings of the 13th International Symposium on Particle Image Velocimetry – ISPIV 2019* . Munich, Germany.

Schekochihin, A. A., Cowley, S. C., Taylor, S. F., Maron, J. L. and McWilliams, J. C. (2004), 'Simulations of the small-scale turbulent dynamo', *Astrophys. J.* **612**(1), 276.

Schekochihin, A. A., Maron, J. L., Cowley, S. C. and McWilliams, J. C. (2002), 'The small-scale structure of magnetohydrodynamic turbulence with large magnetic prandtl numbers', *Astrophys. J.* **576**(2), 806.

Schekochihin, A., Cowley, S., Maron, J. and Malyshkin, L. (2001), 'Structure of small-scale magnetic fields in the kinematic dynamo theory', *Phys. Rev. E* **65**, 016305.

Schlichting, H. and Gersten, K. (2017), *Boundary-Layer Theory*, 9th edn, Springer.

Schröder, A., Schanz, D., Gesemann, S., Huhn, F., Buchwald, T., Paz, D. G. and Bodenschatz, E. (2022), 'Measurements of the energy dissipation rate in homogeneous turbulence using dense 3D Lagrangian Particle Tracking and FlowFit', *Proceedings of 20th International Symposium on Application of Laser and Imaging Techniques to Fluid Mechanics* . Lisbon, Portugal.

Schröder, A. and Schanz, D. (2023), '3D Lagrangian Particle Tracking in Fluid Mechanics', *Annu. Rev. Fluid Mech.* **55**(1), 511–540.

Schumacher, J. (2009), 'Lagrangian studies in convective turbulence', *Phys. Rev. E* **79**, 056301.

SciPy Community (2023), *SciPy: scipy.integrate.odeint function*. Accessed: 2024-09-09.
URL: *https://docs.scipy.org/doc/scipy/reference/generated/scipy.integrate.odeint.html*

SciPy Developers (2024), *scipy.interpolate.splrep*. Accessed: 2024-09-08.
URL: *https://docs.scipy.org/doc/scipy/reference/generated/scipy.interpolate.splrep.html*

Seta, A., Bushby, P. J., Shukurov, A. and Wood, T. S. (2020), 'Saturation mechanism of the fluctuation dynamo at $\mathrm{pr}_M \geq 1$', *Phys. Rev. Fluids* **5**, 043702.

Shahmohamadi, H. and Rashidi, M. M. (2017), 'Experimental investigation and a novel analytical solution of turbulent boundary layer flow over a flat plate in a wind tunnel', *International Journal of Mechanical Sciences* **133**, 121–128.

Siegrist, K. (2022), 'Transformations of Random Variables'. [Online; accessed 2024-07-16].

Spyksma, K., Magcalas, M. and Campbell, N. (2012), 'Quantifying effects of hyperviscosity on isotropic turbulence', *Phys. Fluids* **24**(12), 125102.

Stelzenmuller, N., Polanco, J. I., Vignal, L., Vinkovic, I. and Mordant, N. (2017), 'Lagrangian acceleration statistics in a turbulent channel flow', *Phys. Rev. Fluids* **2**, 054602.

Taylor, G. I. (1935), 'Statistical theory of turbulence', *Proceedings of the Royal Society of London. Series A - Mathematical and Physical Sciences* **151**(873), 421–444.

Toschi, F. and Bodenschatz, E. (2009), 'Lagrangian properties of particles in turbulence', *Annu. Rev. Fluid Mech.* **41**(1), 375–404.

Townsend, A. A. (1947), 'The measurement of double and triple correlation derivatives in isotropic turbulence', *Math. Proc. Camb. Philos. Soc.* **43**(4), 560–570.

Voth, G. A., La Porta, A., Crawford, A., Bodenschatz, E. and Alexander, J. (2002), 'Measurement of particle accelerations in fully developed turbulence', *J. Fluid Mech.* **469**, 121–160.

Wan, M., Oughton, S., Servidio, S. and Matthaeus, W. (2010), 'On the accuracy of simulations of turbulence', *Phys. Plasmas* **17**(8).

Weigel, J., Linkmann, M. and Lellep, M. (2020), 'Trajectory Analyzer (TARA)'.
URL: *https://bitbucket.org/WeigelJu/trajectory-analyzer-tara/src/master/*

Wieneke, B. (2012), 'Iterative reconstruction of volumetric particle distribution', *Meas. Sci. Technol* **24**(2), 024008.

Xu, H., Ouellette, N. and Bodenschatz, E. (2007), 'Curvature of Lagrangian Trajectories in Turbulence', *Phys. Rev. Lett.* **98**, 050201.

Yaglom, A. M. (1949), 'On the acceleration field in a turbulent flow', *C. R. Akad. URSS* **67**(5), 795–798.

Yang, Y., Wan, M., Matthaeus, W. H., Shi, Y., Parashar, T. N., Lu, Q. and Chen, S. (2019), 'Role of magnetic field curvature in magnetohydrodynamic turbulence', *Phys. Plasmas* **26**(7), 072306.

Yeung, P. K. and Pope, S. B. (1989), 'Lagrangian statistics from direct numerical simulations of isotropic turbulence', *J. Fluid Mech.* **207**, 531–586.

Yeung, P. K., Pope, S. B., Lamorgese, A. G. and Donzis, D. A. (2006), 'Acceleration and dissipation statistics of numerically simulated isotropic turbulence', *Phys. Fluids* **18**(6), 065103.

Yuen, K. H. and Lazarian, A. (2020), 'Curvature of magnetic field lines in compressible magnetized turbulence: Statistics, magnetization predictions, gradient curvature, modes, and self-gravitating media', *Astrophys. J.* **898**(1), 66.